Natália Maleski de Sá

Thermodynamic comparison of a wine cooler operating with a magnetic prototype and a vapor compression refrigeration system

Florianópolis
December, 2020

Natália Maleski de Sá

Thermodynamic comparison of a wine cooler operating with a magnetic prototype and a vapor compression refrigeration system

Trabalho de Conclusão de Curso apresentado ao Curso de Graduação em Engenharia Mecânica da Universidade Federal de Santa Catarina como parte dos requisitos para obtenção do título de Bacharel em Engenharia Mecânica.

Universidade Federal de Santa Catarina
Departamento de Engenharia Mecânica

Supervisor: Jader Riso Barbosa Jr.
Co-supervisor: Alan Tihiro Nakashima e Jaime Andrés Lozano Cadena

Florianópolis
December, 2020

Ficha de identificação da obra elaborada pelo autor,
através do Programa de Geração Automática da Biblioteca Universitária da UFSC.

de Sá, Natália Maleski
Thermodynamic comparison of a wine cooler operating with a magnetic prototype and a vapor compression refrigeration system / Natália Maleski de Sá ; orientador, Jader Riso Barbosa Jr., coorientador, Alan Tihiro Dias Nakashima, coorientador, Jaime Andrés Lozano Cadena, 2020.
126 p.

Trabalho de Conclusão de Curso (graduação) - Universidade Federal de Santa Catarina, Centro Tecnológico, Graduação em Engenharia Mecânica, Florianópolis, 2020.

Inclui referências.

1. Engenharia Mecânica. 2. Refrigeração magnética. 3. Compressão mecânica de vapores. 4. Caracterização termodinâmica. 5. Comparação de performance. I. Riso Barbosa Jr., Jader. II. Tihiro Dias Nakashima, Alan. III. Lozano Cadena, Jaime Andrés IV. Universidade Federal de Santa Catarina. Graduação em Engenharia Mecânica. V. Título.

Natália Maleski de Sá

Thermodynamic comparison of a wine cooler operating with a magnetic prototype and a vapor compression refrigeration system

Este Trabalho de Conclusão de Curso foi julgado adequado para obtenção do Título de Engenheira Mecânica e aprovado em sua forma final pela Comissão Examinadora e pelo Curso de Graduação em Engenharia Mecânica da Universidade Federal de Santa Catarina.

Florianópolis, 18 de dezembro de 2020.

Documento assinado digitalmente
Carlos Enrique Nino Bohorquez
Data: 19/11/2021 21:05:24-0300
CPF: 564.878.519-49
Verifique as assinaturas em https://v.ufsc.br

Prof. Carlos Enrique Niño Bohórquez, Dr. Eng.
Coordenador do Curso de Graduação em Engenharia Mecânica

Comissão Examinadora:

Documento assinado digitalmente
Jader Riso Barbosa Junior
Data: 17/11/2021 13:38:19-0300
CPF: 010.026.207-40
Verifique as assinaturas em https://v.ufsc.br

Prof. Jader Riso Barbosa Jr., Ph.D - Orientador
Universidade Federal de Santa Catarina

Documento assinado digitalmente
Alan Tihiro Dias Nakashima
Data: 17/11/2021 14:45:13-0300
CPF: 772.834.572-91
Verifique as assinaturas em https://v.ufsc.br

Alan Tihiro Dias Nakashima, M.Sc. - Coorientador
Universidade Federal de Santa Catarina

Documento assinado digitalmente
Jaime Andres Lozano Cadena
Data: 17/11/2021 16:27:10-0300
CPF: 011.171.599-73
Verifique as assinaturas em https://v.ufsc.br

Jaime Andrés Lozano Cadena, Ph.D - Coorientador
Universidade Federal de Santa Catarina

Documento assinado digitalmente
Joel Boeng
Data: 17/11/2021 13:55:44-0300
CPF: 042.587.559-82
Verifique as assinaturas em https://v.ufsc.br

Joel Boeng, M.Sc. - Avaliador
Universidade Federal de Santa Catarina

Documento assinado digitalmente
Saulo Guths
Data: 17/11/2021 13:47:27-0300
CPF: 538.889.529-72
Verifique as assinaturas em https://v.ufsc.br

Prof. Saulo Güths, Dr. Eng. - Avaliador
Universidade Federal de Santa Catarina

Acknowledgements

Agradeço primeiramente ao Prof. Jader Riso Barbosa Jr., por ter me proporcionado a incrível oportunidade de trabalhar no Polo e no Polomag. O seu "sim" foi crucial em meu desenvolvimento como engenheira e pesquisadora. Agradeço também pela orientação nestes quase 4 anos e pelas contribuições feitas para este trabalho.

Ao meus Coorientadores, Ms. Eng. Alan Tihiro Nakashima e Dr. Jaime Andrés Lozano, pela mentoria e por todos os conhecimentos compartilhados, não só durante este trabalho, mas em toda a jornada dentro do Polo. Agradeço também pela decisão acertada na sugestão deste tema, que foi cativante e desafiador do início ao fim. Alan, um agradecimento especial pela inesgotável fonte de paciência com as minhas perguntas, das simples às complexas, e por todos os momentos de companheirismo compartilhados nestes anos.

Agradeço também a todo o time Polomag. A contribuição de cada um de vocês foi o que tornou possível a realização deste trabalho. Ao Sergio, pelo grande companheirismo e pelos ensinamentos desde o meu primeiro dia no Polo. Ao Bernardo, por embarcar comigo nas mais aleatórias aventuras fora do contexto do laboratório. À Gislaine, pela incansável vontade de ajudar a todos em suas respectivas atividades e pela grande contribuição na montagem do protótipo. Ao Victor, pelo companheirismo nos altos e baixos de um trabalho experimental e pela parceria na montagem do protótipo. Agradeço a todos os membros, atuais e antigos, pelas contribuições neste projeto inovador, e pelos momentos de descontração e de *insights* disfarçados de procrastinação. Obrigada, Guilherme, Henrique, Fábio, Gusttav, Joana, Diego, Higor, Maria, Luís, Luiza, Mayara, Laryssa, Ricardo, Matheus, Gabriel M., Gabriel G., Paulo, Elias e demais membros. Um agradecimento especial ao Marcelo e ao Anderson, pela competência e pela ajuda fundamental prestada durante toda a etapa de montagem do protótipo.

Um reconhecimento especial à banca examinadora, Ms. Eng. Joel Boeng e Prof. Saulo Guths. Obrigada pelo tempo e experiência doados na avaliação deste trabalho e por todas as contribuições.

Ao meu amor, João Fábio, pelo apoio incondicional durante todas as fases da minha graduação e pela paciência nos (muitos) fins de semana do ano letivo em que estive na universidade ou no laboratório, e não em casa. Obrigada por ser a base estável durante todas as instabilidades da vida. Obrigada por caminhar ao meu lado.

Aos meus pais, Heitor e Aline, por todo o amor e apoio durante toda a vida. Cheguei até aqui graças a vocês. Às minhas primas, Brenda e Gabriela, por estarem comigo em todos os momentos da vida, seja na alegria ou na tristeza. À toda a minha família, pela resiliência diante dos momentos tristes. Um agradecimento especial à minha tia Simone, meu avô Rogério e minha avó Varilda, em memória, cujo amor e carinho serão sempre o meu combustível nos momentos de dificuldade.

Por fim, quero agradecer a todos que de alguma forma contribuiram para este trabalho.

"Only entropy comes easy." (Anton Chekhov)

Abstract

In the past decades, research on alternative cooling technologies have heavily emerged due to ongoing environmental regulations. In this framework, magnetic refrigeration is one of the most promising for applications near room temperature. Several magnetic refrigerator prototypes have been developed throughout the years, but most of them are focused on the development and optimization of single components, not the system as a whole. Up to now, none of the literature in magnetic refrigeration field reported the level of maturity of the prototypes towards the well established vapor compression technology, nor the stage of competitiveness in terms of performance. Hence, in this thesis, a performance comparison between magnetic and vapor compression technologies was carried out, when operating the same wine cooler cabinet. To that end, both cooling technologies were firstly thermodynamically characterized. A commercial wine cooler based on vapor compression was characterized in terms of temperature pull down time, energy consumption and reverse heat leakage tests, for two levels of internal temperature (8 and 12ºC) and for an ambient temperature of 25ºC. A magnetic wine cooler prototype, previously designed by the research group PoloMag at the Federal University of Santa Catarina (UFSC), was built and coupled with the same cabinet of the vapor compression wine cooler, through a set of a heat exchanger and a fan. The prototype was characterized through performance maps, developed by a combination of different operating frequencies (from 0.5 to 1.0 Hz) and flow rates (from 125 to 225 L/h) as input variables, and an ambient temperature of 25ºC. In an overall comparison of both cooling technologies, the magnetic wine cooler demanded higher energy consumptions, higher temperature pull down time and higher cooling capacities to reach around the same cabinet temperature. Also, the magnetic wine cooler provided inferior COP and overall second-law efficiency than the vapor compression wine cooler. To maintain a temperature of 12.5ºC inside the cabinet, the magnetic wine cooler presented an energy consumption of 505 kWh/year and a cooling capacity of 24.3 W. For this point, the COP was 0.41, the overall second-law efficiency was 1.7% and the temperature pull down time was 5.0 h. To maintain a temperature of 12.0ºC inside the cabinet, the vapor compression wine cooler presented an energy consumption of 272 kWh/year and a cooling capacity of 22.2 W. For this point, the COP was 0.70, the overall second-law efficiency was 3.1% and the temperature pull down time was 1.1 h. In a further analysis of the second-law efficiency and COP, it was demonstrated that the low performance results of the magnetic wine cooler were mainly due to internal irreversibilities. However, high result of internally ideal COP indicated a wide potential of improvement in this regard. In this terms, the magnetic technology is still behind from the vapor compressor regarding overall performance, and there is still a long way to become a competitive technology, but there is also a great potential to do so.

Keywords: Magnetic refrigeration, vapor compression refrigeration, thermodynamic characterization, performance comparison, COP, second-law efficiency.

Resumo

Nas últimas décadas, um grande número de pesquisas em tecnologias alternativas de refrigeração emergiram devido à regulamentações ambientais em andamento no mundo. Neste contexto, a refrigeração magnética tem se mostrado como uma das tecnologias mais promissoras em aplicações próximas à temperatura ambiente. Diversos protótipos de refrigeradores magnéticos foram desenvolvidos nos últimos anos, mas a maioria está focada no desenvolvimento e otimização de componentes, e não do sistema como um todo. Até o momento, nenhum dos trabalhos publicados na área de refrigeração magnética avaliaram o grau de maturidade e de competitividade da tecnologia relativamente à tecnologia vigente de compressão mecânica de vapores. Portanto, neste trabalho, uma comparação das performances das tecnologias magnética e de compressão mecânica de vapores ao operar um mesmo gabinete de adega de vinhos foi realizada. Para isso, as duas tecnologias foram primeiramente caracterizadas termodinamicamente. Uma adega de vinhos comercial que opera com compressão mecânica de vapores foi caracterizada em termos de testes de *pull down* de temperatura, consumo de energia e fluxo de calor reverso. A caracterização foi realizada para duas temperaturas de gabinete (8 e 12ºC) e para uma temperatura ambiente de 25ºC. Um protótipo de adega de vinhos magnética, previamente projetado pelo grupo de pesquisa PoloMag da Universidade Federal de Santa Catarina (UFSC), foi montado e acoplado ao mesmo gabinete da adega a compressão mecânica através de um conjunto de trocador de calor e ventilador. O protótipo foi caracterizado através de mapas de performance, que foram desenvolvidos com a combinação de diferentes frequências de operação (0.5 a 1.0 Hz) e vazões (125 a 225 L/h) como variáveis de entrada, além de uma temperatura ambiente de 25ºC. Numa comparação geral das duas tecnologias de refrigeração, a adega magnética apresentou maiores consumos de energia, tempo de *pull down* de temperatura e capacidades de refrigeração para atingir em torno da mesma temperatura de gabinete. Além disso, forneceu valores inferiores de COP e eficiência de segunda lei em relação à adega a compressão mecânica. Para manter uma temperatura de gabinete de 12.5ºC, a adega magnética apresentou um consumo de energia de 505 kWh/ano e uma capacidade de refrigeração de 24.3 W. Para o mesmo ponto, o COP foi de 0.41, a eficiência de segunda lei 1.7% e o tempo de *pull down* de temperatura de 5.0 h. Para manter uma temperatura de gabinete de 12.0ºC, a adega a compressão mecânica apresentou um consumo de energia de 272 kWh/ano e uma capacidade de refrigeração de 22.2 W. Para o mesmo ponto, o COP foi de 0.70, a eficiência de segunda lei 3.1% e o tempo de *pull down* de temperatura de 1.1 h. Em uma análise mais detalhada da eficiência de segunda lei e do COP, foi constatado que os baixos resultados em termos de performance da adega magnética foram devidos, em maioria, à irreversibilidades internas. Em contraste, um alto resultado de COP internamente ideal foi obtido — em relação à adega de compressão mecânica, o que mostrou que há um grande potencial de melhoria neste quesito. Nestes termos, a tecnologia de refrigeração magnética se mostrou inferior no que diz respeito à tecnologia de compressão mecânica de vapores em termos de performance, e existe ainda um longo caminho a ser percorrido para que a primeira venha a

se tornar uma tecnologia competitiva. Existe, no entanto, um amplo potencial para que este nível possa ser atingido.

Palavras-chave: Refrigeração magnética, compressão mecânica de vapores, caracterização termodinâmica, comparação de performance, COP, eficiência de segunda lei.

List of Figures

List of Tables

Nomenclature

Roman letters

COP	coefficient of performance [-]
c	specific heat capacity [J kg^{-1}K^{-1}]
f	frequency [Hz]
H	magnetic field [T]
h	heat transfer coefficient [W m^{-2} K^{-1}]
k	thermal conductivity [W m^{-1} K^{-1}]
NTU	number of transfer units [-]
Nu	Nusselt number [-]
p	pressure [bar]
$\dot{Q}$	heat transfer rate [W]
Ra	Rayleigh number [-]
Re	Reynolds number [-]
$\dot{S}$	entropy rate [kW K^{-1}]
S	entropy [kJ K^{-1}]
s	specific entropy [kJ kg^{-1} K^{-1}]
T	temperature [^{o}C]
U	overall heat transfer coefficient [W m^{-2} K^{-1}]
UA	overall thermal conductance [W K^{-1}]
$\dot{V}$	volumetric flow rate [L s^{-1}]
v	specific volume [m^{3} kg^{-1}]
$\dot{W}$	power [W]

Greek letters

β	thermal expansion coefficient [K^{-1}]
Γ	torque [N m]

Δ	variation of a parameter [-]
ϵ	effectiveness [-]
η	efficiency [%]
ω	angular speed [rad s^{-1}]
ϕ	utilization factor [-]
ρ	fluid density [kg m^{-3}]
σ	specific magnetization [A m^2 kg^{-1}]

Subscripts

2nd	second-law
ad	adiabatic
amb	ambient
cab	cabinet
Carnot	Carnot cycle
CB	cold blow
C	cold
CE	cold end
CF	cold fan
H	hot
HE	hot end
CHEx	cold heat exchanger
cond	condenser
cycle	AMR cycle
ele	electric
evap	evaporator
F	fan
HF	hot fan
f	final
f	fluid

Fil	filter
FM	flow meter
gen	generated
HB	hot blow
HEx	heat exchanger
HHEx	hot heat exchanger
i	initial
ii	internally ideal
in	inlet
ins	insulation
int	internal
iso	isothermal
lat	lattice
loss	losses
low	lower compartment
Mag	magnetic interaction
Mo	motor
ext	external
out	outlet
P	pump
reg	regenerator
R	reference
s	solid
up	upper compartment
sur	surroundings
sys	system
Total	total
Tr	transmission

V	valve

Abbreviations

AMR	active magnetic regenerator
CHEx	cold heat exchanger
EC	energy consumption
Gd	gadolinium
Gd-Y	gadolinium alloy
HEx	heat exchanger
HHEx	hot heat exchanger
IHX	internal heat exchanger
La-Fe-Si-H	lanthanum-iron-sylicon alloys
La-Fe-Si	lanthanum-iron-sylicon
MCE	magnetocaloric effect
PID	proportional-integral-derivative controller
PU	polyurethane
RHL	reverse heat leakage

Contents

1 Introduction

Refrigeration systems have been of huge importance in the development of modern society, not only for food preservation, but also for human productivity, health, transportation and, more recently, communications and data processing. By definition, refrigeration is concerned with the cooling of bodies or fluids to temperatures lower than those available in the surroundings, at a particular time and place (GOSNEY, 1982). Fundamentally, this is achieved by removing heat from a low temperature heat source and transferring it to a high temperature heat sink, with an energy input as work.

The most widely used refrigeration technology, especially in the household and light commercial segments, is based on the mechanical compression and expansion of a volatile refrigerant, which boils at a low pressure to draw heat from the low-temperature thermal source (refrigerating effect) and condenses at a high pressure so heat is rejected at high-temperature heat sink.

Due to the amount of time and resources spent in developing this century-old technology, its components have been extensively optimized for efficiency, size and cost. Yet, the use of environmentally harmful refrigerants is still — and more than ever, a major concern regarding vapor compression refrigeration applications. According to the latest report of the International Institute of Refrigeration (IIR, 2019), the refrigeration sector accounts for 7.8% of global greenhouse effect gas emissions, in which 37% are direct emissions of HCFCs and HFCs refrigerants. Ongoing regulations such as the Montreal Protocol propose a complete phase out of HCFCs use in developed countries (by 2020) and in developing countries (by 2030). On that account, researches on alternative refrigerant fluids and alternative cooling technologies have heavily emerged in the past decades.

In the branch of not-in-kind cooling technologies, magnetic refrigeration is one with a very high potential to become a viable alternative to vapor compression (QIAN et al., 2016). Essentially, magnetic refrigeration substitutes the variation of the refrigerant fluid pressure in the vapor compression technology by a variation of magnetic field in a solid refrigerant. In response, the solid refrigerant exhibits the magnetocaloric effect (MCE), which is displayed as a temperature change if the process is adiabatic. Thus, a magnetocaloric material heats up when magnetized and cools down when demagnetized. Although the magnitude of MCE can be observed over a range of temperatures, it peaks near the so-called Curie temperature, which is a magnetic phase transition temperature from a ferromagnetic to a paramagnetic state.

The discovery of the MCE is attributed to the works of Weiss and Piccard, in 1917 and 1918 (SMITH, 2013), who also observed the reversible behaviour of the effect. Urbain, Weiss & Trombe (1935) observed magnetocaloric properties close to room temperature in Gadolinium (Gd). Brown (1976) demonstrated that Gd could be used as a refrigerant for magnetic refrigeration near room temperature, in what could be called the first-ever prototype of a magnetic refrigerator (KITANOVSKI, 2020). A pictorial representation of a simple magnetic

refrigeration cycle undergone by a solid refrigerant is presented in Fig. 1. The refrigerant, initially at room temperature (T_R), is adiabatically magnetized showing a temperature increase of ΔT_{ad}. With the refrigerant now above room temperature, heat can be rejected to the ambient, while the magnetic field is kept constant. After the material regains the thermal equilibrium at T_R, it is adiabatically demagnetized and has a temperature decrease of ΔT_{ad}. With the solid refrigerant now below room temperature, heat can be absorbed from the internal ambient, until the material again reaches thermal equilibrium at T_R.

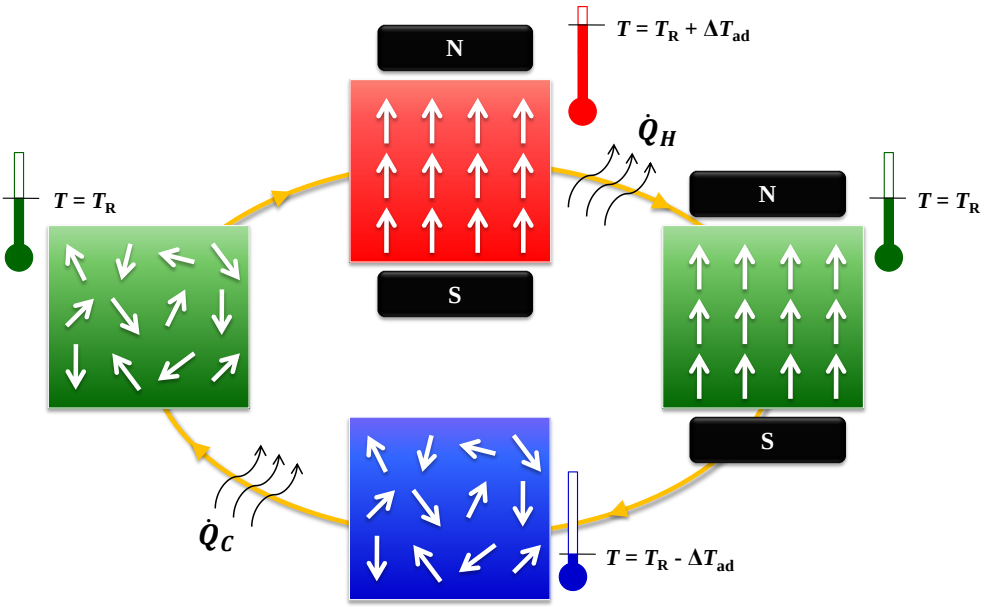

Figure 1 – Pictorial representation of magnetic refrigeration cycle (LOZANO, 2015).

With the prospects of an efficient and internally reversible cooling technology (TREVIZOLI, 2015), scientists and engineers prompted numerous developments in this area over the last two decades or so. So far, thousands of works have been published by more than 40 research groups around the world (KITANOVSKI et al., 2015), focusing on the development of new materials, design and analysis of magnetic circuits and optimization of components in terms of geometry and operating conditions (PEIXER, 2020). As a result, several magnetic refrigerator prototypes are being presently developed (KITANOVSKI, 2020).

1.1 Motivation and objectives

The above mentioned efforts dedicated to magnetic refrigeration research proved to be fairly successful at overcoming intrinsic limitations to develop magnetic refrigerators. However, the progress reported in the open literature is still at pre-competitive and pre-commercial stages, being more focused on developing and optimizing components, rather than the system as a whole (NAKASHIMA et al., 2020).

A typical prototype is composed of an active magnetic regenerator, or AMR (i.e., a porous regenerative matrix containing the magnetocaloric material), a magnetic circuit to promote the change in magnetic field and a hydraulic and control system synchronized with the magnetic field profile to promote the flow management (LOZANO, 2015). The cooling

load is usually imposed by electrical resistances and the temperature of the hot reservoir is usually controlled by thermal baths (KITANOVSKI, 2020; TREVIZOLI; BARBOSA, 2020). Additionally, the current setups are not concerned about how the heat exchangers and cabinet impact on the overall performance of the magnetic refrigerator (PEIXER et al., 2018), thus neglecting the impact of heat exchanger effectiveness, fan power dissipation and cabinet losses. Therefore, up to this point, no assessment on the maturity level of magnetic refrigeration compared to the the well-developed vapor compression refrigeration was yet performed.

In the past two years, the development of a magnetic wine cooler is in course by PoloMag, a research project focused on magnetic refrigeration at Polo - Research Laboratories for Emerging Technologies in Cooling and Thermophysics at the Federal University of Santa Catarina (UFSC), sponsored by Embraco and Embrapii. The research is supported by more than a decade of the group experience and it aims to optimize the entire system — studying the subsystems and its trade-offs simultaneously, and build the first setup in the magnetic refrigeration field with a real cabinet and real heat exchangers. An schematic representation of the magnetic wine cooler prototype is shown in Fig. 2.

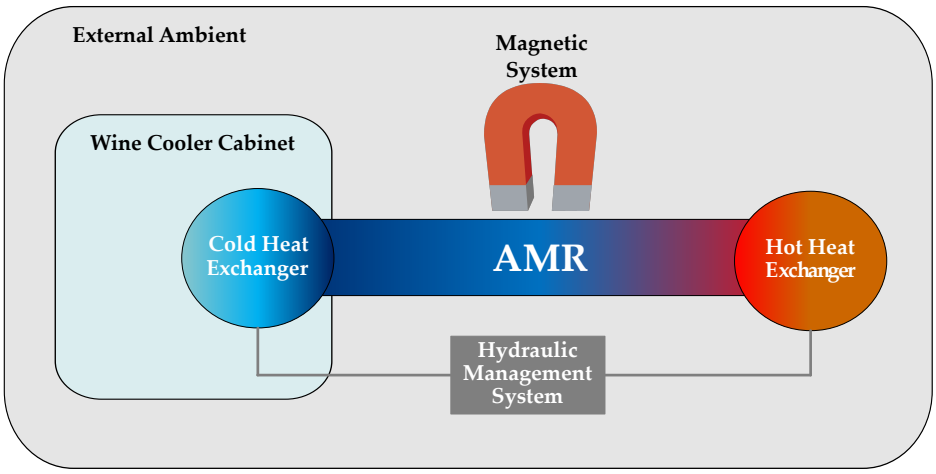

Figure 2 – Schematic representation of the magnetocaloric wine cooler system designed by PoloMag and its main components. Adapted from Peixer (2020).

Given the observed lack in the literature of studies reporting the current maturity level of magnetic refrigeration and a fair comparison with the vapor compression technology, the main objective of this work is to experimentally evaluate and compare the thermodynamic performances of both cooling technologies operating the same wine cooler cabinet. In order to fulfill this goal, the following specific objectives have been proposed:

- Characterize experimentally the thermodynamic performance of a commercially available wine cooler operated by a vapor compression cooling system;
- Build the designed magnetic wine cooler prototype developed by the PoloMag project with the same cabinet of the vapor compression wine cooler, coupling it with real heat exchangers;

- Characterize the thermodynamic performance of the wine cooler operating with magnetic cooling technology and evaluate the main sources of losses, identifying the most important points to be improved;
- Compare experimentally the performances of the magnetic and vapor compression cooling technologies operating the same wine cooler cabinet, to point out the current development stage of magnetic refrigeration and how further still it must progress to become a viable alternative to vapor compression refrigeration in terms of performance.

1.2 Thesis Overview

This thesis is divided into five chapters. Chapter 2 reviews the concepts of the vapor compression and magnetic refrigeration technologies, pointing out the main theoretical fundamentals to be used in the thesis. Chapter 3 presents the experimental evaluation and thermodynamic analysis of the vapor compression wine cooler and the magnetic wine cooler prototype. Also, Chapter 3 includes a detailed description of the designing phase and construction features of the magnetic prototype, pointing out the main decisions of each subsystem. Chapter 4 presents the results of the experimental characterization of the wine cooler operating with both cooling technologies, as well as the thermodynamic comparison between both magnetic and vapor compression cooling technology. Additionally, improvement points for the prototype are suggested based on the thermodynamic analysis results and further analysis. Lastly, Chapter 5 presents the conclusions of the thermodynamic analysis and comparison, assessing the level of maturity and the gap between technologies, as well as recommendations for future works.

2 Literature Review

This chapter presents a review on the concepts of the vapor compression refrigeration and the magnetocaloric refrigeration technologies. Initially, the operational principle and main components of the vapor compression systems are described, with a further review on several works in the field to assess the most important characterization tests of vapor compression refrigerators. Next, the fundamental principles of operation of a magnetocaloric refrigerator, with a review on the MCE — from a basic thermodynamics point of view, a review on AMRs and its most relevant performance parameters and a review on the state-of-the-art of magnetic refrigeration — in terms of the main components, the most relevant prototypes and their performances. Lastly, a review on the thermodynamic evaluation of cooling devices when comparing the application of different operational technologies.

2.1 Conventional Refrigeration System

Cooling devices as currently known produce cold mainly by artificial means, with common technologies such as the vapor compression refrigeration, the absorption refrigeration, the thermoeletric refrigeration and the magnetocaloric refrigeration (HERMES, 2006). The most conventional cooling technology is the vapor compression[1], based on the mechanical compression and expansion of refrigerant fluids. As presented in Fig. 3, the conventional refrigeration system is designed with 5 components: a compressor, a condenser, an expansion device, an evaporator and an internal heat exchanger (IHX). The compressor guarantees the fluid circulation with the conversion of electrical energy into flow work and establish the region of high pressure into the system (condensation pressure). The condenser rejects heat to the external environment as a result of the fluid condensation. The expansion device, usually a capillary tube, expands the fluid and establish the region of low pressure into the system (evaporation pressure). The evaporator removes heat from the refrigerated compartment as a result of the fluid evaporation. Lastly, the IHX, a counter-current heat exchanger, increases the cooling capacity of the system and avoids liquid in the compressor inlet by subcooling the fluid before the expansion and superheating the fluid before the compression.

In the refrigeration cycle presented in Fig. 3, the fluid enters the compressor as superheated vapor at the low pressure level (point 1), where it is compressed to the level of high pressure and temperature. The fluid exits the compressor as superheated vapor at the high pressure level and enters the condenser (point 2), where heat is rejected to the surroundings ($\dot{Q}_H$). The fluid exits the condenser as saturated liquid at the high pressure level and enters the IHX (point 3), where it is subcooled through the heat exchange with the suction line. The fluid exits the IHX as subcooled liquid at the high pressure level and enters the expansion device (point 3'), where it is expanded to the level of low pressure and temperature. The fluid exits the expansion device as a saturated mixture of liquid and vapor at the low pressure

[1] In this thesis, this technology will be referred as either vapor compression or conventional.

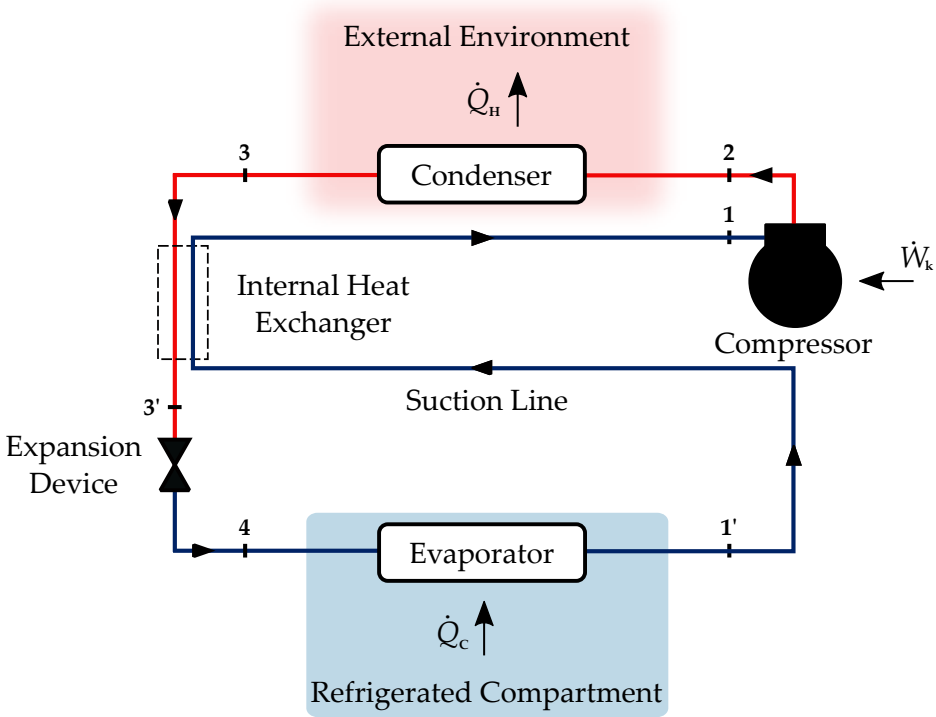

Figure 3 – Schematic representation of a refrigeration system operating with vapor compression technology.

level and enters the evaporator (point 4), where heat is removed from the compartment to be refrigerated ($\dot{Q}_C$). The fluid exits the evaporator as saturated vapor and enters the IHX (point 1′), where it is superheated before entering the compressor, completing the cycle. In a temperature *versus* entropy diagram (*T*-*s*), the described refrigeration cycle is as follows in Fig. 4.

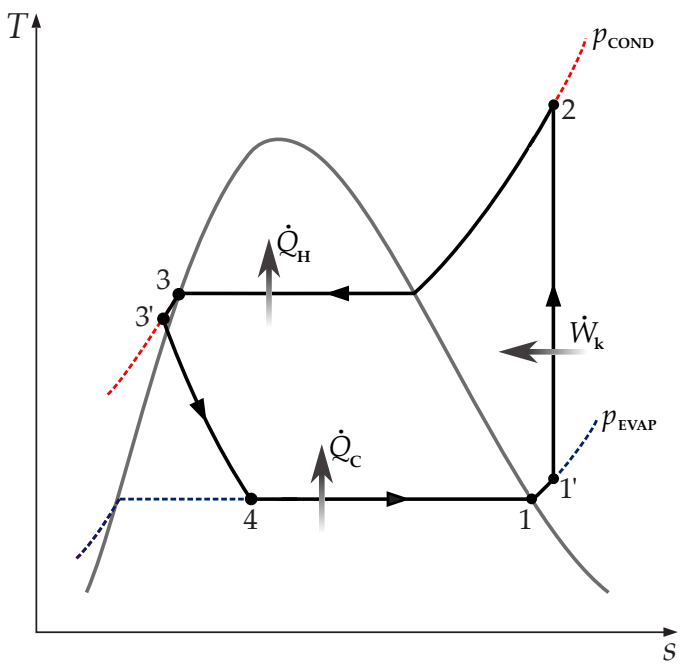

Figure 4 – *T*-*s* diagram of the conventional refrigeration cycle.

In real systems, irreversibilities due to viscous losses and non-adiabatic components

lead to a cycle far from ideal in terms of performance, triggering years of studies on the improvement of the single components of the conventional refrigeration cycle. In order to assess the evolution of components and compare the performance of different systems, standardized tests were developed to characterize and classify the products to a number of categories over the years.

2.1.1 Characterization of Household Refrigerators

According to the IEC 62552 (2015) standard for household refrigerating appliances, a test report regarding the characterization of wine storage appliances shall include the test results of energy consumption and temperature stratification, besides details about the bottle capacity of each compartment. In order to assess more information on performance metrics of the conventional wine cooler, additional tests must be carried out.

Polo Laboratories have been dedicating efforts in groundbreaking research in the refrigeration field since 1982. In more than three decades of research engagement, Polo developed several works regarding improvements and optimization of refrigeration systems aligned with interests of industry. Hence, the development of the test methodology for the characterization of the conventional wine cooler in this thesis was based in the works developed at Polo, with highlights presented as follows.

Gonçalves et al. (2000) proposed a test method to assess the quality of the thermal insulation and the heat transfer through the refrigerator walls. The so called reverse heat leakage test consists in calculating the overall thermal conductance of the refrigerator (UA) with an analytical model of the conservation of energy applied in the control volume of the cabinet, in steady state conditions. During the test, the cooling system remains switched off and the compartments of the refrigerator are heated to temperatures higher than the temperature of the surroundings, so as to maintain a constant heat flux into the external ambient direction. With steady state condition, the temperatures of the compartments and ambient are accounted and the UA is calculated.

Hermes (2006) developed a methodology to emulate the transient behavior of a domestic refrigerator, during both the pull down and the cyclic operation. The methodology was based on the development of a mathematical model for each component of the refrigerator, with inputs and further validation of data generated from a baseline product. The transient behavior of the baseline product was characterized with tests of energy consumption in cyclic operation and pull down. Also, the reverse heat leakage test was carried out to assess the UA of the refrigerator and to calculate the portion of the thermal load imposed by the heat transfer through the refrigerator walls and gasket.

Hermes et al. (2009) proposed a methodology to predict the energy consumption of domestic refrigerators and freezers via steady state simulation. The methodology was validated with data from a baseline product tested for energy consumption in steady state regime. The energy consumption tests in steady state were carried out with the compensation of the exceeded cooling capacity by means of heat generation inside the refrigerator compartments. The heat was generated with PID-driven electrical resistances and during

the test the thermostat was switched off and the damper was fixed at a predefined condition, so as to carry out the test with a full time running compressor. To evaluate the performance metrics of the refrigerator as well as the compressor runtime, it was necessary to assess the *UA* of the refrigerator compartments, which was achieved with the reverse heat leakage test proposed by Gonçalves et al. (2000). The methodology aimed not to be a replacement to the standardized energy consumption test, but to provide a reliable and much faster procedure to be used as guide in the conception and development phase of refrigerators.

Boeng (2012) developed a methodology to select the pair capillary tube and refrigerant charge that maximizes the performance of domestic refrigerators. The methodology was based in an experimental apparatus capable of provide several combinations of refrigerant charge and restrictions in the expansion device, thus emulating different capillary tubes. Tests were carried out with the aim of developing an energy consumption map as a function of the pair combinations, so as to identify the operation point of the refrigerator. To reduce the time associated with the tests for the energy consumption, the steady state approach proposed by Hermes et al. (2009) was adopted. Also, the reverse heat leakage test proposed by Gonçalves et al. (2000) was carried out to assess the portion of heat load imposed by the surroundings through the evaluation of the *UA* of the refrigerator.

Thiessen (2015) carried out a study on the effectiveness of applying vacuum insulation panels in domestic refrigerators. The study was based on the comparison of a baseline product with PU insulation and sixteen samples with different configurations of the vacuum panels. The comparison was achieved through the evaluation of the *UA* with the reverse heat leakage test proposed by Gonçalves et al. (2000), and the energy consumption in periodic steady state. For the energy consumption tests, the author proposed a modified approach from the standardized procedure of IEC 62552 (2015), that demands 24 hours of recording data with an integer number of compressor cycles, two defrosting cycles and a freezer compartment loaded with tylose packages. In order to reduce time and disadvantages associated with the standardized test, the author performed tests with 5 hours of an integer number compressor cycles, with no defrosting cycle and no tylose packages.

Espíndola (2017) carried out a study on the overall thermal performance of refrigerators with skin condensers. The study was based in the development of a mathematical model for the skin condenser coupled with a model for the refrigeration system and a further comparison with the thermal performance of a baseline product with wire-and-tube condenser. The model was validated with the data from eight modified refrigerators with different geometric configurations of skin condenser. The comparison between the condensers and the model validation were achieved through the evaluation of the *UA* with the reverse heat leakage test proposed by Gonçalves et al. (2000), the steady state energy consumption test proposed by Hermes et al. (2009) and the modified periodic state energy consumption test proposed by Thiessen (2015).

Marcon (2017) carried out an experimental study on the performance of a built-in refrigerator in accordance with the IEC 62552 (2015) standard. The author proposed several alterations with the aim of optimizing the refrigerator by means of performance and energetic metrics. The alterations were implemented on the charge of refrigerant, the amplitude

of the thermostat control, the external heat exchanging area of the wire-and-tube condenser and addition of phase changing material into the condenser. The comparison between the refrigerator samples was achieved through the evaluation of the energy consumption, assessed with the standardized energy consumption test in cyclic operation, and through pull down tests to assess the initial transient curve of the systems.

On accounting the aforementioned works, typical tests to characterize conventional cooling appliances regarding comparison and optimization purposes are the reverse heat leakage test, the energy consumption, whether in cyclic or steady state operation, and the pull down test. Thus, these tests were considered during the planning of characterization phase of the conventional wine cooler, for the further comparison with the magnetic wine cooler.

2.2 Magnetic Refrigeration System

2.2.1 The Magnetocaloric Effect

The magnetocaloric effect (MCE) is the thermal response of a magnetic material due to the application of an external magnetic field (H). The thermal response is a consequence of the coupling between the magnetic sublattice of the material and the magnetic field, which alters the magnetic portion of the total entropy. According to Tishin & Spichkin (2003), the total entropy of some magnetocaloric materials at constant pressure can be suitably approximated as a contribution of three main portions, as presented in Eq. (2.1).

$$s(T,H) \approx s_{\text{ele}}(T) + s_{\text{lat}}(T) + s_{\text{mag}}(T,H) \tag{2.1}$$

where s_{ele} is the electronic portion, s_{lat} is the lattice portion and s_{mag} is the magnetic portion. The electronic and lattice portions are mainly a function of the temperature, while the magnetic portion is a function of both the temperature and the magnetic field. Thus, the total entropy of the magnetic material is also a function of the temperature and the magnetic field.

The manifestation of the MCE can be obtained with two different thermodynamic processes: an isothermal magnetization or an adiabatic magnetization. Regardless, the magnetization of the magnetocaloric material induces a negative variation in the magnetic entropy portion, as the magnetic field imposes a degree of order on the magnetic spin ($\Delta s_{\text{mag}}(T,H) < 0$). In an isothermal magnetization, the variation of the electronic and lattice entropy portions are zero, and the total entropy variation equals the variation of the magnetic portion (Eq. (2.2)). As the variation of the magnetic entropy is negative, so is the variation of the total entropy, which is physically translated as a heat rejection to the surroundings.

$$\Delta s_{\text{iso}}(T,H) \approx \cancelto{0}{\Delta s_{\text{ele}}(T)} + \cancelto{0}{\Delta s_{\text{lat}}(T)} + \Delta s_{\text{mag}}(T,H)$$

$$\Delta s_{\text{iso}}(T,H) \approx \Delta s_{\text{mag}}(T,H) \tag{2.2}$$

In an adiabatic magnetization, the total entropy variation is zero, and the sum of the variation of the electronic and lattice entropy portions increase to compensate the negative variation of the magnetic entropy (Eq. (2.3)). This increase of the electronic and lattice entropy portions are physically translated as an increase in the temperature of the material, resulting in the adiabatic temperature variation ΔT_{ad}.

$$\cancelto{0}{\Delta s(T,H)_{\mathrm{ad}}} \approx \Delta s_{\mathrm{ele}}(T) + \Delta s_{\mathrm{lat}}(T) + \Delta s_{\mathrm{mag}}(T,H)$$

$$\Delta s_{\mathrm{ele}}(T) + \Delta s_{\mathrm{lat}}(T) \approx -\Delta s_{\mathrm{mag}}(T,H) \tag{2.3}$$

In a more classical thermodynamic approach, the entropy variation of a magnetocaloric material can be described as in Eq. (2.4), assuming conditions of constant pressure and volume.

$$ds = \left(\frac{\partial s}{\partial T}\right)_{\mathrm{H}} dT + \left(\frac{\partial s}{\partial H}\right)_{\mathrm{T}} dH \tag{2.4}$$

For magnetic processes, the specific heat at a constant magnetic field, c_{H}, is defined as in Eq. (2.5) (KITANOVSKI et al., 2015).

$$\frac{c_{\mathrm{H}}}{T} = \left(\frac{\partial s}{\partial T}\right)_{\mathrm{H}} \tag{2.5}$$

The Maxwell relation presented in Eq. (2.6) can be used to relate the entropy with the specific magnetization, σ, originated from the thermodynamic identity for the Gibbs free energy.

$$\left(\frac{\partial s}{\partial H}\right)_{\mathrm{T}} = \left(\frac{\partial \sigma}{\partial T}\right)_{\mathrm{H}} \tag{2.6}$$

By applying Eq. (2.5) and Eq. (2.6) in Eq. (2.4), an infinitesimal specific entropy variation is given by Eq. (2.7).

$$ds = c_{\mathrm{H}}\frac{dT}{T} + \left(\frac{\partial \sigma}{\partial T}\right)_{\mathrm{H}} dH \tag{2.7}$$

Considering the magnetization carried out in isothermal or adiabatic conditions, as previously stated, the fundamental quantities Δs_{iso} and ΔT_{ad} can be derived, respectively, and are presented in Eq. (2.8) and Eq. (2.9).

$$\Delta s_{\mathrm{iso}} = \int_{H_0}^{H_1} \left(\frac{\partial \sigma}{\partial T}\right)_{\mathrm{H}} dH \tag{2.8}$$

$$\Delta T_{\mathrm{ad}} = -\int_{H_0}^{H_1} \frac{T}{c_{\mathrm{H}}}\left(\frac{\partial \sigma}{\partial T}\right)_{\mathrm{H}} dH \tag{2.9}$$

Figure 5 presents the two processes described previously in a entropy *versus* temperature (S-T) diagram. Two lines of constant magnetic field H_{i} and H_{f} represent the magnetic field variation. The vertical line represents the entropy change of the material due to the

isothermal (Δs_{iso}) magnetization from H_i to H_f, and the horizontal line represents the adiabatic temperature variation of the material due to the adiabatic magnetization (ΔT_{ad}) from H_i to H_f.

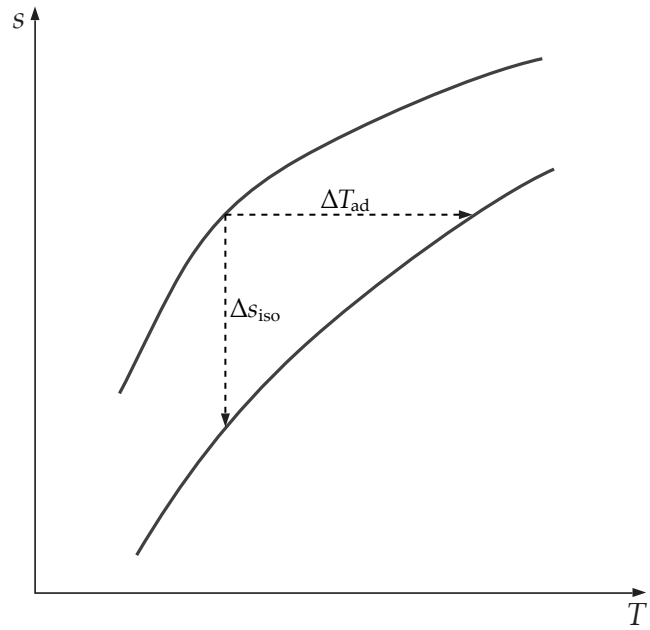

Figure 5 – Schematic representation of the adiabatic and isothermal magnetization processes in a *s*-*T* diagram. Adapted from Smith et al. (2012).

The MCE is an intrinsic property to all magnetic materials, but differs in the magnitude. A material can only be considered magnetocaloric when it exhibits a perceptible MCE (LOZANO, 2015), considered as a ΔT_{ad} manifestation of at least 2 K per tesla (LYUBINA, 2017). The magnitude of the MCE is a function of the material temperature, and the highest manifestation of the effect occurs for a certain temperature in each material. For ferromagnetic materials[2], the highest MCE is achieved near the magnetic transition temperature, known as Curie temperature (T_{Curie}). Thus, for a cooling system applied at near room temperature, the T_{Curie} of the magnetocaloric refrigerant shall desirably be at near room level. The benchmark magnetocaloric material for near room temperature applications is the Gadolinium (Gd), with a T_{Curie} usually in the range of 290 to 297 K (17 to 24ºC) and with a ΔT_{ad} of around 3.0 K for a magnetic field of 1.0 T (BAHL; NIELSEN, 2009). Trevizoli et al. (2012) carried out an experimental analysis of the MCE reversibility for a commercial Gd sample over almost instantaneous magnetization and demagnetization. As it can be seen in Fig. 6, for a change in the magnetic field of 1.65 T, the exhibited ΔT_{ad} was of about 3.8 K.

Although household and commercial cooling devices demand normally a temperature span between the hot and cold sources in the order of 40 K or more, the magnitude of the MCE exhibited by Gd is of few kelvin. Thus, from an application point of view, reaching larger temperature span is essential to the feasibility of magnetic cooling devices. The most spread alternative to achieve a larger temperature span is through thermal regeneration with the employment of active magnetic regenerators.

[2] From this point onwards in this thesis, only ferromagnetic materials will be considered when referring to magnetocaloric materials.

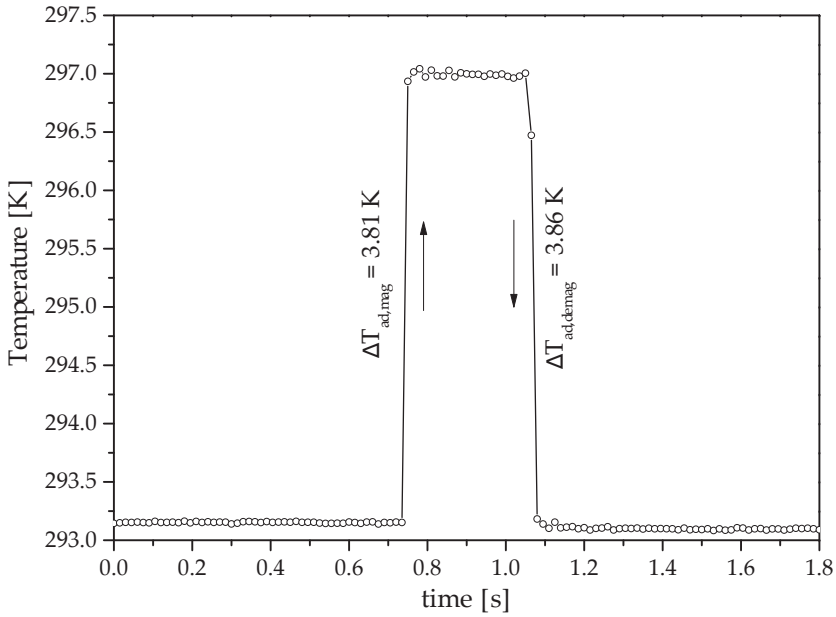

Figure 6 – Experimental demonstration of the MCE reversibility in a commercial Gd sample over almost instantaneous magnetization and demagnetization. Adapted from Trevizoli et al. (2012)

2.2.2 *Active Magnetic Regenerators*

Magnetic refrigeration systems can be built according to different thermodynamic cycles, such as Ericsson, Stirling and Brayton (KITANOVSKI et al., 2014). As the MCE of Gd is too small for near room temperature cooling applications, regenerative cycles enable the achievement of larger temperature spans and larger cooling capacities (TREVIZOLI, 2015). The most common regenerative thermo-magnetic cycle is the Brayton cycle, performed in an active magnetic regenerator (AMR) (BARCLAY; STEYERT, 1982). An AMR is a regenerator assembled with a porous matrix of magnetocaloric material, acting not only as a medium of energy storage but also as the refrigerant. With a cyclic operation of magnetization and demagnetization of the AMR and the use of a heat transfer fluid as a thermal exchange medium between the solid refrigerant and the cold and hot reservoirs, the temperature span between the cold and hot ends of the regenerator can reach larger values than the limited ΔT_{ad} of the MCE (LOZANO, 2015). The thermo-magnetic Brayton cycle undergone by one portion of the active magnetic regenerator (AMR cycle) is represented in Fig. 7, in a temperature *versus* entropy diagram (*T*-*s*), and it can be explained in the following idealized steps (ROWE et al., 2005):

- *Adiabatic magnetization*: the magnetic field applied to the solid refrigerant is adiabatically increased, raising the temperature of the matrix by $\Delta T_{\mathrm{ad}}(T, \Delta H)$ due to the MCE;

- *Cold-to-hot period (or cold blow)*: the matrix rejects heat to the cold fluid coming from the cold source, decreasing the matrix temperature and increasing the fluid temperature at the hot end to a higher level than that of the hot sink, so as to enable sensible heat rejection;

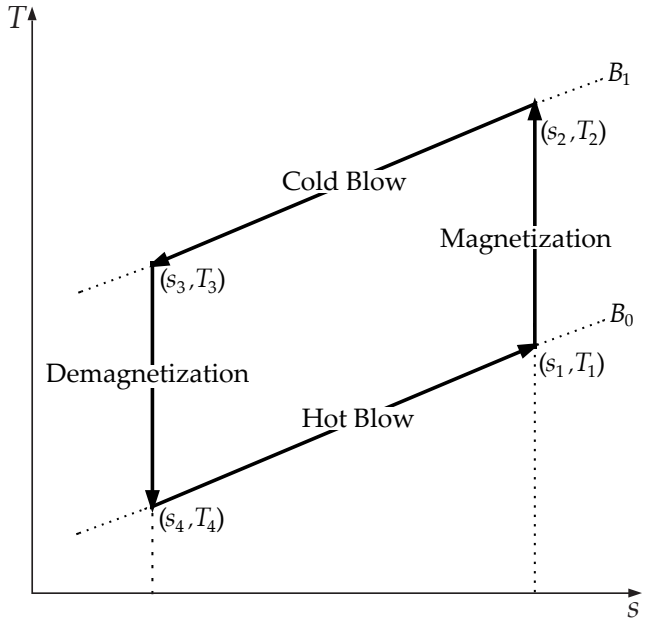

Figure 7 – *T-s* diagram of the Brayton cycle undergone in an AMR (TREVIZOLI, 2015).

- *Adiabatic demagnetization*: the magnetic field applied to the solid refrigerant is adiabatically reduced, decreasing the temperature of the matrix by $\Delta T_{\text{ad}}(T, \Delta H)$ due to the MCE;
- *Hot-to-cold period (or hot blow)*: the matrix absorbs heat from the fluid returning from the hot thermal sink, increasing the matrix temperature and decreasing the fluid temperature at the cold end to a lower level than that of the cold source, enabling sensible heat absorption.

In an schematic representation, the AMR cycle is presented in Fig. 8.

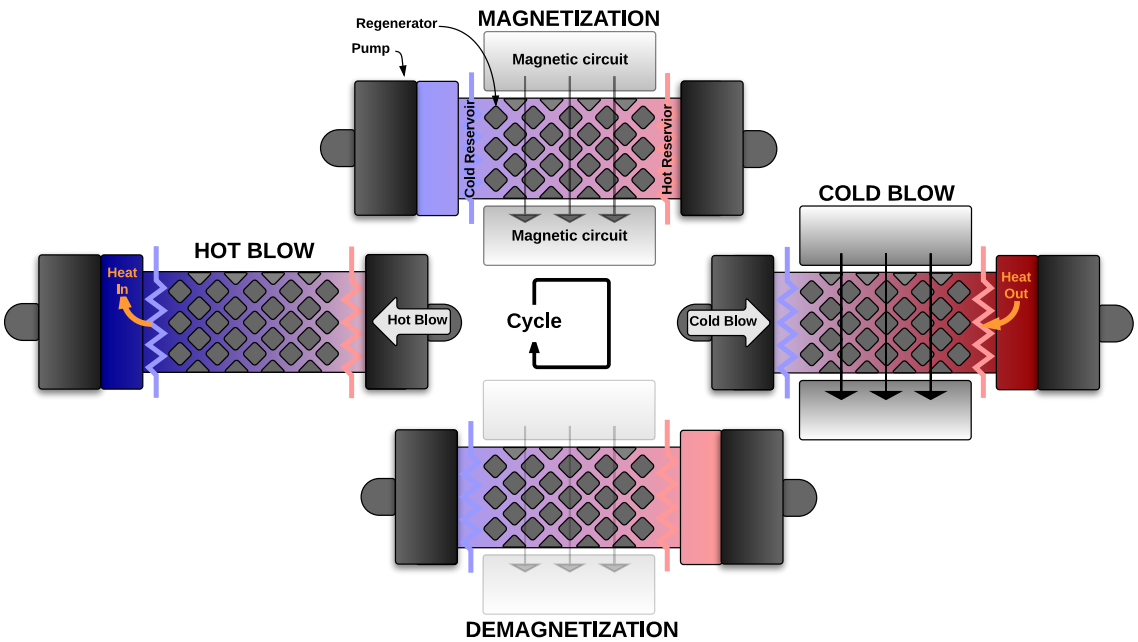

Figure 8 – Schematic representation of the AMR cycle and its main components (TREVIZOLI, 2015).

2.2.3 Performance Parameters of Active Magnetic Regenerators

The efficiency of a magnetic cooling system is highly dependent on the effectiveness of the regenerative matrix. The regenerator effectiveness depends on the solid phase thermophysical properties, matrix geometry, thermal capacity, porosity and operating parameters, such as frequency and flow velocity (ROWE et al., 2005; TURA; ROWE, 2011; NIELSEN et al., 2012; TREVIZOLI et al., 2014). This parameters are related more commonly by two dimensionless groups: the utilization factor (or simply utilization), ϕ, and the number of transfer units, NTU. The utilization is the ratio of the thermal capacity of the working fluid flowing through the regenerator during one blow (hot or cold) and the thermal capacity rate of the regenerator solid matrix, defined by Eq. (2.10) (SHAH; SEKULIĆ, 2003; ROWE et al., 2005).

$$\phi = \frac{\dot{m}_{\mathrm{f}} c_{\mathrm{p,f}} \tau_{\mathrm{blow}}}{m_{\mathrm{s}} c_{\mathrm{s}}} \tag{2.10}$$

where $\dot{m}_{\mathrm{f}}$ is the mass flow rate of the fluid, $c_{\mathrm{p,f}}$ is the specific heat of the fluid, τ_{blow} is the time period of the blow, m_{s} is the mass of the solid matrix and c_{s} is the specific heat of the solid matrix. The NTU is the ratio of the overall thermal conductance and the thermal capacity of the fluid in one blow, defined by Eq. (2.11) (NELLIS; KLEIN, 2009).

$$NTU = \frac{U A_{\mathrm{HT}}}{\dot{m}_{\mathrm{f}} c_{\mathrm{p,f}}} \tag{2.11}$$

where U is the overall heat transfer coefficient and A_{HT} is the heat transfer area. The regenerator effectiveness, ϵ, is usually expressed as a function of both the utilization and the NTU. Fig 9 presents an example of the relation $\epsilon = f(\phi, NTU)$, for a symmetrical and balanced regenerator, with the effectiveness as a function of NTU for different utilization factors. As can be seen, only regenerators with an utilization lower than the unity are capable of achieving 100% of effectiveness and the lower the utilization is, earlier this limit is achieved. For utilizations higher than the unity, the effectiveness achieve a maximum value below 100% and the higher the utilization is, earlier the asymptotic limit is achieved. In a general conclusion, the effectiveness is higher as lower is the utilization and higher is the NTU, save the cases in the asymptotic limit region. Thus, it is desirable for a more effective regenerator to have a porous matrix with high thermal capacity and a working fluid with a thermal capacity lower than that of the matrix. Also, a short blow period, or a higher blow frequency, provide more effective regenerators.

Another parameter that greatly affects the performance of the AMR is the MCE itself (ENGELBRECHT; BAHL, 2010). As previously discussed, the MCE is maximum when near the T_{Curie} of the magnetocaloric material. As the temperature of the matrix moves away from this point, the magnitude of the MCE can drop sharply. That said, if an AMR has a fixed T_{Curie} along its length, the temperature profile that is established in the AMR during its operation contributes to the degradation of the MCE, specially in the final portions of its length, as the temperature is smaller in this region. This problem is usually overcame through the use of layered regenerators, i.e. regenerators whose composition — such as the T_{Curie}, varies

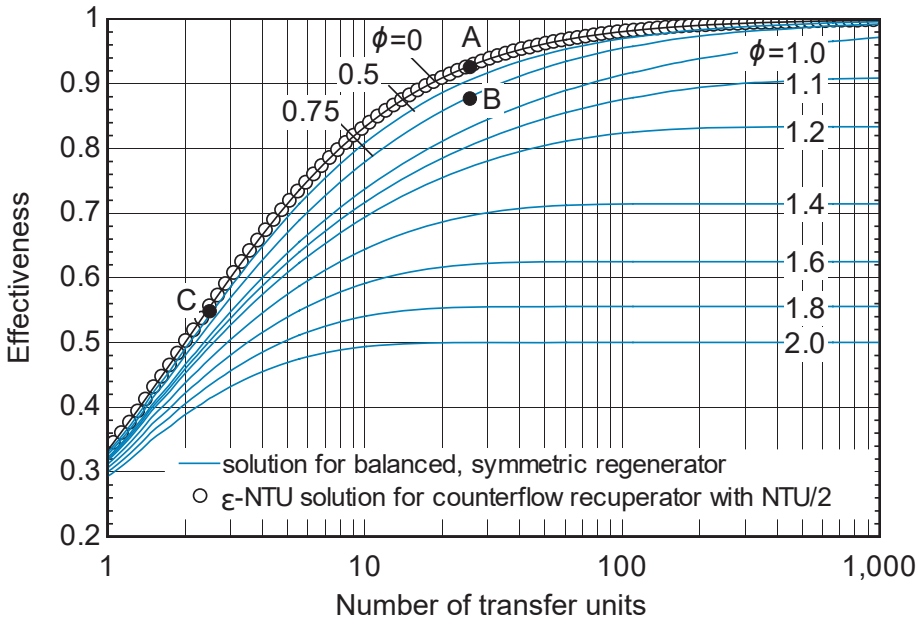

Figure 9 – Regenerator effectiveness as a function of the *NTU* and the utilization. Adapted from Nellis & Klein (2009).

spatially along its length. With a layered regenerator, the T_{Curie} profile can follow the local average temperature in steady state during the system operation and the AMR performance can be enhanced. The degradation of the MCE is also highly influenced by the temperature of the heat sink in which the cooling system is installed. If the system is intended to work at a determined temperature of heat sink, the first layers of the regenerator shall have T_{Curie} near that temperature. If the heat sink temperature is varied to higher or lower levels during the system operation, the MCE will degrade and the AMR performance will reduce.

2.2.4 *Overview on Magnetocaloric Refrigerator Prototypes*

A typical magnetocaloric refrigerator utilizes magnetocaloric materials in the form of a regenerative matrix (AMR) associated with a magnetic field, normally generated by permanent magnets. A heat transfer fluid, usually water containing inhibitors, oscillates through the regenerators with the control of valves, in synchrony with the periodic magnetization/demagnetization. The fluid oscillation is enabled by a hydraulic pump, which also connects the AMR with the external heat source and the heat sink heat exchangers (Adapted from Kitanovski (2020)).

The method through which the magnetization/demagnetization is achieved classify the magnetic systems into reciprocating and rotary. A reciprocating system is characterized by a linear, back and forth movement. This can be achieved either by moving the regenerator in and out of a stationary magnet or by moving the magnet in and out of a stationary regenerator. A rotary system is characterized by a rotating motion, which can be achieved either by rotating the regenerator or the magnet. Reciprocating devices are usually used for small scale systems and testing devices, running with one or two regenerators at frequencies below 1 Hz (LEI, 2016). Rotary devices, on the other hand, are usually used for larger systems and can achieve higher frequencies. Also, rotary prototypes are much closer to eventually

what would become a commercial product (TREVIZOLI; BARBOSA, 2020), therefore being the most common of the magnetic prototypes.

Some of the most relevant and more recent magnetic refrigerator prototypes reported in literature are briefly described in the following paragraphs, with highlights of the best operating points. A thorough description of these machines is beyond the scope of this thesis.

Tura & Rowe (2011) developed a compact magnetic refrigerator for near room temperature applications at the University of Victoria (UVic), which consisted of two rotary magnetic circuits, generating magnetic fields in the range 0.1 to 1.4 T, and two stationary regenerators, with 110 g of Gd spheres in total. A mixture of water and ethylene-glycol (80-20%) was employed as heat transfer fluid. The prototype was able to achieve 10ºC of regenerator temperature span and 50 W of cooling capacity, at a maximum operating frequency of 4 Hz and an utilization of 0.62. A maximum *COP* of 1.6 was obtained at an operating frequency of 1.4 Hz, for 2.5ºC of regenerator temperature span and 50 W of cooling capacity. The *COP* calculation included all motor inefficiencies and drive loss. It was claimed by the authors that the *COP* could be increased to 2.2 if the motor inefficiencies were removed.

Engelbrecht et al. (2012) developed a magnetic refrigerator prototype for near room temperature applications at the Technical University of Denmark, which consisted of two concentric Halbach array[3] stationary magnet, with a peak of magnetic field of 1.24 T, and 24 rotating regenerators mounted around and within the two concentric magnets with 2.8 kg of Gd spheres. A mixture of water and ethylene-glycol (75-25%) was used as heat transfer fluid. The thermal load was emulated by a resistance heater and the temperature of the hot side of the AMR was controlled by a counter-flow heat exchanger connect to a thermal bath. The prototype was able to achieve 15.4ºC of regenerator temperature span and 200 W of cooling capacity operating at an operating frequency of 1 Hz and flow rate of 6.7 L/min. The *COP* achieved was 0.8, which included inefficiencies in the pump, in the rotating system and in the valves.

Jacobs et al. (2014) developed a large scale rotary magnetic refrigerator at Astronautics Corporation of America (USA), intended to meet the preliminary performance specifications of a supplemental electronics cooler used in Naval applications. The system was designed for operation above room temperature, with a hot inlet fluid temperature of 44ºC and cold inlet fluid temperature of 32ºC. The magnetic refrigerator consisted of a Halbach cylinder array as magnet with a peak of magnetic field of 1.44 T and 12 regenerators with six layers of La-Fe-Si-H alloys, adding up 1.52 kg of magnetocaloric material. On the cold side, an electrical heater emulated the thermal load of the system and on the hot side the heat exchanger was connected to a thermal bath, which controlled the regenerator inlet temperature at the hot end. For a mass flow rate of 1272 kg/h and a frequency of 4 Hz, the magnetic refrigerator was able to achieve 12ºC of regenerator temperature span and 2090 W of cooling capacity, corresponding to a *COP* around 2.

Eriksen et al. (2015) developed a new generation of prototype in the Technical University of Denmark, which consisted of a Halbach array rotary magnet with 1.13 T of magnetic

[3] The Halbach array is an arrangement of permanent magnets in a cylindrical shell that creates a uniform magnetic field in one side of the array and cancels the magnetic field in the other side.

field and 11 regenerators mounted within the magnet. The regenerators had one layer of Gd and 3 layers of Gd-alloys, with 1.7 kg of magnetocaloric material in total. A mixture of water and ethylene-glycol (95-5%) was used as heat transfer fluid. The thermal load was emulated by an electrical heater in the cold side and the excess of heat in the hot side was rejected in a heat exchanger, with a hot side temperature held constant at 18ºC. The prototype was able to achieve 10.2ºC of regenerator temperature span and 103 W of cooling capacity at an operating frequency of 0.75 Hz and a flow rate of 3 l/min. The *COP* achieved was 3.1. The authors concluded that a considerable power consumption was caused by auxiliary components — 21% for the pumping through external components and 7% due to friction and losses in gears and bearings.

Lozano et al. (2016) developed a magnetic refrigerator at the Federal University of Santa Catarina, in the Research Laboratories for Emerging Technologies in Cooling and Thermophysics - POLO. The apparatus consisted in a rotary magnet with a peak of magnetic field of 1 T and 16 stationary regenerators with 1.7 kg of Gd. A mixture of water and ethylene-glycol (80-20%) was used as heat transfer fluid. On the cold side, the heat load was emulated by an electrical heater and on the hot side the temperature of the regenerator inlet was controlled by a heat exchanger coupled to a thermal bath. The prototype was able to achieve 7.1ºC of regenerator temperature span for a cooling capacity of 80.4 W, at 0.8 Hz and 200 L/h. The *COP* and second-law efficiency were 0.54 and 1.16%, respectively. Capovilla et al. (2016) demonstrated that the valves were the major energy consuming components of the transmission system, having the total transmission power always reached higher values than the pumping power, for the experiments performed.

Fig. 10 summarizes the main parameters of the works described.

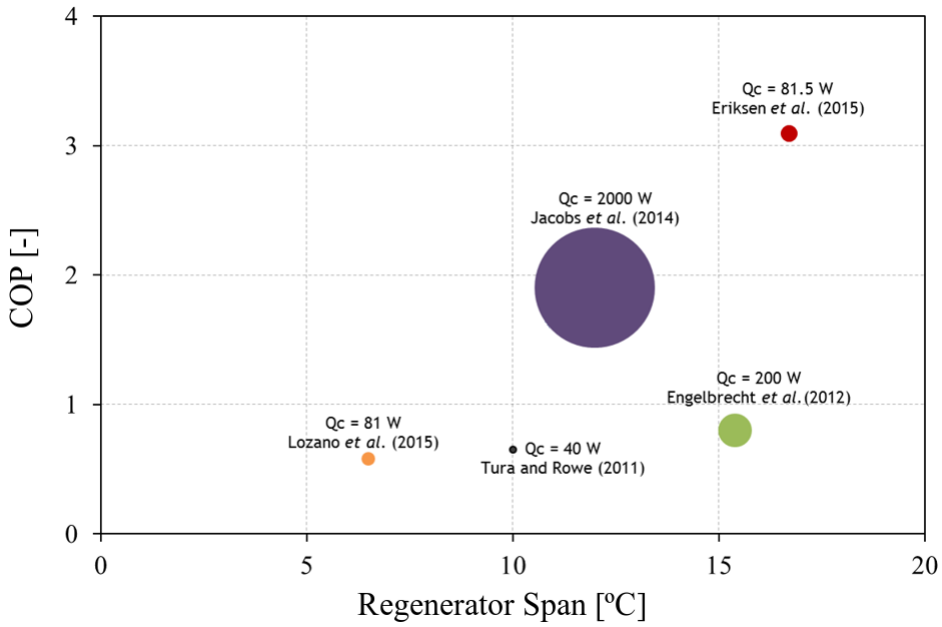

Figure 10 – *COP* as a function of the regenerator temperature span for selected magnetic refrigeration devices. The size of the circles are proportional to the cooling capacity $\dot{Q}_c$.

A key fact to be learned from these works is that none of them — as well as most of the work reported in literature, have tested their devices with a cabinet as refrigerated environment and a real heat exchanger in the cold side. So far, the thermal load — and therefore the cooling capacity, is usually emulated by electrical heaters. Also, most of the works control the inlet temperature of the regenerator in the hot side, which does not reflect truthfully a real application of the magnetic cooling devices as refrigerators. On that account, however advanced is the knowledge on AMR and magnet design, there is still a lack of knowledge on the system behavior operating a real cabinet and real heat exchangers, and how close the magnetic refrigeration is from the vapor compression technology.

2.3 Performance comparison between cooling technologies

The most common performance parameter used to characterize refrigeration systems is a first-law based efficiency, widely known as the coefficient of performance — *COP*. The *COP* is given by the relation between the net capacity to remove the heat and the amount of energy spent in order to remove it (GOSNEY, 1982). Thus, the *COP* is the ratio between the cooling capacity, $\dot{Q}_C$, and the electric power consumed by the product, $\dot{W}$, as presented in Eq. (2.12):

$$COP = \frac{\dot{Q}_C}{\dot{W}} \tag{2.12}$$

Regardless of the type of the refrigeration system, when comparing alternatives or even the same cooling technology, solely based first-law efficiency can be misleading or incomplete, specially if the systems are operating at different source and sink temperatures and if the cooling capacity is not fixed. Therefore, it is appropriate to compare different systems using performance indexes based on both the first and second law of thermodynamics (BROWN; DOMANSKI, 2014).

The performance parameter based on the second law is known as the second-law efficiency — η_{2nd}, and it can be defined as the ratio between the actual *COP* and the *COP* of an ideal and totally reversible system operating within the same temperature limits in the hot and cold environments — the Carnot *COP*. The Carnot *COP* and the η_{2nd} are presented in Eq. (2.13) and Eq. (2.14):

$$COP_{Carnot} = \frac{T_C}{T_H - T_C} \tag{2.13}$$

$$\eta_{2nd} = \frac{COP}{COP_{Carnot}} \tag{2.14}$$

It is also important when comparing different technologies to respect the same ideal cycle baseline, which can be achieved by writing the (overall) second-law efficiency as the product of the internal and external efficiencies ($\eta_{2nd} = \eta_{2nd,i}\eta_{2nd,e}$). While the former accounts for fluid friction and thermal gradients in the cycle components, the latter is related to the transfer of heat with a finite temperature difference between the cycle and the hot and cold

reservoirs. Such an analysis helps to elucidate the processes that contribute the most to lowering the overall efficiency in each technology (HERMES; BARBOSA, 2012).

Figure 11 presents the thermodynamic representation of a general cooling system. If assumed that the refrigerator is ideal, internally and externally, the coefficient of performance depends only on the temperatures of the internal and external environments — T_C and T_H, and is equal to the Carnot *COP* presented in Eq. (2.13). If assumed that the cooling device operates ideally between the cold and hot ends — T_{CE} and T_{HE}, the *COP* considering thermal losses only due to the external irreversibilities can be calculated as follows in Eq. (2.15):

$$COP_{ii} = \frac{T_{CE}}{T_{HE} - T_{CE}} \tag{2.15}$$

where the ii index stands for internally ideal. The internally ideal *COP* is the maximum coefficient of performance possible to be achieved by the refrigerator when operating with real heat exchangers.

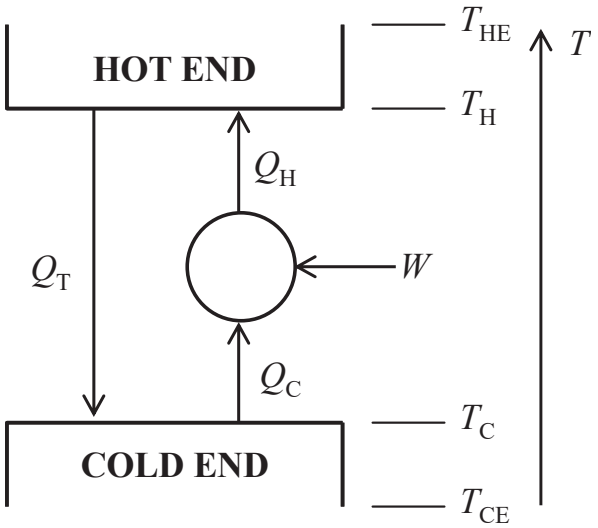

Figure 11 – Thermodynamic representation of a cooling system. Adapted from Hermes & Barbosa (2012).

The second-law efficiency associated with the internal irreversibilities is calculated by comparing the *COP* of the real refrigeration system with that obtained assuming an ideal refrigerator with real heat exchangers, as follows in Eq. (2.16).

$$\eta_{2nd,i} = \frac{COP}{COP_{ii}} \tag{2.16}$$

Similarly, the second-law efficiency associated with the external irreversibilities is calculating by comparing the *COP* obtained assuming an ideal refrigerator with real heat exchangers with that of an ideal and fully reversible refrigerator operating within the same temperature limits, as presented in Eq. (2.17).

$$\eta_{2nd,e} = \frac{COP_{ii}}{COP_{Carnot}} \tag{2.17}$$

3 Experimental analysis

This chapter presents the experimental methods adopted to characterize both vapor compression and magnetic cooling technologies, being divided into two sections. The first section describes the commercial product and its features, as well as the characterization of the conventional wine cooler according to standardized tests for household appliances. The second section describes the design phase of the magnetic wine cooler prototype for each subsystem, presenting the final apparatus assessment and features and the experimental test procedure applied in the characterization phase. In addition, both sections present the thermodynamic analysis for the respective cooling technology in focus.

3.1 Conventional wine cooler characterization

As mentioned in Ch. 1, one of the main goals of this work is to compare the conventional (vapor compression) and magnetic cooling technologies on the same basis, i.e., operating the same wine cooler cabinet, in order to determine the viability of the latter for this specific refrigeration application.

The performance baseline for comparing the two technologies was defined based on experimental characterization tests performed in a commercially available wine cooler. The characterization tests comprised an evaluation of the thermodynamic performance of individual components and of the system as a whole, including tests such as pull-down time, annual energy consumption and heat leakage. A complete description of the tests performed in the vapor compression system are presented in the work of Dutra (2018).

3.1.1 Product description

The baseline product is a commercially available wine cooler, the Brastemp *Gourmand Dual Zone* BZB31AEBNA, marketed by Whirlpool S.A.. Figure 12 presents a picture of the product. The wine cooler insulated cabinet is divided into two compartments in which the temperature can be set individually between 8 and 18ºC by its onboard control system, according to the wine type. The product stores up to 31 bottles, 10 in the upper compartment and 21 in the lower compartment. The main features of the wine cooler are presented in Tab. 1.

The refrigeration system of the wine cooler is charged with 38 g of R-134a and powered by a reciprocating, fixed speed compressor (WANBAO - ASF51X). The condenser is a wire-on-tube piece with 10 tube passes and 96 wires. Two roll-bond evaporators, one for the upper and another for the lower compartment, are connected to two distinct capillary tubes. The flow rate through each evaporator is controlled by a solenoid valve according to the temperature set point of each compartment. Two thermostats provide the input for the temperature control system, which employs an on-off control strategy. Figure 13 presents a

Figure 12 – Wine cooler Brastemp *Gourmand Dual Zone* BZB31AEBNA.

Table 1 – Main characteristics of the conventional wine cooler (DUTRA, 2018).

Characteristic	Values
Width [mm]	500
Height [mm]	970
Depth [mm]	595
Temperature range [°C]	8 to 18
Climate class	N
Mass [kg]	43
Capacity	31 bottles
Insulation	C-pentane

schematic diagram of the system.

3.1.2 *Cabinet instrumentation*

The instrumentation of the cabinet was installed according to the IEC 62552 (2015) standard for household refrigerating appliances. Figure 14 presents the positions of thermocouples assessing the air temperature in the cabinet. The temperature of each compartment was determined by the average of the measurements of two thermocouples in the upper compartment and three thermocouples in the lower compartment. The ambient temperature was determined by the average of three thermocouples placed at a distance of 30 cm from the cabinet external walls (left and right) and from the glass door. These T-type thermocouples, all with an uncertainty of ±0.2 K from manufacturer data, were assembled with a hot junction involved in a cylindrical copper block of 15 mm of height and width, in order to increase the thermal capacity and reduce abrupt temperature variations.

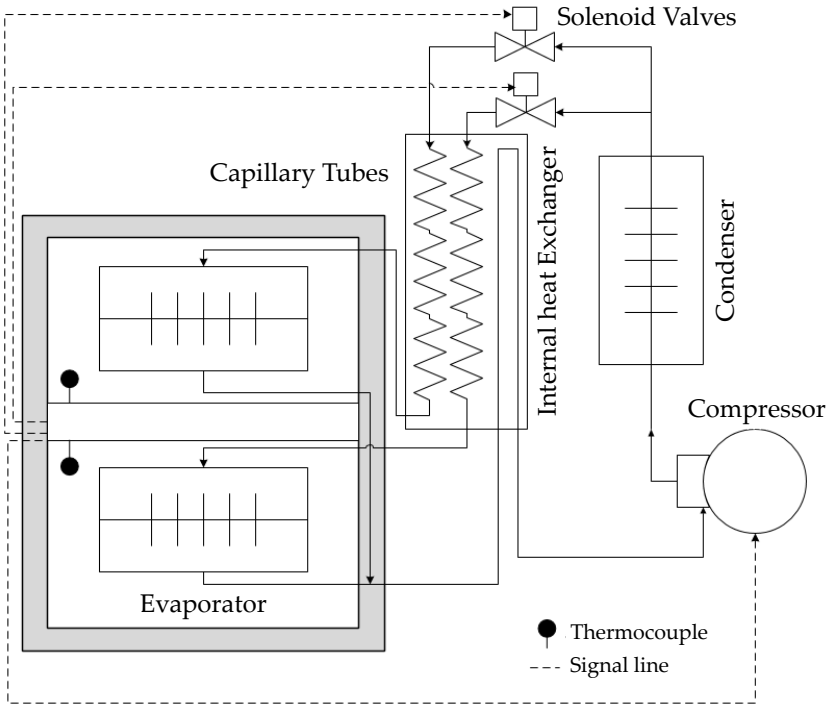

Figure 13 – Conventional wine cooler schematic diagram (DUTRA, 2018)

.

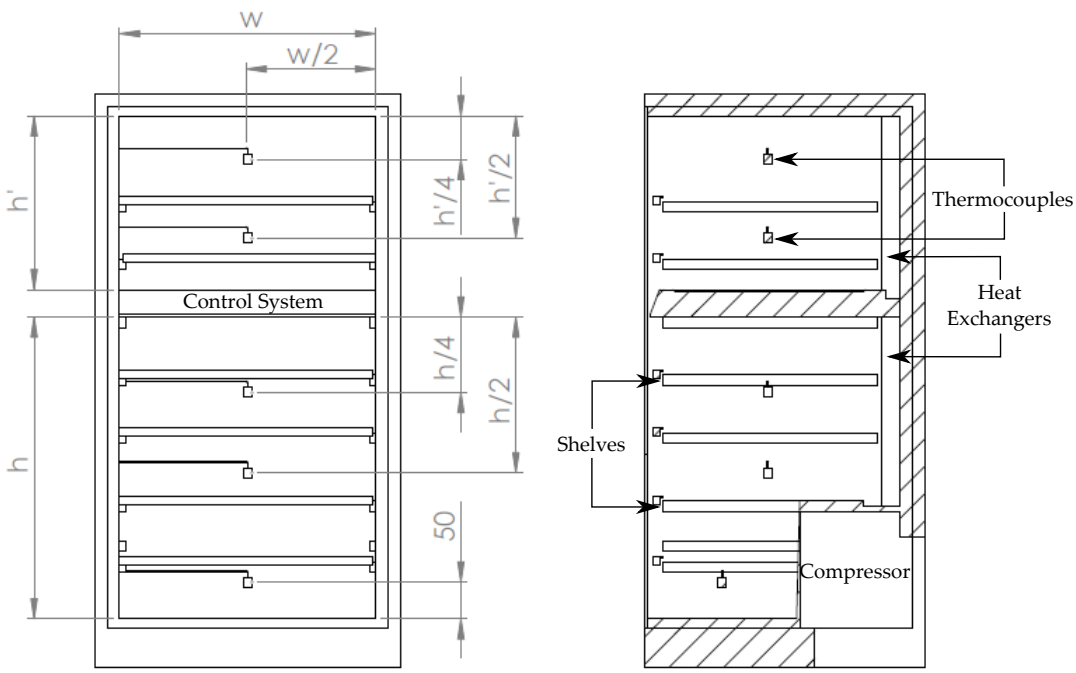

Figure 14 – Frontal and lateral view of the instrumentation of the cabinet for the characterization tests of the conventional system.

Additional thermocouples were placed at the inlets and outlets of the condenser and of the two evaporators (one in the upper and the other in the lower compartment). The hot junctions of the thermocouples were attached to the surfaces of those components, to avoid changing the original characteristics of the product. The thermocouples were also T-type,

with an uncertainty of ±0.2 K from manufacturer data, and were glued on in the surfaces with metallic tape, to avoid radiation influence over the measurements. A Kapton™ tape was placed between the surface of the components and the thermocouples, so as to provide electrical insulation and avoid errors in the measurements that could be caused by possible electrostatic charges. Additionally, a thermal grease was used to improve the heat conduction between the surface of the components and the thermocouples, thus improving the response and accuracy of the measurements.

3.1.3 Test chamber

The characterization tests were performed inside a climate-controlled test chamber, built in agreement with the ISO 15502 (2005) standard, with air temperature and relative humidity control. The temperature can be controlled between -20 and 60ºC (±0.5ºC) and the relative humidity between 40 and 95% (±1%), with air velocities lower than 0.25 m/s (ESPÍNDOLA, 2017). The chamber is controlled by a vapor compression refrigeration system, an arrangement of PID-driven electrical resistances and a humidifier. Figure 15 shows a schematic representation and distribution of the components inside the chamber.

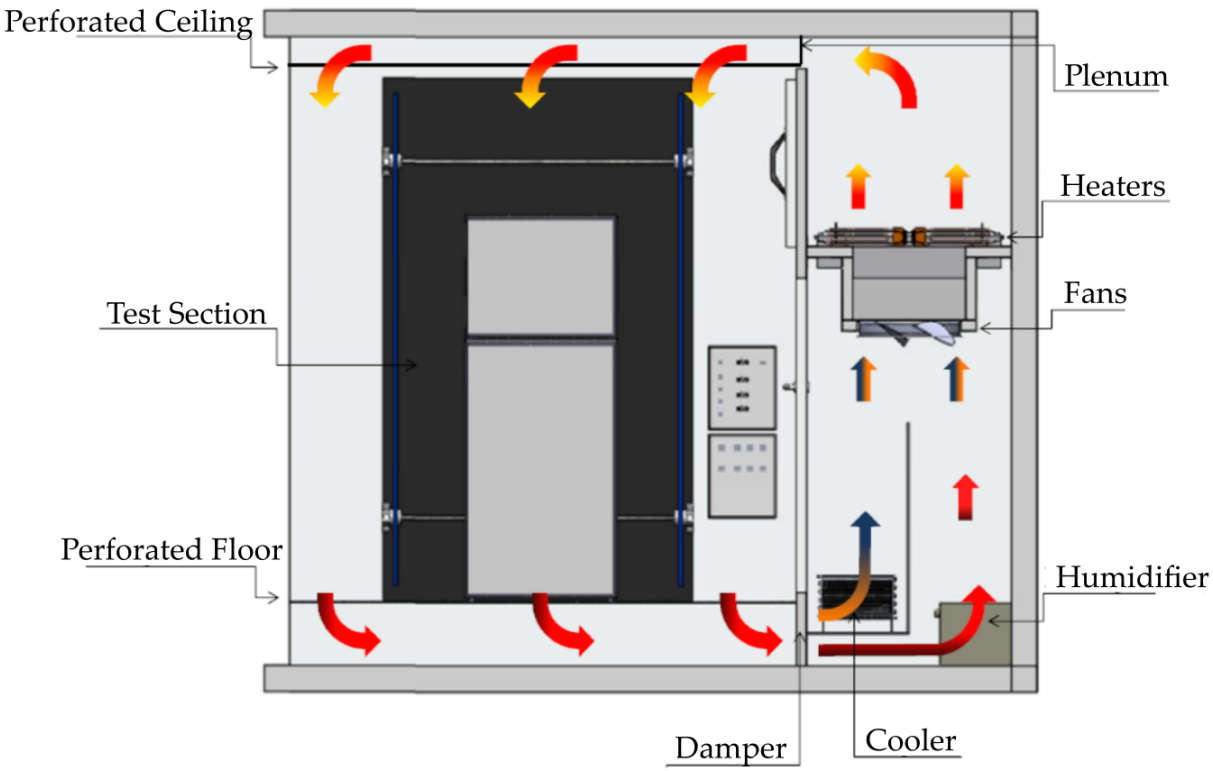

Figure 15 – Instrumentation of the cabinet for the characterization tests of the conventional system. Adapted from Thiessen (2015).

The air temperature is controlled by the refrigeration system and the electrical resistances, being monitored by four thermocouples placed at the top of the chamber, below the perforated ceiling. The refrigeration system and the fans operate continuously, while a PID control activates the resistance power dissipation. The air distribution is controlled by the fans and the damper. The humidity is controlled by the humidifier, consisting in a water tray

with a submerged electrical resistance, with a second PID control acting in the resistance power dissipation inside the tray to ensure the set relative humidity.

The voltage and the electrical current are measured with a power transducer (YOKOGAWA - WT230) and other data such as temperature values are acquired using a data acquisition system (AGILENT - HP34980). The monitoring and recording of the data are performed in LabView.

3.1.4 Temperature Pull Down Test

The pull down test consists of a temporal evaluation of the pressures, temperatures and power consumption of the refrigeration system (HERMES, 2000) between the time when the compressor is switched on and the time when steady state is reached, providing a characterization of the system transient response and cooling capacity. In the scope of this thesis, the pressure pull down was not evaluated, and the test was called as temperature pull down.

Prior to the test, the wine cooler is positioned inside the climate-controlled test chamber and, with compressor switched off, the cabinet door is kept open to guarantee an initial condition of thermal equilibrium between the inside of the cabinet and the controlled ambient. Once equilibrium is reached, the door is closed and the compressor and other equipment are switched on. The test is finished when the system achieves steady state. During the test, both ambient and cabinet temperatures are recorded, as well as the power consumption (compressor and other components).

The latest international standard for household appliances, IEC 62552 (2015), does not specify the ambient temperature for wine cooling appliances. As regards domestic refrigerators, the standard recommends following the climate classification of the product. Thus, for the N-class product (subtropical region) the test was carried out at an ambient temperature of 25.0±0.5ºC. As regards the determination of the final internal temperature of the cabinet, the test was carried out in two different limits, one with both thermostats set to the minimum operation temperature, 8ºC, and another with both thermostats at the temperature recommended by IEC 62552 (2015) for wine coolers, 12ºC.

3.1.5 Energy Consumption Test

The energy consumption is the main quantitative parameter associated with the thermodynamic performance of a refrigerator (THIESSEN, 2015). According to Hermes, Melo & Knabben (2013), ISO 8561 (1995) used to be the international standard for testing frost-free refrigerators until 2005, when it was replaced by ISO 15502 (2005). Currently, both standards have been merged into IEC 62552 (2015). In general, the standards follow a similar test procedure. Firstly, the refrigerator should be tested according to its climate classification: for N-class products (subtropical regions) the test is carried out at an ambient temperature of 25.0±0.5ºC and for T-class (tropical regions) the ambient temperature is 32.0±0.5ºC. The internal cabinet temperature of the product is set using its onboard control system. Also, the

refrigerator power consumption must be monitored during a period of 24 hours comprising an integer number of on-off compressor cycles and at least two defrosting cycles. The energy consumption is then calculated by the integration of the power consumption of the product during the entire test period. As it may be difficult to maintain the test temperature inside the cabinet exactly at the reference, two tests are carried out, one above (EC^+) and another below (EC^-) the reference temperature (T_R). The energy consumption at the reference temperature (EC_R) is then calculated through a linear interpolation using both test runs, as represented in Fig. 16.

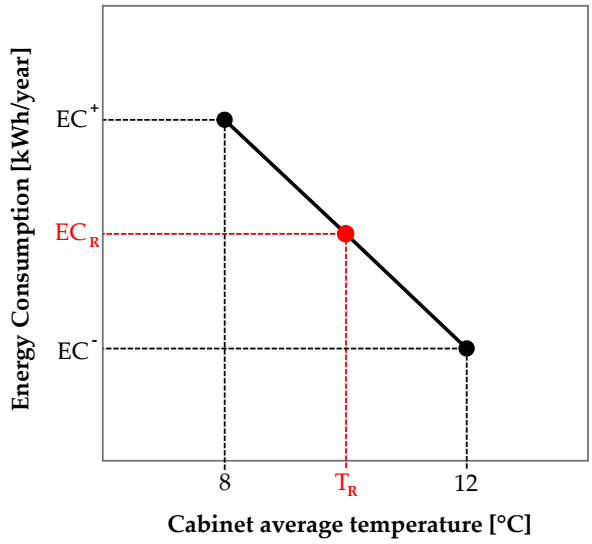

Figure 16 – Energy consumption calculation through linear interpolation. Adapted from Thiessen (2015).

Aiming to overcome possible disadvantages associated with the standardized energy consumption test, Thiessen (2015) proposed an alternative test method that provides reliable results with an easier approach and shorter testing times. The test procedure is monitored during a period of 5 hours comprising an integer number of on-off compressor cycles. Defrosting cycles are not considered. Also, the test is performed after the product reaches the periodic steady state. As the results are aimed at comparing conventional and magnetic refrigerating systems — and not at characterizing the final product for approval, this method was adopted for the energy consumption data.

Concerning wine coolers, IEC 62552 (2015) establishes that the energy consumption test must be carried out with an internal temperature of, at most, 12°C. In this case, the tests were carried out for the standard indicated temperature and the minimum temperature allowed by the onboard control, 8°C, so as to establish an interval for possible interpolation to be used in the comparison with the prototype test results.

3.1.6 *Reverse Heat Leakage Test*

The energy consumption of a refrigeration system is mostly defined by the thermal load due to heat transfer through its cabinet walls (GONÇALVES et al., 2000). Thus, the quality of the thermal insulation is key to guaranteeing the efficiency of the cooling system. On account

of sizing the quality of the insulation, Gonçalves et al. (2000) proposed a test methodology to evaluate the overall thermal conductance in an indirect approach, the reverse heat leakage (RHL) test.

The RHL consists of heating the interior of the cabinet to temperatures higher than those of the surroundings, creating a temperature difference with respect to the external ambient and, consequently, a heat flux in that direction. During the test, the cooling system remains switched off. The compartments are heated by PID-driven electrical resistances, positioned in such a way to minimize the thermal stratification. Once the steady state is reached, the temperatures inside the compartment and the surroundings are recorded together with the power consumption of the electrical resistances. Applying these data in an energy balance of a control volume with boundaries such as presented in Fig. 17, the resulting equation is given by Eq. (3.1):

$$UA_{\text{up}}(\overline{T}_{\text{up}} - \overline{T}_{\text{sur}}) + UA_{\text{low}}(\overline{T}_{\text{low}} - \overline{T}_{\text{sur}}) = \dot{W}_{\text{up}} + \dot{W}_{\text{low}} \tag{3.1}$$

where UA_{up} and UA_{low} are the overall thermal conductances of the upper and lower compartments, $\dot{W}_{\text{up}}$ and $\dot{W}_{\text{low}}$ are the average power dissipation rates of the electrical resistances in the upper and lower compartments and $\overline{T}_{\text{up}}$, $\overline{T}_{\text{low}}$ and $\overline{T}_{\text{sur}}$ are the average temperatures for the upper and lower compartment as well as the surroundings.

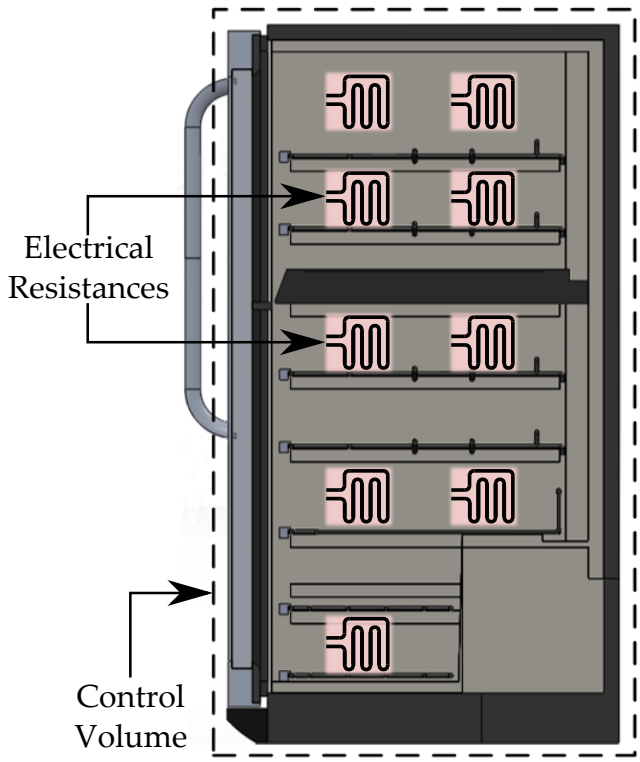

Figure 17 – Schematic representation of the control volume for the energy balance during the RHL tests.

Except for the overall thermal conductances, the remaining parameters in Eq. (3.1) are directly measured. As there are two unknowns for one equation, at least two linearly independent tests are required in order to determine UA_{up} and UA_{low} by the least-squares

method (ESPÍNDOLA, 2017). Aiming to decrease the uncertainty of the results, four linearly independent tests were proposed, as presented in Tab. 2.

Table 2 – Experimental parameters of the RHL tests.

Test	1	2	3	4
Temperature of the upper compartment [°C]	50	60	50	60
Temperature of the lower compartment [°C]	35	40	50	50

3.1.7 Conventional Wine Cooler Thermodynamic Analysis

The thermodynamic performance of the conventional wine cooler is evaluated in terms of the coefficient of performance (*COP*), the overall second-law efficiency (η_{2nd}) and the internal and external portions ($\eta_{2nd,i}$ and $\eta_{2nd,e}$). The *COP* is the ratio between the cooling capacity, $\dot{Q}_C$, and the average electric power consumed by the product, $\dot{W}_{Total}$, as presented in Eq. (3.2):

$$COP = \frac{\dot{Q}_C}{\dot{W}_{Total}} \tag{3.2}$$

The cooling capacity at periodic steady state is equal to the thermal load imposed by the surroundings on the refrigerated compartments, given by Eq. (3.3).

$$\dot{Q}_C = UA_{up}(\overline{T}_{amb} - \overline{T}_{up}) + UA_{low}(\overline{T}_{amb} - \overline{T}_{low}) \tag{3.3}$$

The total power is calculated with the average of the voltage and electrical product in periodic steady state. The overall second-law efficiency (Eq. (2.14)), η_{2nd}, and the internal and external portions, $\eta_{2nd,i}$ and $\eta_{2nd,e}$, are calculated in terms of the actual *COP* (Eq. (3.2)), the Carnot *COP* and the *COP* of an internally ideal system. The Carnot *COP* is given by:

$$COP_{Carnot} = \frac{\overline{T}_{cab}}{\overline{T}_{amb} - \overline{T}_{cab}} \tag{3.4}$$

where $\overline{T}_{cab}$ is the average temperature of the cabinet. The internally ideal *COP* is given by:

$$COP_{ii} = \frac{\overline{T}_{evap,in}}{\overline{T}_{cond,in} - \overline{T}_{evap,in}} \tag{3.5}$$

where $T_{evap,in}$ and $T_{cond,in}$ are the averages temperatures in the evaporator and condenser inlets, respectively. Although the evaporator and condenser inlets temperatures refer to the temperatures of the refrigerant, they were assumed equal to the surface temperatures measured at the inlet of each component. The overall, internal and external second-law efficiencies are calculated as presented in Sec. 2.3.

3.2 Magnetic wine cooler development

The magnetic wine cooler prototype was designed and assembled at the Federal University of Santa Catarina (UFSC) by the PoloMag group in a two-year research project, be-

ing divided mainly into 3 study fronts: AMR/Magnet (FORTKAMP; LOZANO; BARBOSA, 2017; FORTKAMP et al., 2018; BEZ et al., 2018; LANG, 2018; HINKEL, 2018; FORTKAMP, 2019; FORTKAMP et al., 2020; BEZ et al., 2020), Hydraulics/Control (DUTRA et al., 2017; HOFFMANN et al., 2017; CARDOSO, 2018; SANTOS, 2018; NAKASHIMA et al., 2018a; HOFFMANN, 2020), Cabinet/Heat Exchangers (HEx) (PEIXER et al., 2018; DUTRA, 2018; CALOMENO, 2018; PEIXER et al., 2020). Further steps included the Integrated Design subgroup, responsible for the integration and overall optimization of the prototype.

The design phase of the magnetic wine cooler was carried out with an extensive list of trade-off relationship between subsystems, aiming not at the optimization of single components, but of the system as a whole. The exchange of ideas between the subgroups during the design phase was performed according to the product development model proposed by Oliveira (2017), based on the Lean Product Design and Set Based Concurrent Engineering methodologies. Each subsystem and their main characteristics are described in the sections below. A more detailed description of the PoloMag project and the magnetic wine cooler subsystems can be found in the work of Nakashima et al. (2020). A short video illustrating its main features is available at YouTube[1].

3.2.1 AMR/Magnet System

The AMR/magnet assembly is arguably the most important subsystem for it is the core of the magnetic refrigeration system. Standalone selection and optimization of the regenerator and/or magnetic circuit could potentially lead to lower than expected system performance. Thus, Fortkamp (2019) proposed an integrated design of geometric features of an AMR/magnet assembly to achieve the required cooling capacity and temperature span. Fig. 18 shows a quadrant cross section of the magnetic circuit, where the different regions are: (i) the shaft[2], from 0 to R_i, (ii) the stator, from R_i to R_o, (iii) the gap where the regenerator beds are placed, from R_o to R_g, (iv) the magnet cylinder, from R_g to R_s and (v) the external shell, from R_s to R_c.

The magnet design was based on the Halbach cylinder array configuration, with segments of Ne-Fe-B alloys as hard magnetic material, interlayered by segments of a magnetic steel alloy. The AMR beds were designed as rectangular prisms, in a set of two concentric stainless steel cylinders connected by 8 equidistant divisions, thus forming 8 regenerators. The number of regenerators were selected aiming at reducing the number of valves and simplifying the hydraulic and control system (more details in Sec. 3.2.2).

The AMR porous matrix material and length fraction selection followed the propositions of Teyber et al. (2016) and Cararo (2016), who performed experimental and numerical optimization of AMRs using Gd-Y alloys, respectively. The regenerator hot and cold inlet temperatures have been defined based on the works of Peixer et al. (2018), Dutra (2018), Calomeno (2018) and Peixer et al. (2020), who evaluated the effects of the heat exchanger design on the AMR performance (more details in Sec. 3.2.3). Thus, the regenerators were filled

[1] https://www.youtube.com/watch?v=y56ApAvZDoA
[2] Stationary shaft, for structural purposes.

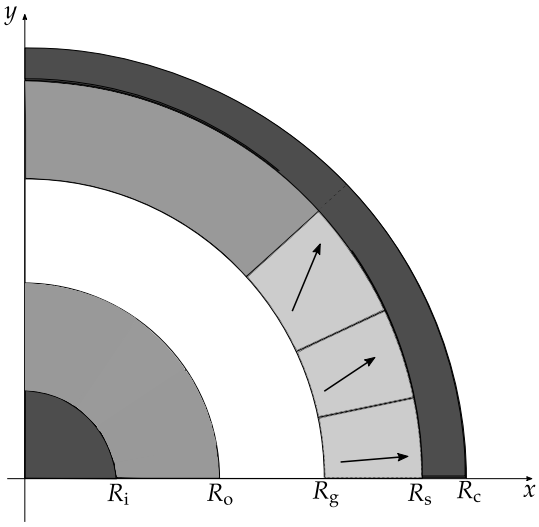

Figure 18 – Quadrant of the cross section of the magnetic circuit. Adapted from Fortkamp (2019).

with Gd and Gd-Y alloys, each layer with its own T_{Curie}, as follows: 74% (length fraction) of Gd (T_{Curie} = 290 K), 17% of $Gd_{97.34}Y_{2.66}$ (T_{Curie} = 283 K) and 9% of $Gd_{95.98}Y_{4.02}$ (T_{Curie} = 277 K). The behavior of the properties of the magnetocaloric materials as a function of temperature and magnetic field are presented in Fig. 19.

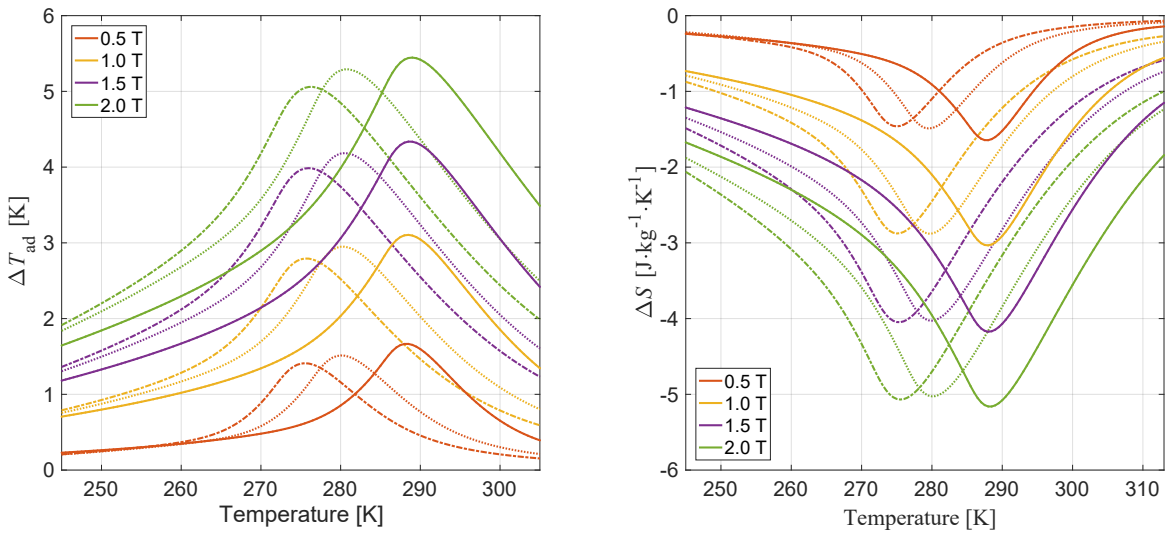

(a) (b)

Figure 19 – Properties of the Gd and Gd-Y alloys used in this assessment. (a) Adiabatic temperature variation, (b) isothermal specific entropy variation. Adapted from Bez et al. (2020).

The external shell is composed of a magnetic steel alloy, acting as flux concentrator. The stator is composed of laminated electrical steel E145, guiding the field lines toward the regenerator. The structure is supported by a stainless steel shaft. The main components of the AMR/magnet assembly are presented in Fig. 20.

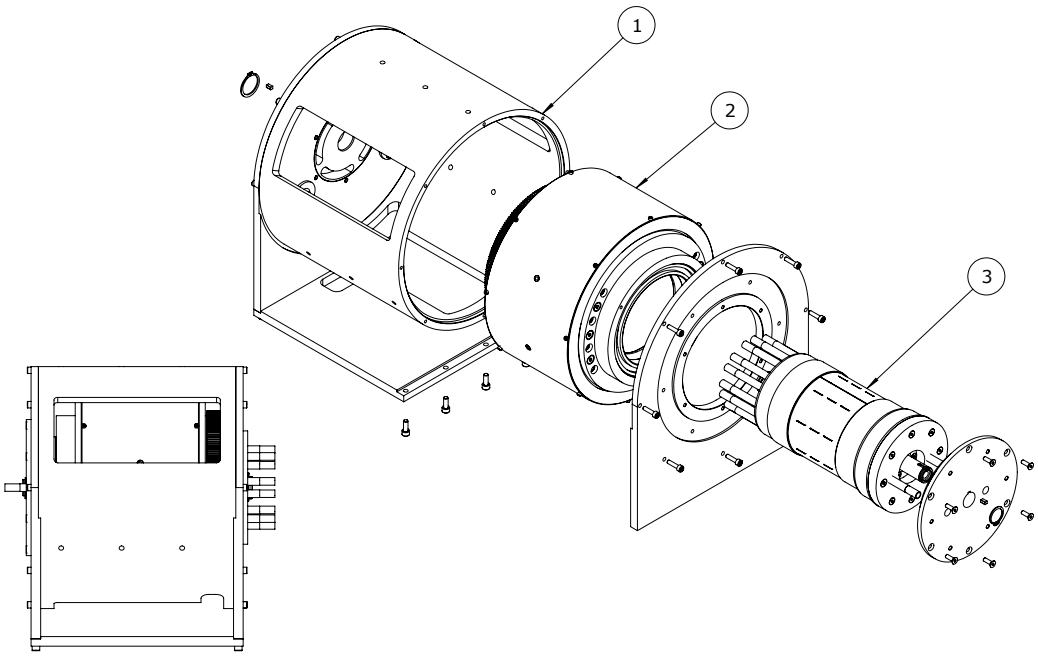

Figure 20 – Exploded view of the first prototype. (1) External housing (for safety purposes); (2) External magnet cylinder; (3) AMR/stator assembly.

3.2.2 *Hydraulic/Control System*

The hydraulic/control system is responsible for the execution of the AMR cycle, comprising pumping the fluid to the appropriate regenerator bed at a specific flow rate and in sync with the magnetic field waveform generated by the rotation of the magnet cylinder. The great effort put in designing and optimizing the AMR/magnet system would be wasted if the AMR cycle was not properly executed (NAKASHIMA et al., 2020). Thus, previous devices developed at POLO-UFSC (TREVIZOLI et al., 2016; LOZANO et al., 2016; HOFFMANN et al., 2017; DUTRA et al., 2017; NAKASHIMA et al., 2018b; CARDOSO, 2018; SANTOS, 2018) studied the influence of the valves as key design elements to the definition of the final power consumption of the system. A compilation of these works was presented by Nakashima et al. (2018b) and is shown in Fig. 21.

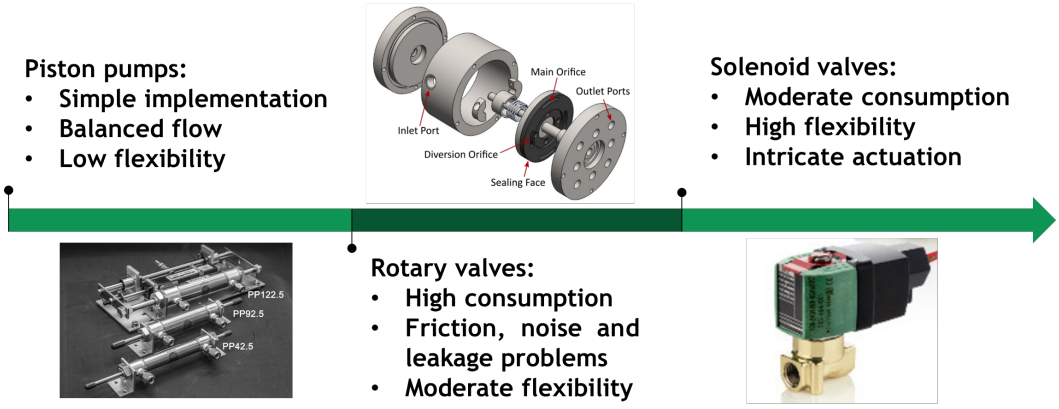

Figure 21 – Progress of the hydraulic devices developed at POLO-UFSC (NAKASHIMA et al., 2018b).

Following these works and taking into consideration a trade-off analysis between

the cost and power consumption of the valves, as well as their commercial availability, a 2/2 solenoid valve was selected, in a scheme proposed by Cardoso (2018), to manage the execution of the AMR cycle. The scheme consists of two valves per regenerator pair for a two-pole magnetic circuit, controlling the inlet and outlet on one side of the beds, while the flow direction is controlled by check valves. The assembly logic of the 2/2 valves with the regenerators is further presented in Fig 27 of Sec. 3.2.5. Although the 2/2 valve scheme is not the most efficient, it was selected so as to reduce the costs of the preliminary apparatus, leaving the power optimization as a future development for the final product device.

To assist on the flow control through the regenerators, manifolds and adapters were manufactured, as shown in Fig. 22. As the regenerator represents the border between the hot side and the cold side of the system, two types of manifolds were manufactured: the hot side manifold and the cold side manifold. The hot side manifold was designed for flexibility, by providing individual access to the inlet and outlet ports of each regenerator bed and thus enabling the implementation of different valving schemes. The cold side manifold was designed for simplicity, by combining the inlet and outlet ports of the AMR bed into two common ports for the heat exchanger connection.

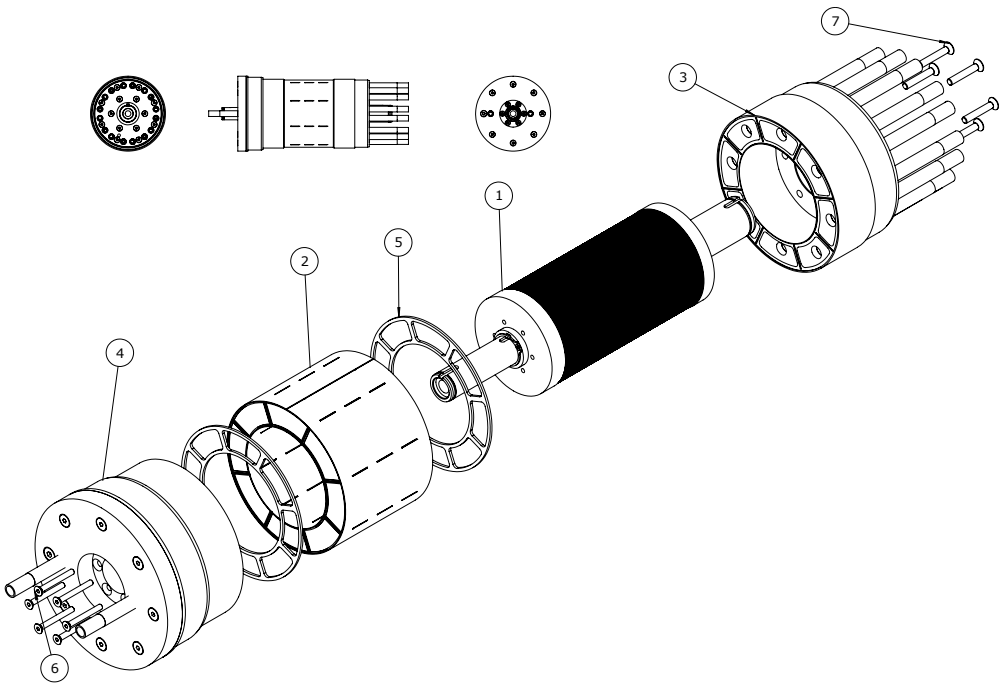

Figure 22 – Exploded view of the AMR, stator, manifolds and adapters assembly. (1) Stator and shaft; (2) regenerator casing; (3) hot side AMR adapter and manifold; (4) cold side AMR adapter and manifold; (5) gasket; (6) tubes; (7) screws.

The synchronization between flow and magnetic field is ensured by a control logic implemented in LabView, following the work of Hoffmann et al. (2017). A sequence of frames corresponding to a full AMR cycle is presented in Fig. 23. The first action of the control is to measure the magnetic field with a Hall effect sensor[3] (HES) to obtain the field waveform and the rotation angle of the magnet during its operation. Then, a set of triggers for the opening and closing of the valves are established, based on the rotation angle and the

[3] Transducer that responds with a variation of the voltage signal when submitted to a magnetic field.

blow fraction. The blow fraction is the ratio of the blow period in one regenerator and the cycle period. For this apparatus, the blow fraction was defined as 25%, meaning that each regenerator will be experiencing fluid flow in one direction in 25% of the full cycle period. In order to ensure constant fluid flow in the cold heat exchanger, the regenerator beds were divided into (A and B) groups and further divided in (1 and 2) pairs. Thus, at each instant of the cycle, one group will be supplied with fluid flow, with opposite directions in the 1 and 2 pairs, while the other group will experience magnetic field variation, either positive or negative. A sequence of four instants, (i) through (iv), corresponds to a full AMR cycle. As the angular speed of the magnet, ω_{m}, is half the speed of the cycle, ω_{cycle}, it also corresponds to a half magnet rotation.

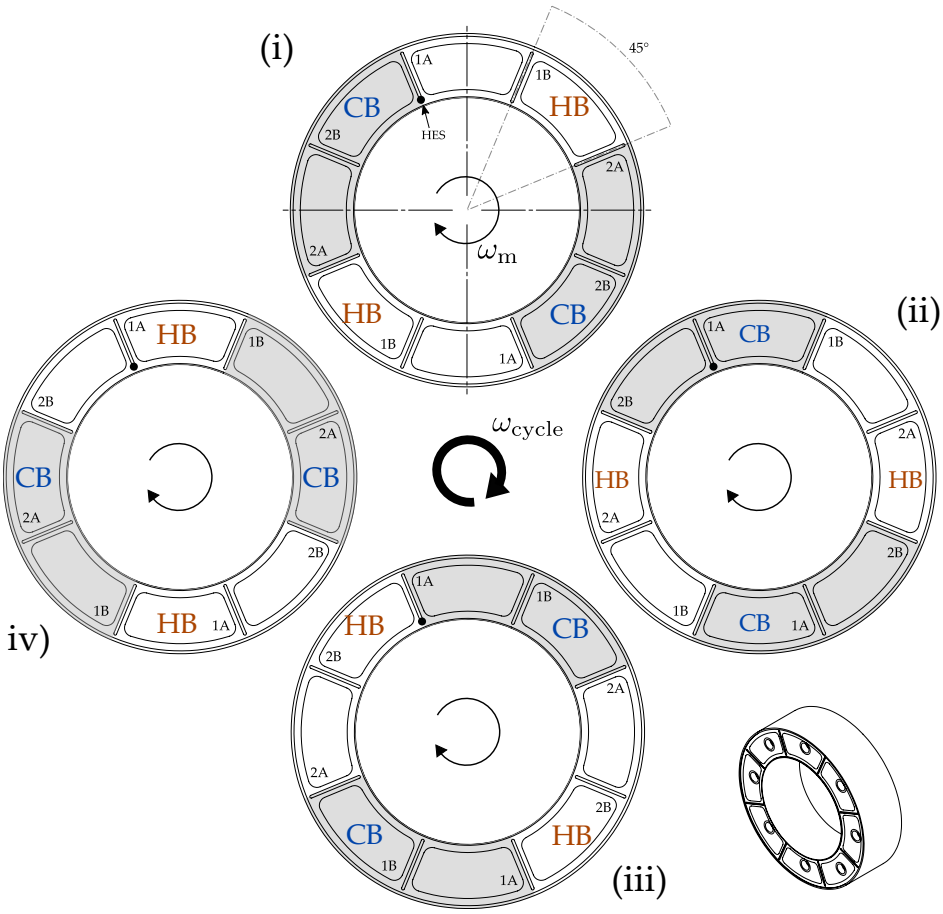

Figure 23 – Blow steps in the regenerator beds (represented by the AMR adapter) for half a magnet rotation (or a full AMR cycle). Regarding the regenerator 1A, instants (i) through (iv) represent the start of the magnetization, cold blow, demagnetization and hot blow, respectively. The grey area corresponds to the region where the magnetic field is superior to $B_{\mathrm{max}}/2$ (NAKASHIMA et al., 2020).

The first procedure of the control algorithm is to measure the magnetic field waveform for a given number of magnet periods. The control loop starts at instant (i) of Fig. 23, which represents the moment when the field measured in the HES reaches approximately $H_{\mathrm{high}}/2$ (gray region) and so the controller is triggered. After that, the controller waits a period equivalent to $(\pi/4)/\omega_{\mathrm{m}}$ ($\pi/4$ is the designed angular width of a regenerator) to execute step (ii) by opening the group A valves, allowing the cold and hot blows in pairs 1A and 1B,

respectively. Steps (iii) and (iv) are a repetition of (i) and (ii) for group B, allowing the cold and hot blows in pairs 2A and 2B, respectively. Once the four steps are completed, half a magnet rotation is accomplished. Thus, for each magnet rotation, two of the AMR cycles just described are performed.

3.2.3 Cabinet/Heat Exchangers System

For the present prototype, one is concerned with estimating the performance of a potential product and so thermal characteristics of heat exchangers and cabinet must be considered in the design phase. In this regard, Peixer et al. (2018), Dutra (2018) and Calomeno (2018) developed a detailed study of the influence of the HEx effectiveness on the performance of an AMR system. Figure 24 shows how the heat exchanger effectiveness contributes to increasing the temperature span that must be produced by the regenerator, $\Delta T_{\text{reg,out}}$, to maintain the desired system span, ΔT_{sys}.

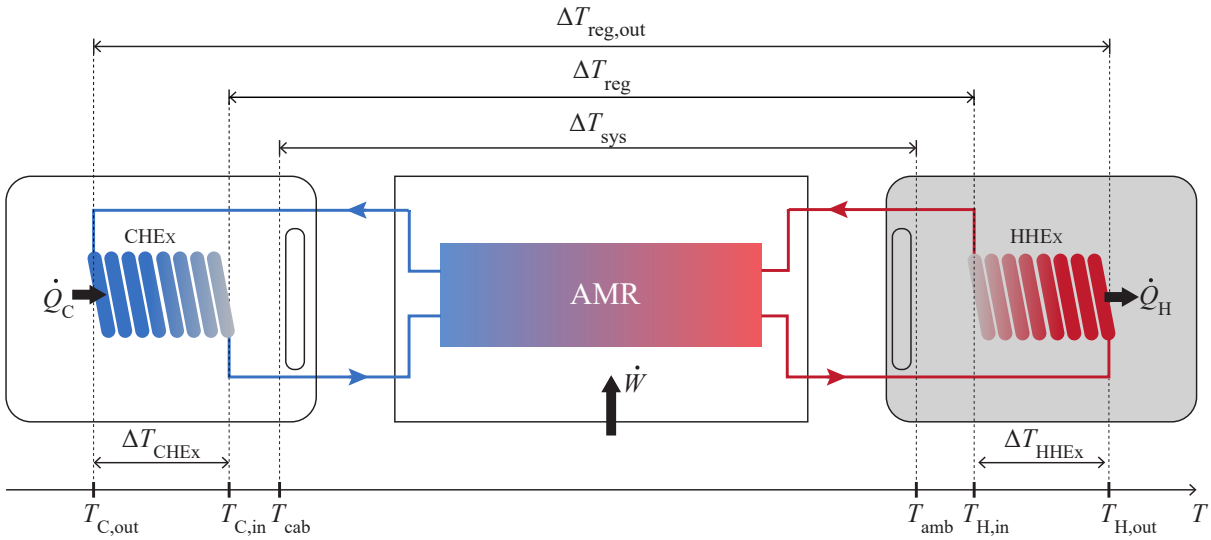

Figure 24 – Representation of the coupling between AMR, heat exchangers and cabinet. Adapted from Calomeno et al. (2016).

As the cooling capacity decreases with an increase in the AMR temperature span, sources of ineffectiveness in the heat exchanger negatively affect the regenerator performance. This behavior is presented in Fig. 25, where the cooling capacity and the regenerator temperature span are presented as a function of the effectiveness of the liquid water stream, given by the product of the effectiveness, ϵ_{HEX}, and the thermal capacity ratio, C^*, considering air as the other heat exchanger fluid.

To meet the cooling capacity requirement for the first prototype, axial fans and fin-tube compact heat exchangers were selected and tested in an apparatus simulating the AMR and coupled with the cabinet from the vapor compression wine cooler (PEIXER et al., 2020). For simplification purposes, the cabinet with originally two compartments was made into a single one through the removal of the onboard control system — which was also the physical barrier between the compartments. Other components from the vapor compression wine cooler, e.g., the compressor, expansion device and the original heat exchangers were

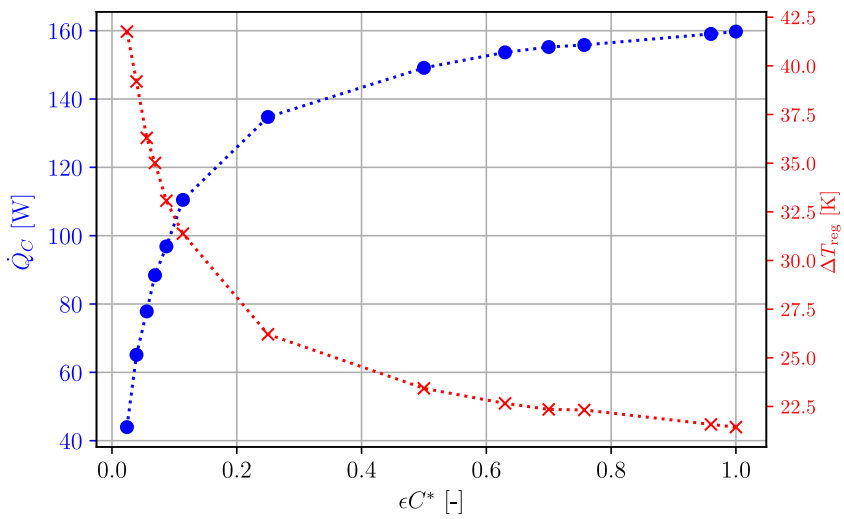

Figure 25 – Influence of the liquid stream effectiveness on the regenerator temperature span and cooling capacity (PEIXER et al., 2018).

removed from the product. This test apparatus was developed in the work of Dutra (2018), in which the main objective was to characterize different heat exchangers with the same fan inside the wine cooler cabinet and determine the fan-heat exchanger combination with the highest effectiveness to be used in the prototype.

The input of the tests was the inlet water temperature of the cold heat exchanger, controlled by a thermal bath. The outputs were the cabinet final temperature, the outlet water temperature of the cold heat exchanger and inlet and outlet air temperatures in the cold heat exchanger. The variable of the tests was the cold heat exchanger, with different number of rows (one or two) in the longitudinal direction and different fin density (from 8 to 12 fins per inch). The frontal area was kept fixed, with heights and widths of 152 mm and 110 mm, respectively. The results are presented in Fig. 26, which shows the system temperature span as a function of the liquid stream effectiveness. The selected heat exchanger was the 2 tube rows with 10 fins per inch, to be used in the cold side, and, because of availability, both 2 tube rows with 10 and 12 fins per inch to be used in the hot side in case more than one was needed.

3.2.4 Experimental Apparatus

The experimental apparatus is represented schematically in Fig. 27. The heat transfer fluid is a 90/10 vol.% mixture of deionized water and commercial anti-freeze (ethylene glycol with anti-corrosion additives). The hydraulic circuit is composed of a hot and a cold side, sharing an AMR/magnet set as border. The AMR/magnet set consists of the magnet, the magnet's rotating system, the active magnetic regenerators, the stator and the flow distributors (manifolds). The magnet is shaped as a cylinder and rotates through an arrangement of toothed pulleys and a timing belt attached to an electrical motor (SEW R17-DRE80S4). As mentioned previously in Sec. 3.2.1, the regenerator beds are filled with three layers of Gd and Gd-Y alloys separated with a wire mesh attached to a frame with the same shape as the

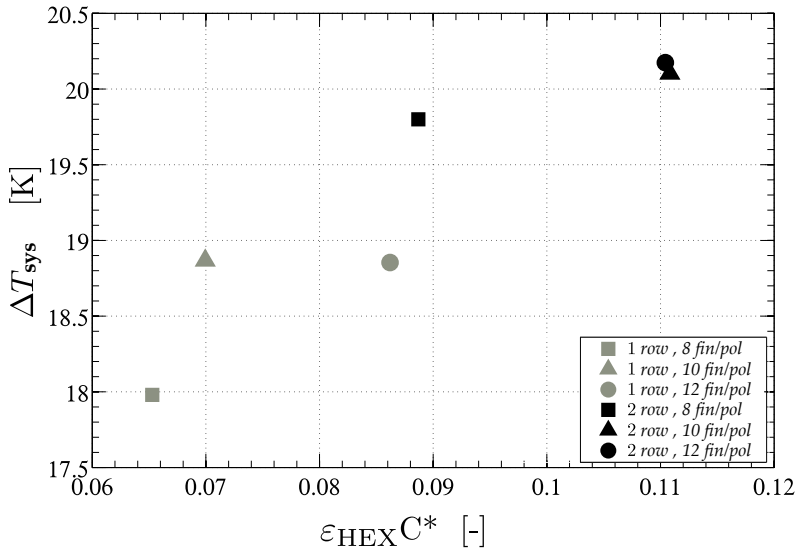

Figure 26 – System temperature span as a function of the liquid water effectiveness, ϵC^*, for six geometries of heat exchangers.

regenerators. The layers and divisions in the regenerator are shown in Fig. 28.

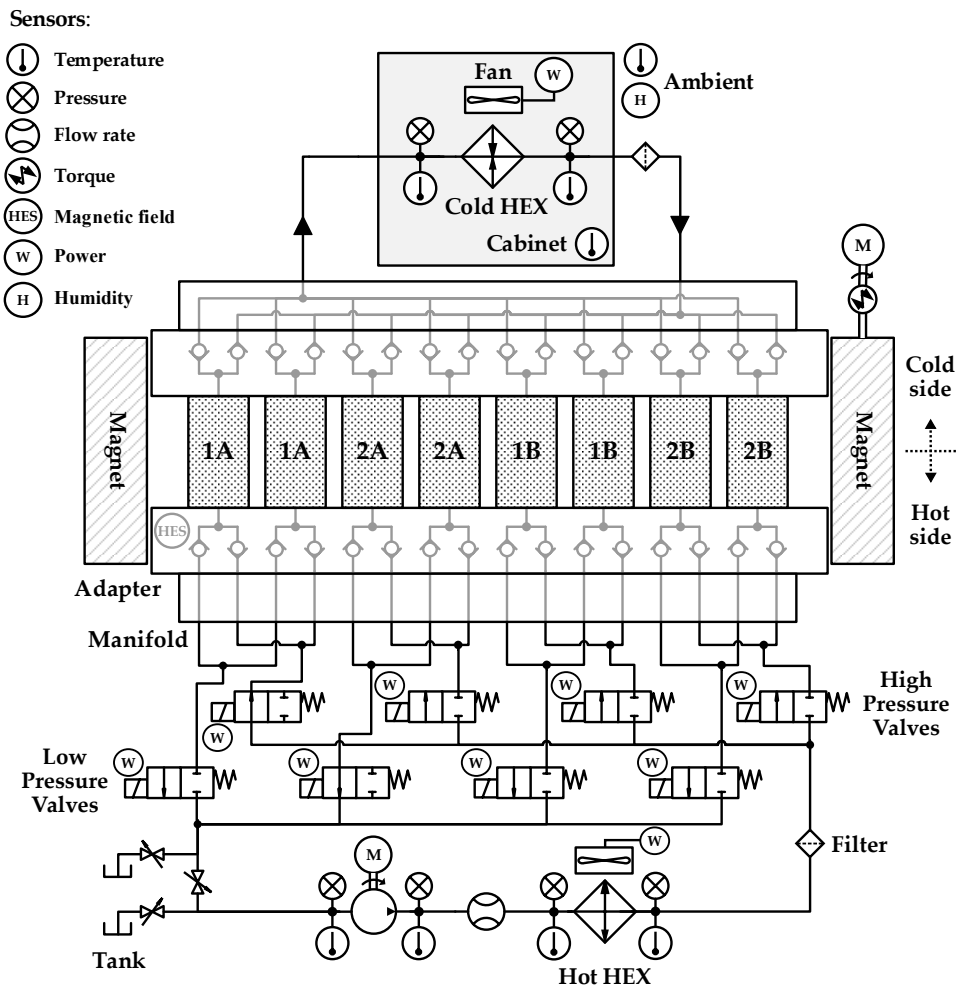

Figure 27 – Schematic diagram of the magnetic wine cooler apparatus.

The hot side comprises the pumping system, three fan-supplied finned tube heat exchangers (HHEx) mounted in parallel and a set of 8 solenoid valves. The pumping system is

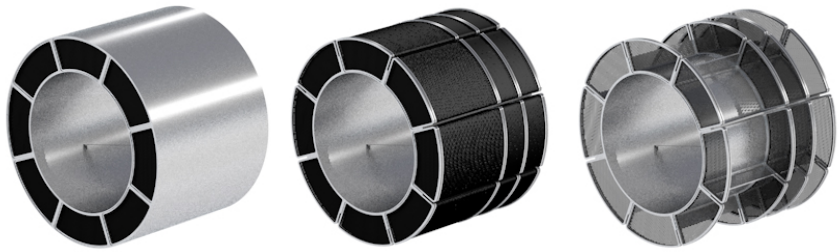

Figure 28 – Schematic view of the regenerators and the internal subdivisions of the layers.

composed of a gear pump (Micropump GL-H25) and an electrical motor (WEG W22 Plus), responsible for providing the desired flow rate according to the set motor speed. The HHEx (vide Annex A) and the hot fans (Ong HuaHA1225M12S-Z and Emb-PapstTYP 4412 FGM) are responsible for the interaction between the heat transfer fluid with the ambient room, associated in parallel to increase the heat rejection rate to the ambient without raising the internal fluid side pressure drop. It was noticed that using three heat exchangers — which increased the surface area on the hot side, helped to remove the additional heat dissipated by the pumping system and guaranteed a temperature near 25ºC at the regenerator entrance, which is essential to achieve a higher magnetocaloric effect along the regenerator layers. The solenoid valves (ASCO Next Generation 8262R232) are responsible for allowing the fluid to flow into the appropriate regenerator pairs according to the magnet position.

The cold side comprises a fan-supplied finned tube heat exchanger (CHEx) and the wine cooler cabinet. The CHEx (Annex A) and the cold fan (Bi-sonic BP1202512H) are responsible for the interaction between the heat transfer fluid and the cold air inside the refrigerated cabinet. The experimental apparatus is presented in Fig. 29.

The cabinet is internally instrumented according to the IEC 62552 (2015) standard, as presented in Fig. 30, and externally instrumented with 3 thermocouples placed at 30 cm distance from the cabinet external walls (left and right) and from the glass door. The cabinet and ambient temperature are determined by the average of the thermocouples set in each respective environment. Other instrumentation includes measurements for the volumetric flow rate, torque, magnetic field, pressure and internal fluid temperatures. The volumetric flow rate is measured by a turbine type flow meter (Aalborg PWE04P-VLN-B2). The torque is measured by a torque transducer (HBM T22). The magnetic field is measured by a Hall sensor (Lake Shore HGT-1010). The air temperatures (cabinet and ambient) are measured by T-type wire thermocouples (Omega PR-T-24-SLE-ROHS) with a copper cylindrical mass of 15 mm of height and width in the (hot) junction, in order to increase the thermal inertia and reduce abrupt temperature variations. The water temperatures are measured by probe thermocouples (Omega TMQSS-062G-6). Both air and water thermocouples were calibrated with a reference probe (Testo 735-2 with Probe 0614 0235) and a thermal bath (Thermo Scientific™ SC150-A40) to decrease the measurement uncertainties. Lastly, the pressure is measured with absolute pressure transducers (Omega PX309), calibrated with a hydraulic dead-weight tester (DH-Budenberg 580). The sensors and their uncertainties are summarized in Tab. 3.

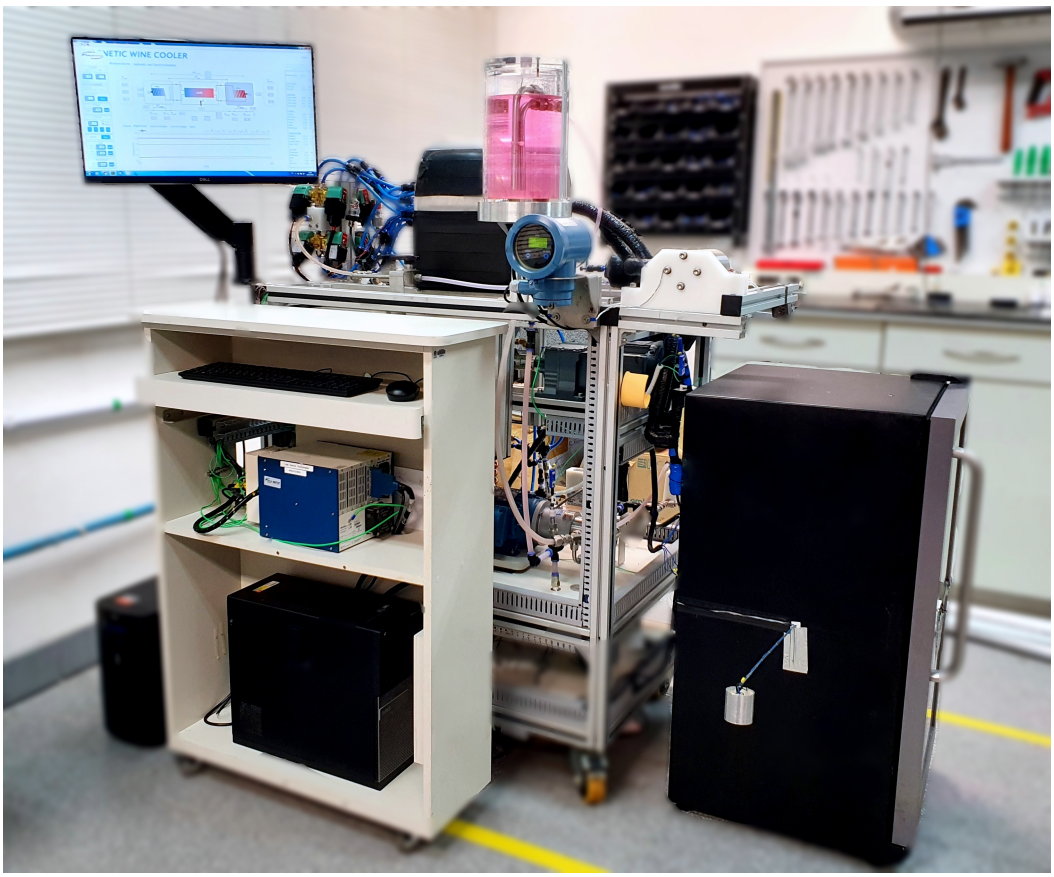

Figure 29 – Prototype assembly.

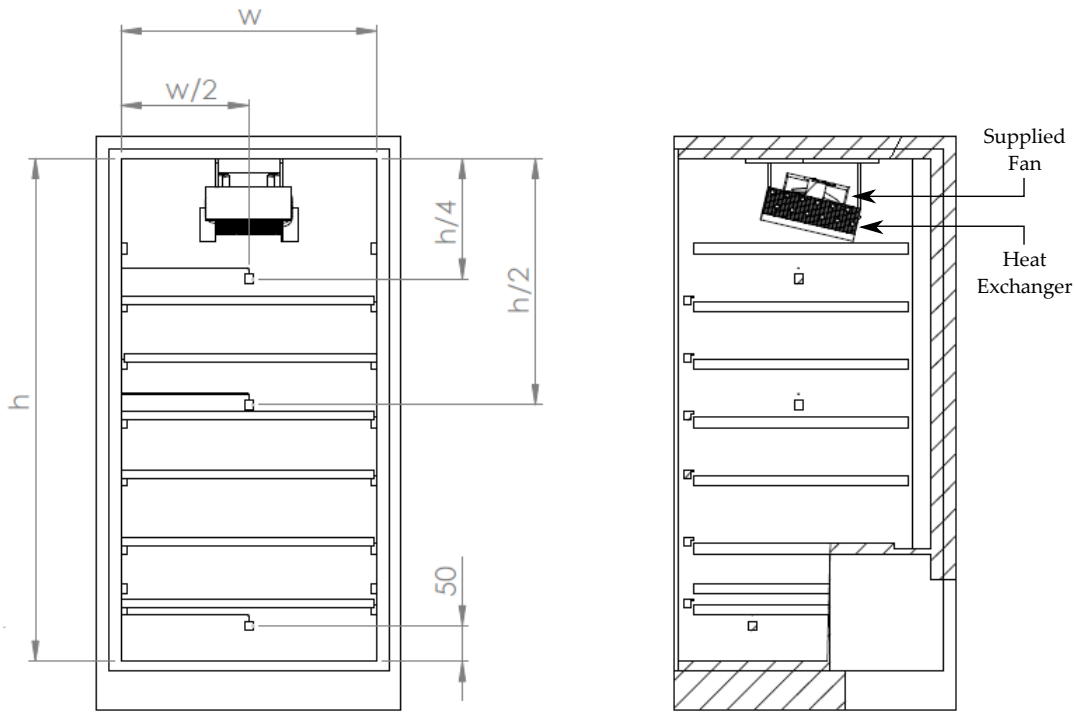

Figure 30 – Instrumentation of the modified cabinet for the tests of the magnetic wine cooler prototype.

The data acquisition is performed by a commercial data logger (National Instruments) connected to a computer software (LabView) which also provides the logic for the flow

Table 3 – Specification of the measuring instruments.

Sensor	Manufacturer	Model	Uncertainty
Thermocouple (air)	Omega	Type T Wire PR-T-24-SLE-ROHS	0.12 °C
Thermocouple (water)	Omega	Probe TMQSS-062G-6	0.10 °C
Pressure transducer	Omega	PX309	0.48 bar
Flow meter	Aalborg	PWE04P-VLN-B2	11 L/h
Torque transducer	HBM	T22	0.5 %
Air humidity transducer	Testo	6681/6610	1.0 %
Hall sensor	Lake Shore	HGT-1010	1.0 %

control strategy. The components of the data acquisition system are summarized in Tab. 4.

Table 4 – Main components of the data acquisition system.

Component	Model
Chassi	NI SCXI-1000 (4 slots)
Board	NI PCI-6259
Modules	NI SCXI-1303 (32 channels)

3.2.5 *Experimental Procedure*

The experimental tests of the magnetic wine cooler prototype aim to enable the comparison between the vapor compression and magnetic cooling technologies operating over the same cabinet. To that purpose, it is necessary to first understand the range of possible operation points that the magnetic wine cooler prototype can deliver. Therefore, performance maps of the prototype shall be developed in terms of *COP*, second law efficiency and steady-state cabinet temperature of the cabinet, as functions of performance variables such as operating frequency and flow rate.

The input variables of the tests are then the operating frequency and the volumetric flow rate. The ranges of the operating frequency and volumetric flow rate are 0.5 to 1 Hz, with steps of 0.25 Hz, and 125 to 225 L/h, with steps of 25 L/h, respectively. The fixed parameters are the blow fraction, kept at 23% to avoid pressure peaks due to delay in the opening time of the valves, the power supplied to the cold and hot side fans and the ambient temperature, kept at 25±1°C by a split air conditioner installed at the test room. The air relative humidity is monitored and expected to be between 40% and 70%. The output variables are the air temperature inside the cabinet, the fluid temperatures along the hydraulic circuit and the power consumption of valves, fans, pumping system and magnet drive systems. The input and fixed parameters are summarised in Tab. 5. Combinations of the two input variables generate fifteen performance tests, named according to Tab. 6.

To initiate the tests for the performance map development, the temperatures of the air inside the cabinet, the surroundings air and the internal working fluid must be in equilibrium within 25±1°C. Once this equilibrium is reached, the frequency of the magnet is set according to each test and the magnet rotating system is switched on. The pump speed is set at a low value and the pumping system is switched on. At this point, the valves are closed and the

Table 5 – Parameters of the prototype for the performance tests.

Parameters	Values
Operating frequency [Hz]	0.5, 0.75 and 1.0
Volumetric flow rate [L/h]	125, 150, 175, 200 and 225
Blow fraction [%]	23
Cold fan power [W]	3.8 (100%)
Hot fan power [W]	8.3 (100%)
Ambient temperature [°C]	25±1
Air relative humidity [%]	40 to 70

Table 6 – Performance tests.

Operating Frequency [Hz]	Volumetric Flow Rate [L/h]				
	125	150	175	200	225
0.5	F50V125	F50V150	F50V175	F50V200	F50V225
0.75	F75V125	F75V150	F75V175	F75V200	F75V225
1.0	F100V125	F100V150	F100V175	F100V200	F100V225

working fluid flows through a relief bypass. Once the magnet completes one cycle, the valves are actuated and the hot side fans are switched on. At this moment, the AMR cycle initiates and the working fluid temperature starts to decrease. The pump speed is raised until the volumetric flow rate reaches the desired value according to the test. The cold side fan is kept off in order to provide a more pronounced temperature decrease. Once the working fluid temperature stabilizes, the cold side fan is switched on, increasing the heat exchange between the working fluid and the air inside the cabinet. Lastly, once the system reaches steady state, the test is recorded for a period of two minutes. As the room temperature is controlled by a split air conditioner, the temperature of the surrounding air and of inlet and outlet air streams of the HHEx reach a cyclic steady state, since they are directly dependent of the air conditioning behavior. Thus, the steady state criterion is fulfilled when the inlet and outlet temperatures of the two streams of the CHEx become constant as well as the temperatures inside the cabinet.

As the initial tests required to develop the performance maps are finished, the data are analyzed in terms of the *COP*, second-law efficiency, steady-state cabinet temperature and power consumption. A first comparison of the magnetic wine cooler prototype and the conventional system is made by an evaluation of the second-law efficiency as a function of the steady-state cabinet temperature for both systems, in order to place the data on the same baseline. Then, a few points of the magnetic wine cooler characterization will be selected for further tests, such as temperature pull down time and the influence of the cold fan power in the steady-state cabinet temperature.

The temperature pull down tests are performed in two different methods, regarding the instant in which the cold fan is switched on. First, the cold fan will be switched on only when the working fluid temperature stabilizes, in order to achieve a sharper temperature decrease, as explained previously in the procedure of the tests for the development of the performance map. Second, the cold fan will be switched on at the same instant as the beginning of the AMR cycle. The purpose of the two methods is to compare both temperature pull down

times.

The tests to investigate the influence of the cold fan power consumption are performed at steady state, with the power consumption of the cold fan varying within 100 to 25% of its the total power, in steps of 25%. The operating frequency and the fluid volumetric flow rate are kept constant. When each condition reaches steady state, the data are recorded over a period of two minutes. The purpose of these tests is to learn in what point the thermal load imposed by the cold fan inside the cabinet starts to contribute to the increase of the cabinet average temperature despite the increased air flow rate and heat transfer, thus finding an optimum power consumption for the fan in the specified test point.

3.2.6 Magnetic Wine Cooler Thermodynamic Analysis

The thermodynamic performance of the magnetic wine cooler is evaluated in terms of the coefficient of performance (*COP*) and the second law efficiency (η_{2nd}). The *COP* is the ratio between the cooling capacity and the total power consumption of the system. The cooling capacity is calculated as the thermal load imposed by the surroundings on the refrigerated cabinet plus the power dissipated by the cold fan inside the cabinet. Thus, the *COP* is calculated as presented in Eq. (3.6):

$$COP = \frac{\dot{Q}_{\text{load}} + \dot{W}_{\text{CF}}}{\dot{W}_{\text{P}} + \dot{W}_{\text{Mo}} + \dot{W}_{\text{CF}} + \dot{W}_{\text{HF}} + \dot{W}_{\text{V}}} \tag{3.6}$$

where $\dot{W}_{\text{P}}$, $\dot{W}_{\text{Mo}}$, $\dot{W}_{\text{CF}}$, $\dot{W}_{\text{HF}}$ and $\dot{W}_{\text{V}}$ are the power consumption of the pumping system, the magnet rotating system, the cold fan, the hot fan and the valves, respectively. $\dot{Q}_{\text{load}}$ is the thermal load and is calculated as follows in Eq. (3.7):

$$\dot{Q}_{\text{load}} = UA_{\text{cab}}(\overline{T}_{\text{amb}} - \overline{T}_{\text{cab}}) \tag{3.7}$$

where $\overline{T}_{\text{amb}}$ and $\overline{T}_{\text{cab}}$ are the average temperature of the surroundings and the average temperature of the cabinet, respectively. The cooling capacity was not considered as the energy balance in the liquid current of the CHEx due to the high uncertainty associated with the results, as the uncertainty of the calibrated thermocouples were about the same order of magnitude as the temperature difference in the outlet and inlet of the CHEx.

The power consumption of the pumping system is calculated through the viscous dissipation, with a pump efficiency of 21%[4], as follows in Eq. (3.8):

$$\dot{W}_{\text{P}} = \frac{\dot{V}_{\text{f}}(p_{\text{out}} - p_{\text{in}})}{\eta_P} \tag{3.8}$$

where $\dot{V}_{\text{f}}$, p_{in} and p_{out} correspond to the volumetric fluid flow rate, and the measured fluid pressures at the inlet and outlet of the pump, respectively. The power consumption of the

[4] The efficiency of the pump was based on catalogue information and further validated with experimental data, as will be explained further in Chapter 4.

magnet rotating system is calculated as presented in Eq. (3.9), with a efficiency of the electrical motor of 81%[5].

$$\dot{W}_{\mathrm{Mo}} = \frac{2\pi f \Gamma}{\eta_{\mathrm{M}}} \tag{3.9}$$

where f and Γ correspond to the operating frequency and the measured torque, respectively. The power consumption of the cold and hot fans as well as the valves are calculated through the measured current and voltage values.

The Carnot *COP* and the internally ideal *COP* are calculated as follows in Eq. (3.10) and (3.11):

$$COP_{\mathrm{Carnot}} = \frac{\overline{T}_{\mathrm{cab}}}{\overline{T}_{\mathrm{amb}} - \overline{T}_{\mathrm{cab}}} \tag{3.10}$$

$$COP_{\mathrm{ii}} = \frac{\overline{T}_{\mathrm{CHEx,in}}}{\overline{T}_{\mathrm{HHEx,in}} - \overline{T}_{\mathrm{CHEx,in}}} \tag{3.11}$$

where $T_{\mathrm{CHEx,in}}$ and $T_{\mathrm{HHEx,in}}$ are the average temperatures in the inlets of the cold and hot heat exchangers, respectively. The overall, internal and external second-law efficiencies are calculated as presented in Sec. 2.3.

[5] The efficiency of the electrical motor that drives the magnetic system was based on catalogue information.

4 Results

This chapter presents the experimental results of the characterization tests of vapor compression and magnetocaloric cooling technologies and the comparison between their thermodynamic performances. For this purpose, the chapter is divided in three sections. The first section presents the results of the characterization tests carried out with the vapor compression wine cooler, comprising the temperature pull down, annual energy consumption and reverse heat leakage tests, as well as the thermodynamic analysis. The second section presents the results of the characterization tests carried out with the magnetic wine cooler prototype, comprising results of steady-state temperature, cooling capacity, power consumption as well as the thermodynamic analysis of each test point. A further analysis based on the magnetic wine cooler results is also presented in this section, in terms of possible improvement points for the prototype. Lastly, the third section presents the comparison between both cooling technologies by means of η_{2nd}, *COP*, average annual energy consumption, cooling capacity and temperature pull down time, as well as some additional comments.

4.1 Conventional Wine Cooler Characterization

The results of the characterization tests for the conventional wine cooler are presented below, following the order described in Sec. 3.1. The first results are from the temperature pull down tests, followed by the annual energy consumption and the reverse heat leakage tests. Lastly, the results of the thermodynamic analysis of the vapor compression wine cooler to further comparison with the magnetic prototype.

4.1.1 Temperature Pull Down Test

The first of the baseline characterization tests for the conventional wine cooler was the temperature pull down test, aiming to characterize mainly the transient response curve of the system. The tests were performed in a 25±0.5ºC controlled environment. The pull down time was considered as the time required for the average cabinet temperature to reach the temperature set in the onboard control. The average cabinet temperature was calculated as the weighted average of the volume percentage of each compartment — 30 and 70% of the total cabinet internal volume for the upper and lower compartment, respectively.

Two tests were carried out in a standard operation: one with the internal temperatures set to 8ºC and another with the internal temperatures set to 12ºC. The temperature pull down curves for 8 and 12ºC are presented in Fig. 31 and Fig. 32, respectively, showing the ambient temperature and the average cabinet temperature during the test. The temperature pull down time for the set temperature of 8ºC was about 1.4 hours and the temperature pull down time for the set temperature of 12ºC was about 1.1 hours. The behaviour of the

temperature profile for the upper and lower cabinet experience a change at around 0.9 h for the 8ºC test and 0.6 h for the 12ºC test. In both tests, the temperature of the upper cabinet — previously at a higher level than the lower cabinet, starts to decrease at a higher rate, while the temperature of the lower cabinet starts to slightly increase. In the 12ºC test, this behavior was yet reversed again before the pull down time was reached. This behaviour is due to the change in the management of the refrigerant flow rate for each of the evaporators, carried out by the solenoid valves (see Fig. 13 in Sec. 3.1.1), that changes the priority according to the control logic.

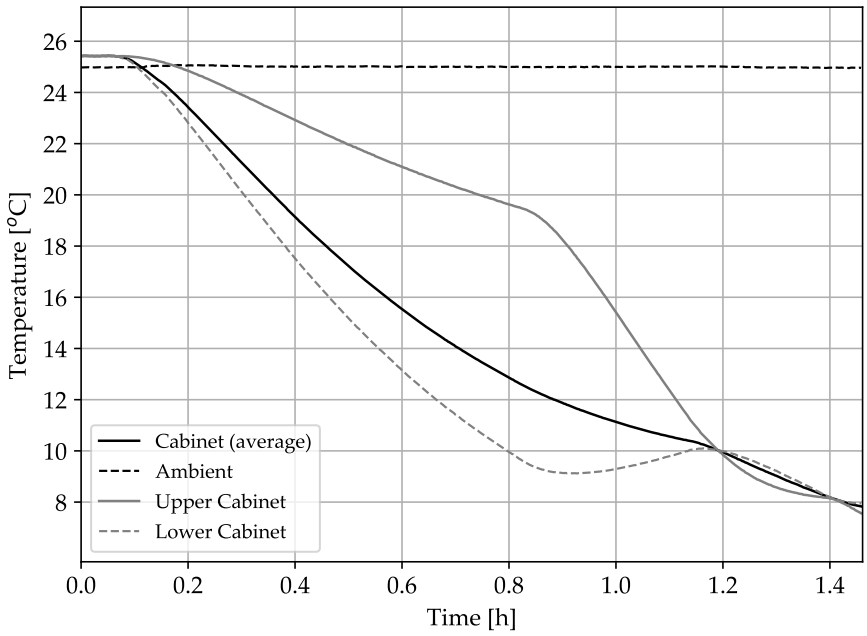

Figure 31 – Ambient and average cabinet temperature during the pull down time test for a thermostat temperature of 8ºC and ambient temperature of 25ºC.

4.1.2 *Energy Consumption Test*

The second of the baseline characterization tests was the evaluation of the annual energy consumption. Two tests were carried out for each average internal temperature set in the onboard control, i.e., 8ºC and 12ºC, in a 25±0.5ºC controlled environment. The curves of the total power consumption of the product and the average cabinet temperatures for each compartment during a period of 5 hours are presented in Figs. 33 and 34, for 8 and 12ºC, respectively.

The results of the average annual energy consumption per year are presented in Tab. 7, based on the extrapolation of the power consumption of the product integrated over a test period of 5 hours. The test with 8ºC in the onboard control presented a much greater annual energy consumption — 368 kWh/year, when compared to the 12ºC test — 272 kWh/year, as it required a higher cooling capacity to maintain the lower level of steady-state cabinet temperature. As can be noticed in Figs. 33 and 34, the compressor performed more cycles for the 8ºC test than for the 12ºC, during the same time interval, therefore increasing the

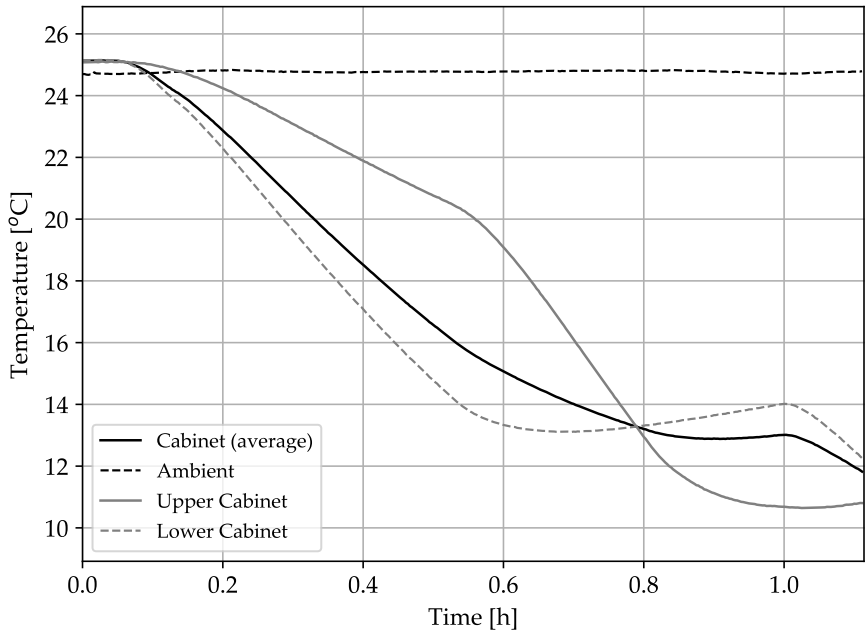

Figure 32 – Ambient and average cabinet temperatures during the temperature pull down test for a thermostat temperature of 12ºC and ambient temperature of 25ºC.

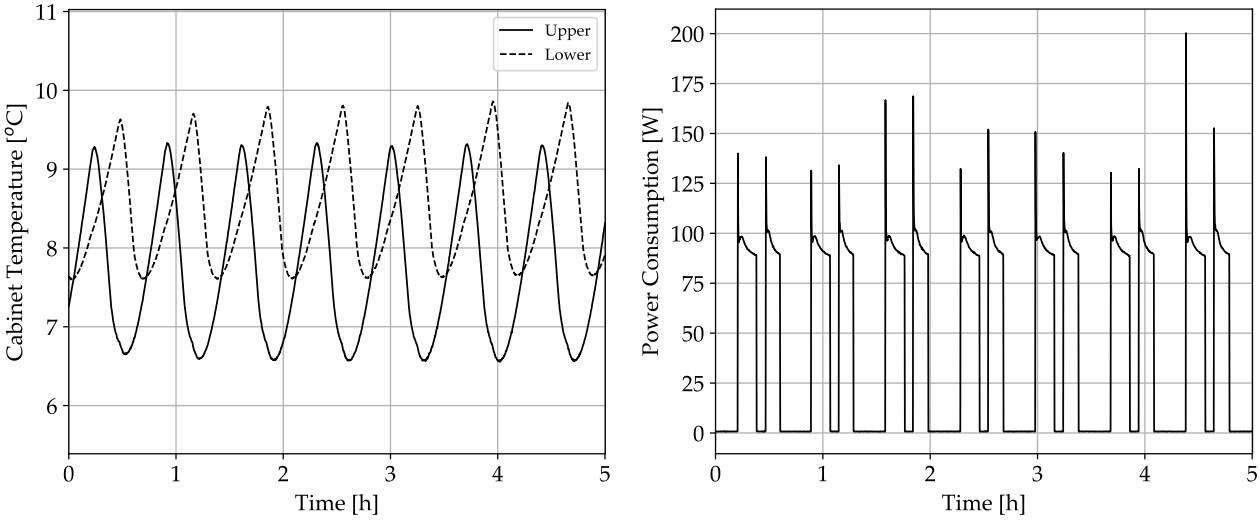

(a) (b)

Figure 33 – Average (a) cabinet temperature and (b) power consumption of the product for 5 hours of test running in periodic steady state for a thermostat temperature of 8ºC and ambient temperature of 25ºC.

average power consumption during the test period. Both test points presented an annual energy consumption greater that the limit of 175 kWh/year allowed for wine cooler applications, according to IEC 62552 (2015). Through catalogue information, the compressor of the conventional wine cooler has a capacity of 170 W, which is around the same average capacities from compressors used in refrigerators with both fresh food and freezer compartments. Thus, the very higher annual energy consumption can be associated with an oversized compressor for the wine cooler application.

As the average temperatures of the compartments acquired with the thermocouples

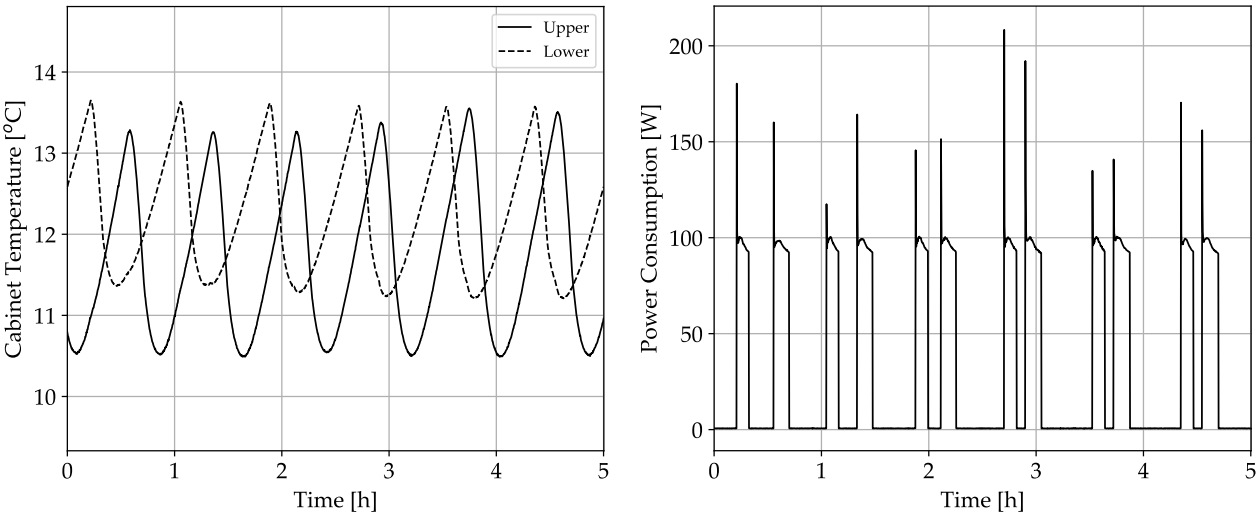

(a) (b)

Figure 34 – Average (a) cabinet temperature and (b) power consumption of the product for 5 hours of test running in periodic steady state for a thermostat temperature of 12ºC and ambient temperature of 25ºC.

Table 7 – Results of the annual energy consumption of the product for an ambient temperature of 25±0.5ºC.

Parameters	**Temperature [ºC]**	
	8	12
Average temperature in the upper compartment [ºC]	7.7	11.7
Average temperature in the lower compartment [ºC]	8.5	12.2
Energy Consumption [kWh/year]	369	272

are different than the temperatures set by the controls, a reference temperature was calculated for each test to establish the endpoints of the interpolation interval. The reference temperatures were calculated through the weighted average of the volume percentage of each compartment. The average temperature endpoints and the respective annual energy consumption are summarized in Tab. 8.

Table 8 – Results of the annual energy consumption of the product for the average temperature inside the cabinet.

Cabinet Temperature [ºC]	**Energy consumption [kWh/year]**
8.2	369
12.1	272

4.1.3 Reverse Heat Leakage Test

The last of the baseline characterization tests is the RHL test, aiming to determine the overall thermal conductance (*UA*) of the cabinet. By imposing a heat generation inside the cabinet and measurements of temperature (cabinet and ambient) and power dissipated by the resistances, the *UA* was calculated by the least-squares method. As there are two com-

partments inside the cabinet, four linearly independent tests were carried out, as previously presented in Tab. 2 (see Sec. 3.1.6). The experimental data results are presented in Tab. 9.

Table 9 – Experimental data of the RHL tests.

Parameters	**Test**			
	1	2	3	4
Temperature of the upper compartment [°C]	50.1	61.1	50.2	58.8
Temperature of the lower compartment [°C]	35.0	39.7	50.2	50.2
Temperature of the surroundings [°C]	20.8	22.0	21.1	21.1
Power dissipated in upper compartment [W]	9.8	12.6	31.0	28.2
Power dissipated in lower compartment [W]	24.6	35.4	19.3	29.3

By applying the experimental data obtained from the RHL tests in Eq. (3.1), the *UA* was calculated for each compartment. The *UA* of the cabinet was obtained through the sum of both UA_{up} and UA_{low}. The results are presented in Tab. 10.

Table 10 – Results of the overall thermal conductances.

Parameters	**Results**
UA of the upper compartment [W/°C]	0.69
UA of the lower compartment [W/°C]	1.05
UA of the cabinet [W/°C]	**1.74**

4.1.4 Conventional Wine Cooler Thermodynamic Analysis

The thermodynamic analysis of the conventional wine cooler followed the equations presented in Sec. 3.1.7. The analysis is presented for the control temperatures of 8 and 12°C, which corresponds to the average cabinet temperatures of 8.2 and 12.1, respectively.

The cooling capacities were 29.1 W for the 8°C test and 22.3 W for the 12°C test. The *COP* and second-law efficiency were, respectively, 0.68 and 4.0% for the set temperature of 8°C, and 0.70 and 3.1% for the set temperature of 12°C. The *COP* barely changed between the two test points, which reflected in a higher second-law efficiency for the 8°C test, as the Carnot *COP* is lower.

Fig. 35 (a) presents the analysis of the Carnot, internally ideal and actual *COP* and Fig. 35 (b) presents the analysis of the external, internal and overall second-law efficiencies for the two test points of the conventional wine cooler. As can be seen, although the 12°C test presented the highest Carnot and internally ideal *COP* — respectively 16.9 and 6.3 for the 8°C test and 22.3 and 8.3 for the 12°C test, the actual *COP* was practically the same of that of the 8°C test, which reflects in a lower overall and internal second-law efficiencies, the latter being 10.9% for the 8°C test and 8.5% for the 12°C test. For both tests, the external efficiency was practically the same, around 37.0%. This value represents the efficiency of the heat exchangers of conventional wine cooler, and as the two evaporators and the condenser are all exchanging heat with their respective environment by means of natural convection, thus a low value should be expected. The low efficiency of the heat exchangers could also be related to the oversized compressor. So as to compensate the extra capacity provided by the

compressor and maintain the levels of temperature for good wine quality, the evaporators could have been designed to be undersized.

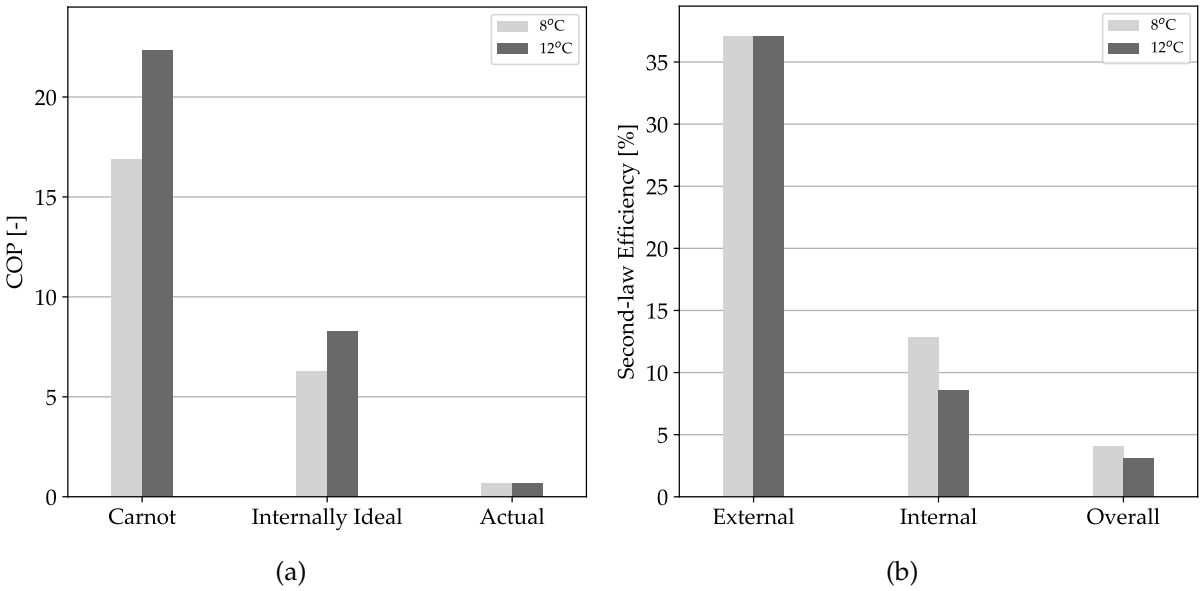

Figure 35 – (a) *COP* and (b) second-law efficiency for the conventional wine cooler.

The results of the thermodynamic analysis of the conventional wine cooler are summarized in Tab. 11.

Table 11 – Thermodynamic analysis of the conventional wine cooler.

Parameters	**Set Temperature [ºC]**	
	8	12
Temperature pull down time [h]	1.4	1.1
Average cabinet temperature [ºC]	8.2	12.1
Cooling capacity [W]	29.1	22.3
Energy consumption [kwh/year]	369	272
Coefficient of performance [-]	0.68	0.70
Second-law efficiency [%]	4.0	3.1

4.1.5 Uncertainty Analysis

The expanded uncertainties were calculated for the main variables of the characterization tests of the conventional wine cooler, for a 98% confidence interval and a combination of type A and B uncertainties. Table 12 presents the maximum expanded uncertainties of the main variables. The calculation procedure is presented in Appendix A.

4.2 Magnetic Wine Cooler Characterization

The results of the characterization tests for the magnetic wine cooler prototype are presented below, according to Sec. 3.2.5. The first results present the performance maps with steady-state temperature, cooling capacity, power consumption, *COP* and second-law

Table 12 – Expanded uncertainties associated with the experimentally determined variables (98% confidence interval).

Parameters	Uncertainty
Average air temperature [°C]	0.1
Average refrigerant fluid temperature [°C]	1.0
Overall thermal conductance [W/°C]	0.08
Cooling capacity [W]	1.4
Energy consumption [kWh/year]	46
Coefficient of performance [-]	0.15
Second-law efficiency [%]	0.9

efficiency. With the first results, suitable test conditions are selected for further analysis of pull down time and power consumption of the fan connected to the cold heat exchanger. Lastly, an evaluation of improvement points of the prototype is carried out.

4.2.1 Performance Tests

For the development of the performance maps of the prototype, fifteen tests were carried out according to the parameters presented in Tab. 6 (see Sec. 3.2.5), at an ambient temperature of 25±1°C and evaluated at steady state. The results of the tests are presented in the figures below.

Figure 36 presents the steady-state cabinet temperature as a function of the flow rate and operating frequency. The lowest cabinet temperature reached by the magnetic prototype was 10.8°C, obtained in the test F100V175 — 1.0 Hz and 175 L/h. The trend of the curves indicates that for each frequency there is an optimum condition that generates a minimum cabinet temperature. It is also noticeable that the lowest temperature occurred at a volumetric flow rate of 175 L/h for all operating frequencies, although for the operating frequency of 0.5 Hz the tests F50V150 and F50V175 presented very similar steady-state cabinet temperature, 11.9°C and 11.8°C, respectively.

The behavior of the steady-state cabinet temperature is mainly a reflection of two parameters — the cooling capacity provided by the magnetic prototype and the ambient temperature. Figure 37 presents the cooling capacity as a function of the flow rate and operating frequency. The maximum cooling capacity reached by the magnetic prototype was 27.9 W, provided by the test point F100V175. For the operating frequencies of 0.5 Hz and 0.75 Hz, the highest cooling capacities were reached for the test points F50V150 and F75V175, respectively. The cooling capacity depends on a combination of effects, such as the regenerator effectiveness, the inlet temperature of the working fluid in the regenerator hot side and the flow rate. The regenerator effectiveness is a function of the utilization factor (ϕ) and the NTU (see Sec. 2.2.3), and it is higher for low utilizations and high NTU. The inlet temperature of the working fluid in the regenerator hot side is affected by the extra heat added by the power dissipation of the pump, which is increases with the flow rate. Thus, although the cooling capacity is directly proportional to the flow rate, higher flow rate values contribute to the increase of the utilization factor and the decrease of the NTU,

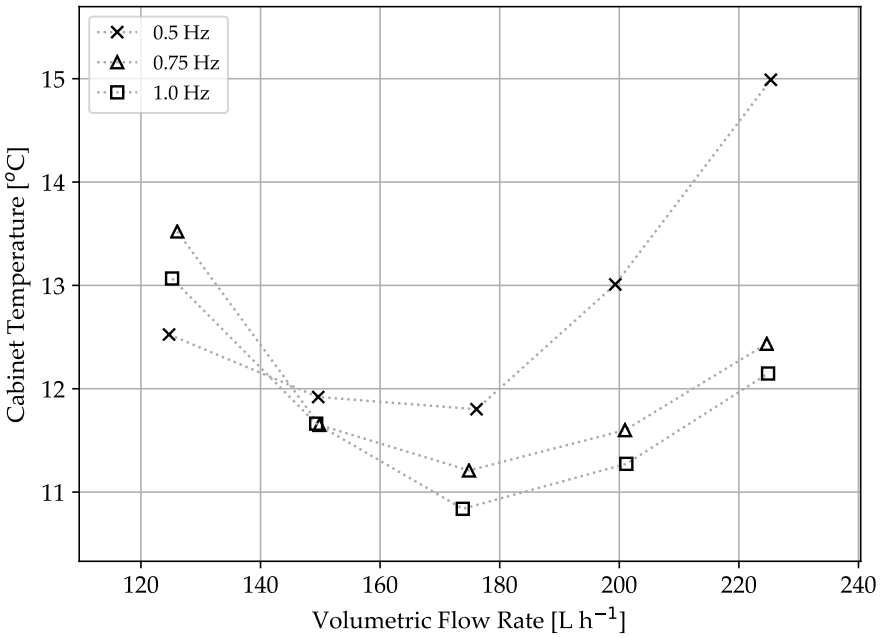

Figure 36 – Results of the steady-state cabinet temperature as a function of the volumetric flow rate and operating frequency.

leading to lower regenerator effectiveness. Also, higher flow rate values contributes to a higher viscous power dissipation, leading to higher temperatures in the regenerator inlet and compromising the magnetocaloric effect in the regenerator layers.

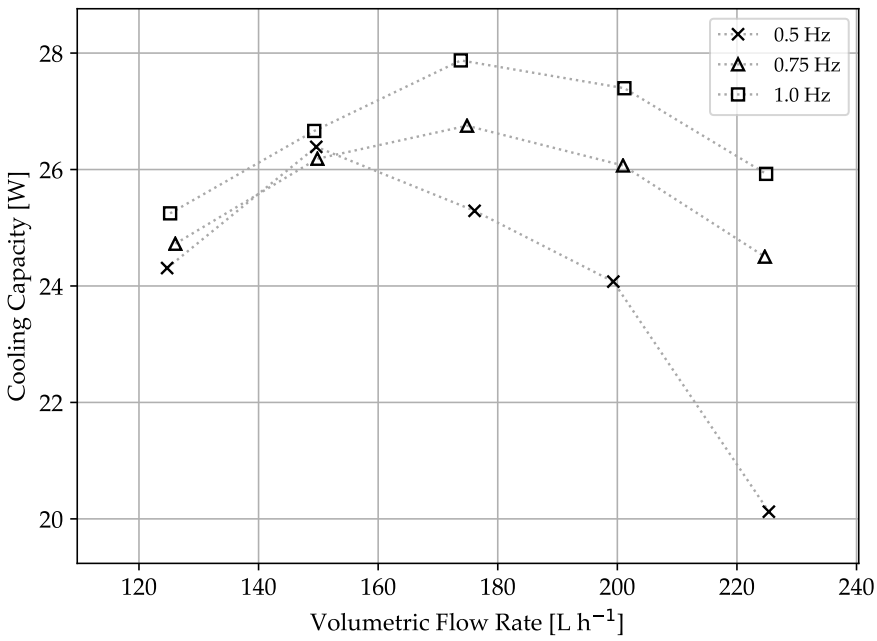

Figure 37 – Results of the cooling capacity as a function of the volumetric flow rate and operating frequency.

For the curves with operating frequencies of 0.75 and 1.0 Hz, the test points that reached the highest cooling capacities were also the test points that reached the lowest cabinet temperatures — F75V175 and F100V175, as expected. However, for the operating frequency of 0.5 Hz, the highest cooling capacity was reached in the test point F50V150, while the lowest

temperature was reached for test point F50V175. This discrepancy is due to the influence of the ambient temperature on the steady-state cabinet temperature. For the F50V150 test, the cabinet temperature was 11.9ºC for an ambient temperature of 24.8ºC, which represents a ΔT_{sys}[1] of 12.9ºC. For the F50V175 test, the cabinet temperature was 11.8ºC for an ambient temperature of 24.0ºC, representing a ΔT_{sys} of 12.2ºC. With the higher ambient temperature, the F50V150 test was subjected to a higher heat load. Thus, although the F50V150 test presented a higher steady-state cabinet temperature, if both tests — F50V150 and F50V175, were carried out at the exact same ambient temperature, the F50V150 test would have presented the lowest steady-state cabinet temperature for the operating frequency of 0.5 Hz, as it presented a higher ΔT_{sys}.

Figure 38 presents the total power consumption of the prototype as a function of the flow rate and operating frequency. The total power consumption comprises the power to operate the pump, the fans, the valves and the power to drive the magnetic circuit. Although the power consumption increases with both the flow rate and the operating operating frequency, the most influential parameter is the flow rate, which more than triples the power consumption results of the volumetric flow rate from 125 L/h to 225 L/h.

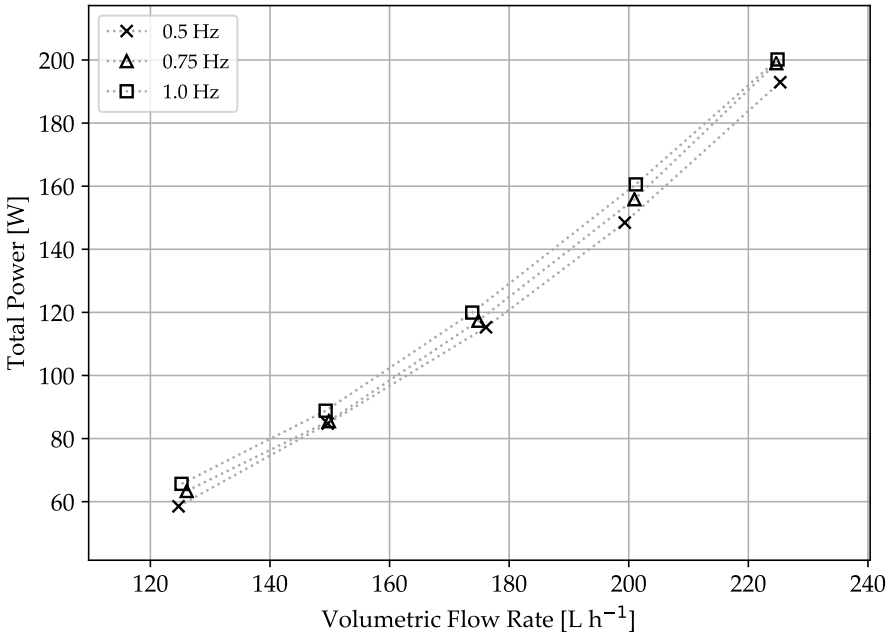

Figure 38 – Results of the total power consumption of the prototype as a function of the volumetric flow rate and operating frequency.

The contribution of each share of the power consumption is also evaluated as a function of the flow rate and operating frequency, as presented in the Figs. 39 (a) and (b), respectively. Figs. 39 (a) presents the contribution of each power share with the volumetric flow rate, for a fixed frequency of 1.0 Hz. The power required to operate the pump was the dominant contribution of the total power consumption, as well as the most affected by the flow rate, varying from ~ 50% for the flow rate of 125 L/h to ~ 81% for the flow rate of 225 L/h.

[1] ΔT_{sys} is the temperature span of the system, which is the difference between the temperature of the external ambient and the refrigerated cabinet. For more details, see Fig. 24 in Sec. 3.2.3.

Figs. 39 (b) presents the contribution of each power share with the operating frequency, for a fixed volumetric flow rate of 150 L/h. Both magnetic and valve contributions increase with frequency due to a greater number of AMR/magnet cycles performed, but overall the contributions for the total power consumption did not change significantly with the frequency.

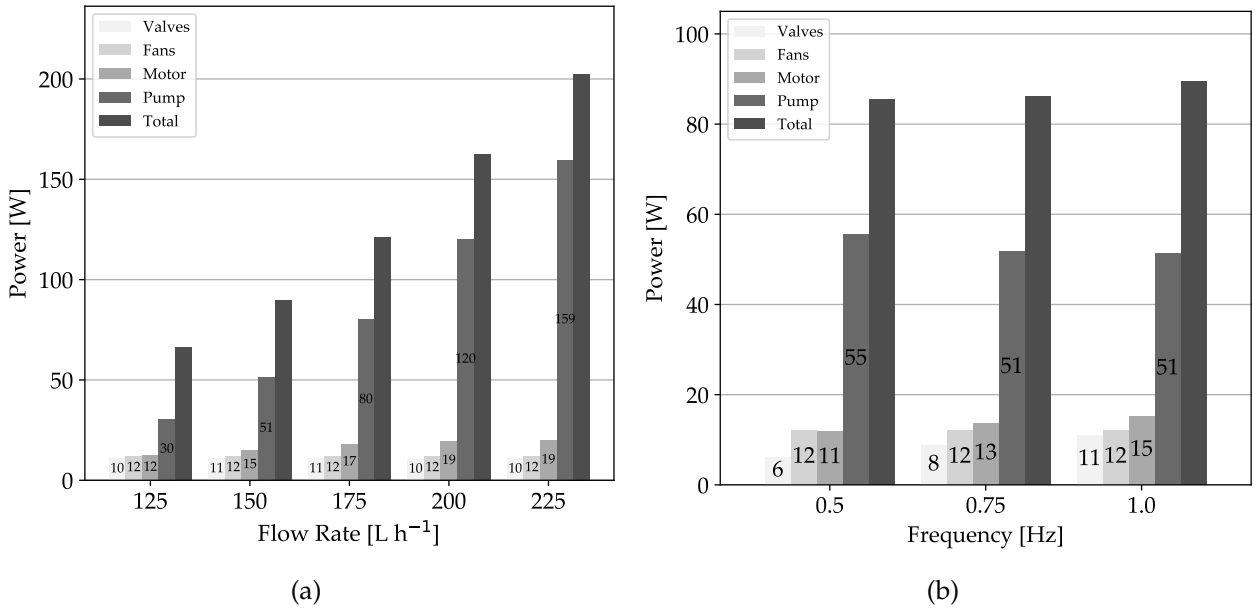

Figure 39 – Contribution of each component in the power consumption of the prototype as a function of (a) the volumetric flow rate for a magnetic frequency of 1.0 Hz and (b) the magnetic frequency for a volumetric flow rate of 150 L/h.

Figure 40 presents the annual energy consumption, in kWh/year, as a function of the flow rate and operating frequency. Due to the significant increase of the pumping power and total power consumption with the flow rate, the annual energy consumption of the prototype reaches extreme values at high volumetric flow rates. The lowest values of annual energy consumption are reached for the volumetric flow rate of 125 L/h, being 505, 548 and 567 kWh/year for the operating frequencies of 0.5, 0.75 and 1.0 Hz, respectively. The annual energy consumption for the test point F100V175 was 1036 kWh/year.

With results of steady-state cabinet temperature, cooling capacity and total power consumption of the magnetic prototype, the thermodynamic efficiency metrics, i.e, the *COP* and the second-law efficiency, were calculated and are presented in Fig 41 and 42, respectively. The *COP* decreases steadily with the flow rate, despite the fact that the cooling capacity curves exhibited points of maximum. The *COP* behavior is mostly affected by the considerable increase in the required pumping power with the flow rate, which represents a much greater variation from that experienced by the cooling capacity. A similar trend is observed in the second-law efficiency, but for an operating frequency of 0.5 Hz the η_{2nd} is somewhat reduced at a higher rate for high flow rates, because of the increase of the ideal COP_{Carnot} with the pronounced increase of the steady-state cabinet temperatures. The best *COP* and second-law efficiency achieved by the prototype was 0.41 and 1.7%, respectively, obtained in the test point F50V125. The and second-law efficiency of the test point F100V175, with the

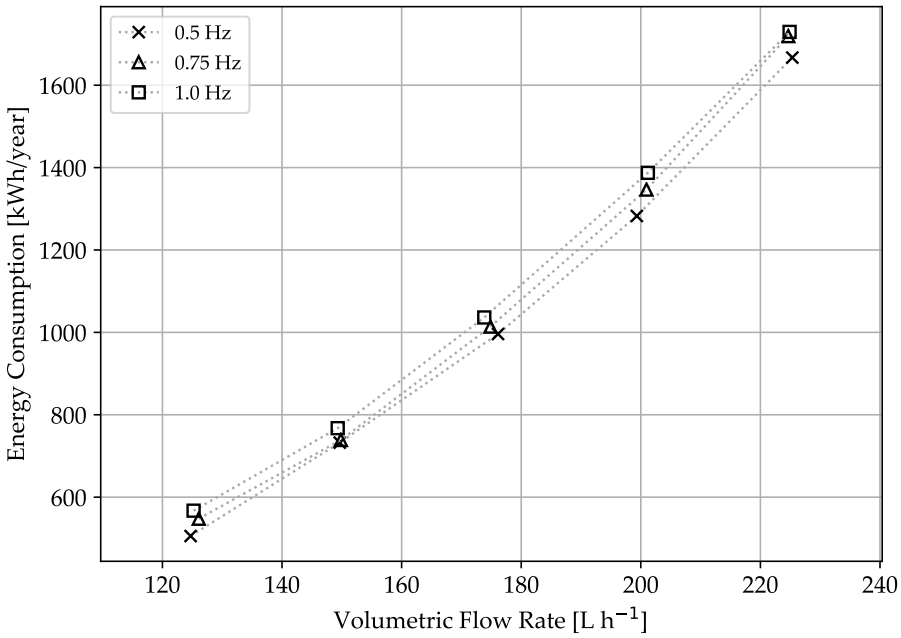

Figure 40 – Results of the annual energy consumption of the prototype as a function of the volumetric flow rate and operating frequency.

lowest cabinet temperature, was 0.23 and 1.1%.

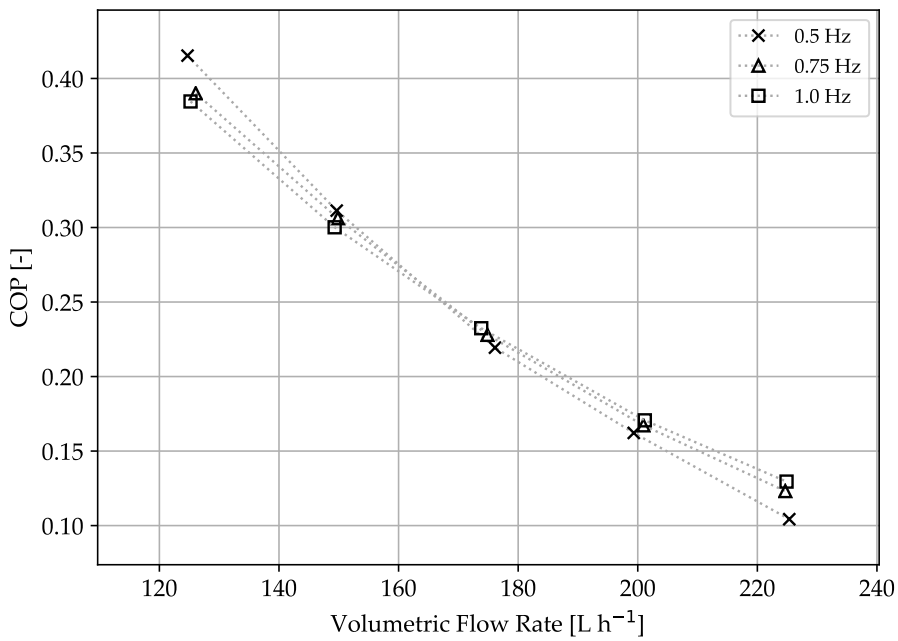

Figure 41 – Results of the coefficient of performance as a function of the volumetric flow rate and operating frequency.

Figures 43 (a) and (b) present the Carnot and internally ideal *COP* as a function of the flow rate and operating frequency. Contrarily to the behavior of the actual in decreasing with the increase of flow rate, both Carnot and internally ideal *COP* showed a behavior of minimum points for each operating frequency. The Carnot exhibited minimum points for the tests in which the temperature span between the cabinet and ambient (ΔT_{sys}) are the highest, corresponding to the tests with the highest cooling capacities. The internally ideal

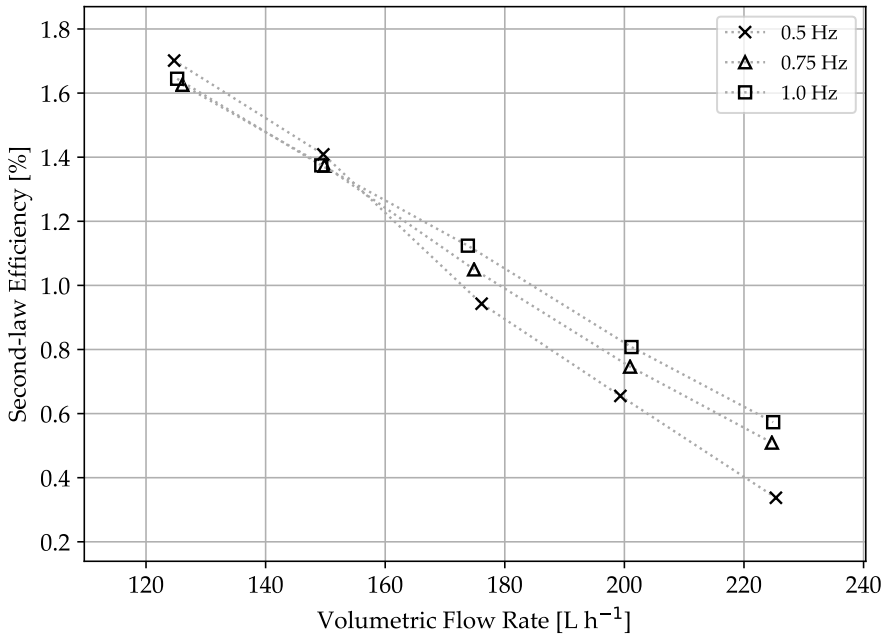

Figure 42 – Results of the second-law efficiency as a function of the volumetric flow rate and operating frequency.

COP exhibited minimum points for the tests in which the temperature difference between the HHEx and CHEx inlets were the highest — or the $\Delta T_{\text{reg,out}}$ (see Sec. 3.2.3), corresponding to the temperature span in the regenerator.

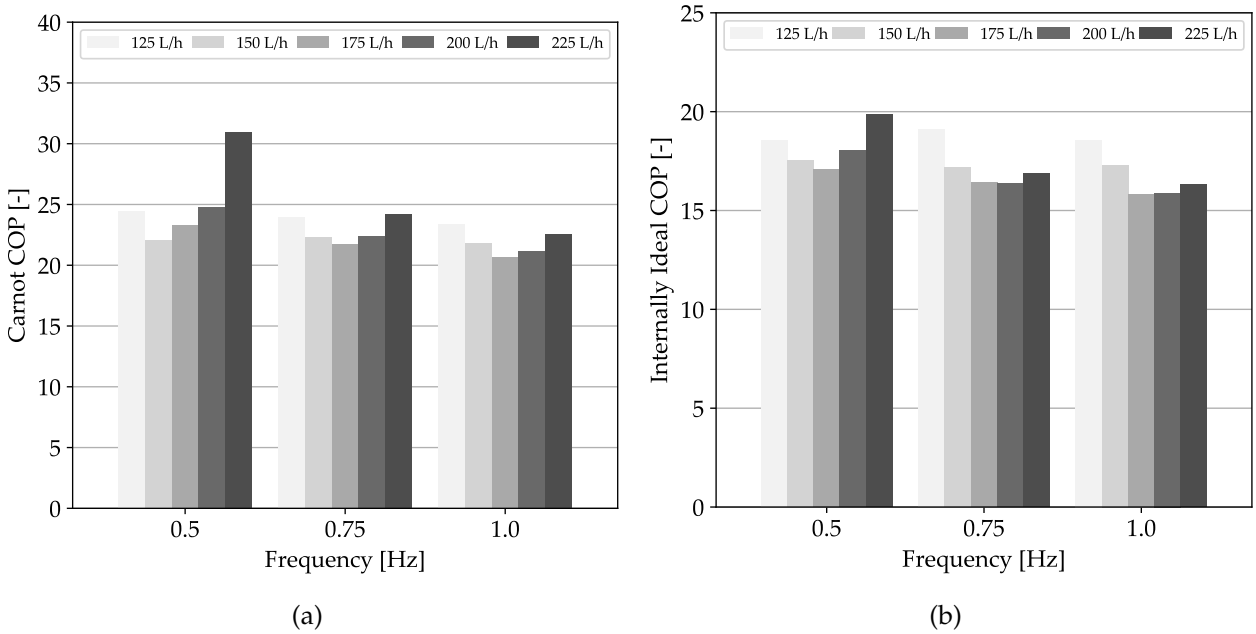

Figure 43 – Results of (a) Carnot *COP* and (b) internally ideal *COP* of the magnetic wine cooler prototype.

Figures 44 (a) and (b) present the external and internal second-law efficiencies as a function of the the flow rate and operating frequency. The external efficiencies are high, with a mean value around 75.0%, which not only reflects the enhancement of the forced convection heat exchange, but also indicates a good selection of the heat exchangers and

fans by the Cabinet/Heat Exchangers Subsystem during the design phase of the prototype. The internal efficiencies decrease abruptly with the flow rate, mainly as a consequence of the pronounced increase of the pumping power and the consequent decrease of the actual *COP*. The internal efficiencies are low, indicating that the thermodynamic losses of the magnetic prototype can be quite high. This combined with the high values of internally ideal *COP* suggests there is still great potential for improvement in the magnetic technology.

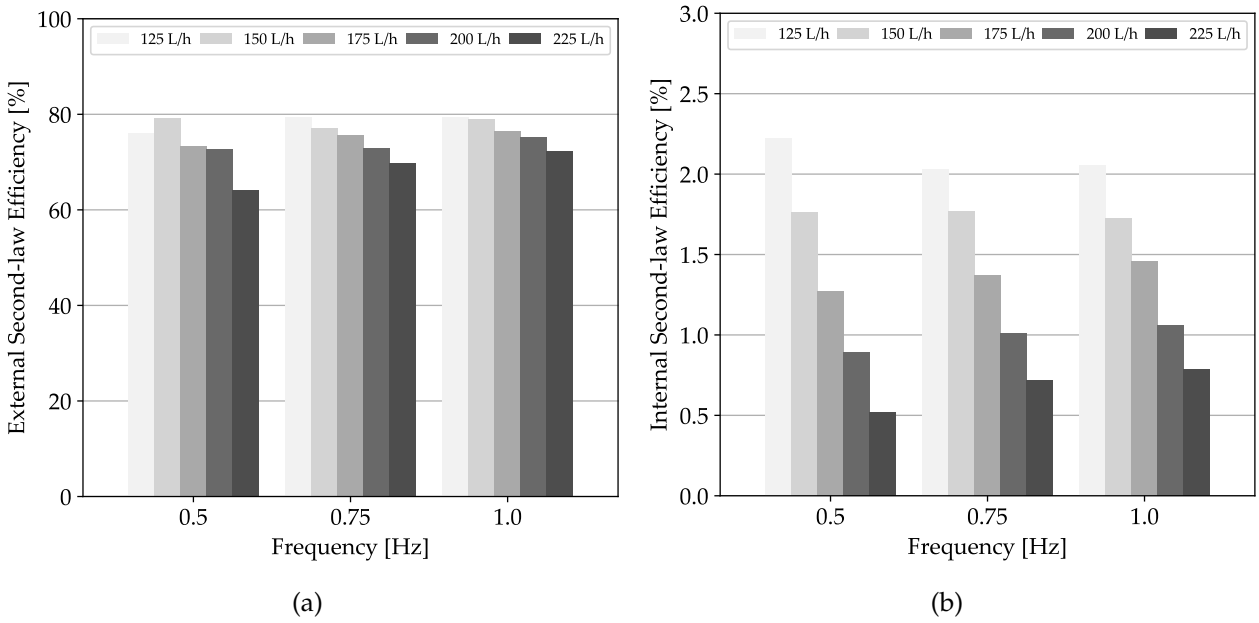

Figure 44 – Results of (a) external and (b) internal second-law efficiencies of the magnetic wine cooler prototype.

With the results of the performance tests, two tests were selected to further studies: the best operating point in terms of the lowest steady-state cabinet temperature (F100V175) and the best operating point in terms of efficiency (F50V125).

4.2.2 *Temperature Pull Down Test*

The temperature pull down tests for the prototype were carried out at an ambient temperature of 25±1°C for the F100V175 and F50V125 test conditions using two methods that differ with respect to the instant when the cold fan is switched on, as explained in Sec. 3.2.5. Figures 45 and 46 present the results of the temperature pull down for method 1 — with the cold fan being switched on after the temperature of the working fluid starts to stabilize. In the graphic subtitle, the Regenerator Inlet stands for the temperature in the inlet of the regenerator in the hot end — which corresponds to the temperature exiting the HHEx, and Regenerator Outlet stands for the temperature in the outlet of the regenerator in the cold end — which corresponds to the temperature entering the CHEx. Initially, the cold fan is kept off and thus the *UA* of the set cold HEx and fan is low, with a heat exchange between working fluid and cabinet air by means of natural convection. With a low heat exchange rate, the temperature of the fluid in the cold side decreases more abruptly when compared to the decrease rate of the cabinet temperature. Once the fluid temperature in the cold side starts

to stabilize[2], the fan is switched on, increasing suddenly the heat exchange between the heat transfer fluid and the cabinet air. Consequently, the temperature of the fluid in the CHEx outlet instantly starts to increase, yielding a higher temperature in the regenerator inlet on the cold side. With a higher fluid temperature entering the regenerators in the cold blow, the heat exchange between the working fluid and the solid refrigerant decreases, leading to a general increase of temperature on the cold side of the system and a decrease of the temperature span in the regenerator. Simultaneously, the temperature of the cabinet air starts decreasing at a higher rate, and as it achieves a certain temperature level, the temperature of the working fluid starts once again to decrease, and both continue decreasing until the steady state is reached. The pull down time for the F50V125 test was about 5 hours. The pull down time for the F100V175 test was about 2.5 hours, and it was defined as the instant when the steady-state cabinet temperature of the cabinet reached 12.0ºC, so as to be used in the further comparison with the conventional wine cooler.

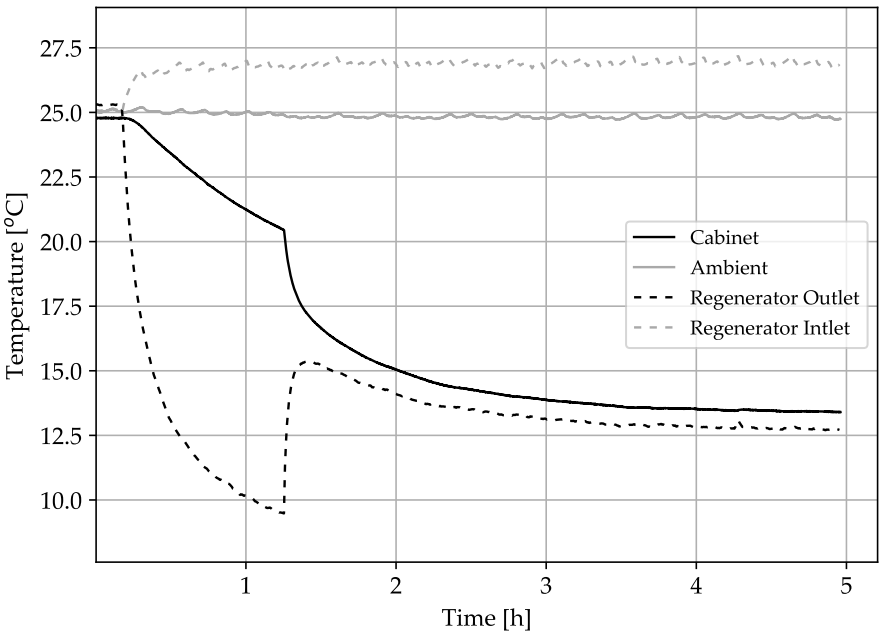

Figure 45 – Results of the temperature pull down of the prototype as a function of the time, for the test condition F50V125 and method 1.

Figure 47 presents the results of the temperature pull down for method 2 — with the cold fan being switched on together with the beginning of the AMR/Magnet cycle, and for the F100V175 test point. In this case, the heat exchange between working fluid and cabinet air occurs by means of forced convection during the entire test and the temperatures decrease together with a similar trend. The pull down time for the F100V175 test by this method was about 2 hours, and it was also defined as the instant when the steady-state cabinet temperature reached 12.0ºC. Thus, this last test method provided a temperature pull down time of about 0.5 hours less than the first method, showing that switching on the cold fan

[2] So as to not waste unnecessary time on the pull down test, this moment was defined as when the temperature in the cold side presents a noticeable reduction in the decrease rate once it has surpassed 10ºC. This temperature was identified as an average limit for the cold side when the cold fan is kept off for most test points in the preliminary tests.

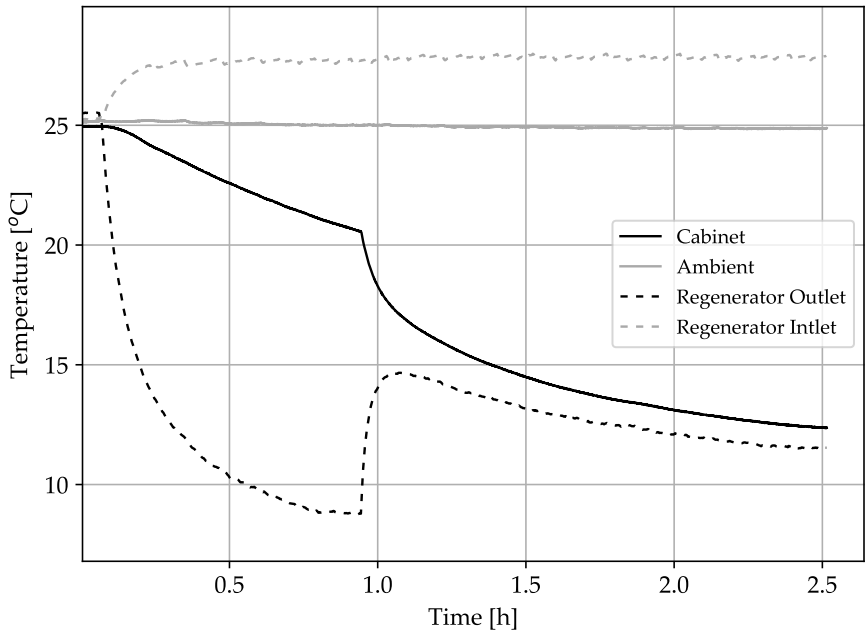

Figure 46 – Results of the temperature pull down of the prototype as a function of the time, for the test condition F100V175 and method 1.

with the AMR/Magnet cycle allows to reach lower temperatures faster than switching it on after some stabilization time.

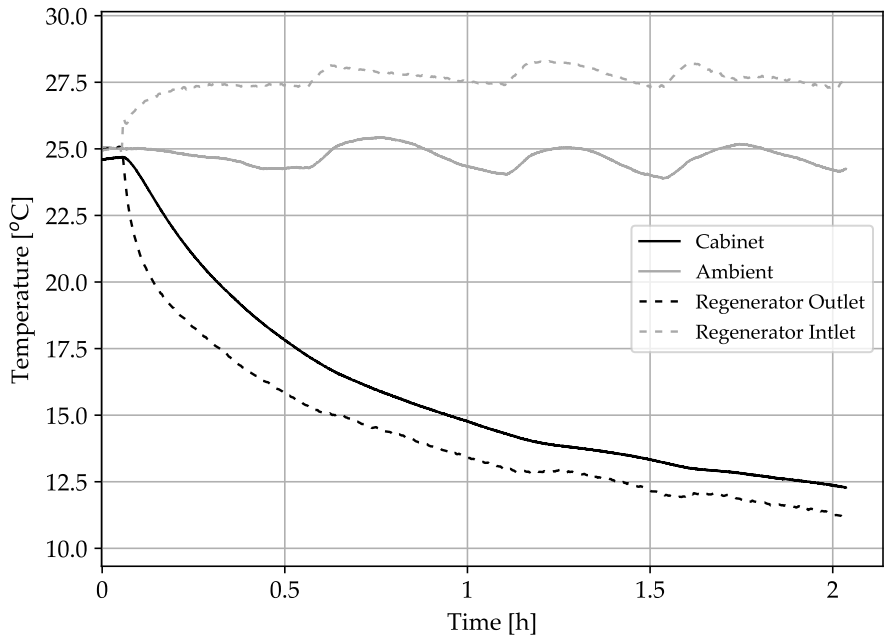

Figure 47 – Results of the temperature pull down of the prototype as a function of the time, for the test condition F100V175 and method 2.

4.2.3 *Influence of the Cold Fan Power Test*

The tests for the influence of the cold fan power in the steady-state cabinet temperature were also carried out for the F50V125 and F100V175 test points. The power supply to the

fan was varied from 100% to 25% of its total power, in steps of 25%. Fig. 48 presents the results for the steady-state cabinet temperature and the temperature stratification for both F50V125 and F100V175 test points. The cabinet temperatures decreased with the decrease of the fan power, and the lowest cabinet temperatures were achieved with 25% of the fan power supply. This results are due to the decrease of the heat load imposed by the fan inside the cabinet. As expected, with the decrease of the fan power supply the stratification of the cabinet temperature increased somewhat. According to the IEC 62552 (2015) standard, the stratification shall not surpass 0.5ºC for all measured points inside a compartment, and thus the test F100V175 with 25% of fan power supply was not considered as a valid point, as it provided a stratification of 0.6ºC.

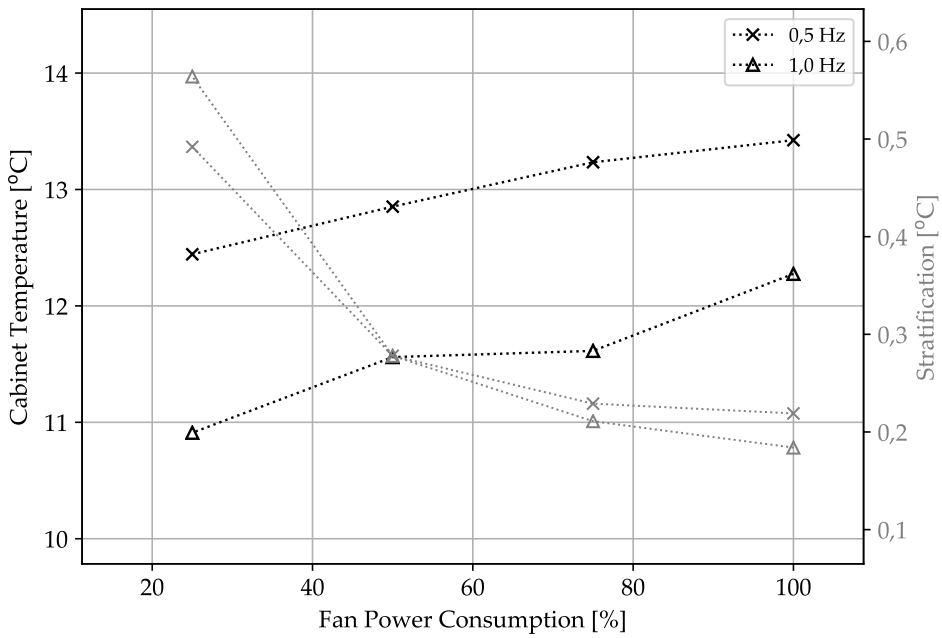

Figure 48 – Results of steady-state cabinet temperature and stratification level as a function of the power consumption of the fan, for the test points F50V125 and F100V175.

The F50V125 with 25% fan power (F50V125 @ 25%) and the F100V175 with 50% fan power (F100V175 @ 50%) provided the lowest cabinet temperature within the allowed limits of stratification. Tab. 13 presents the results of cabinet temperature, *COP*, second-law efficiency and annual energy consumption for each of the test points mentioned.

Table 13 – Results of the points with lowest cabinet temperatures within the stratification limits for the test of the fan power influence.

Parameters	**Test**	
	F50V125 @ 25%	F100V175 @ 50%
Average cabinet temperature [ºC]	12.4	11.5
Stratification [ºC]	0.49	0.28
COP [-]	0.40	0.20
η_{2nd} [%]	1.77	0.83
Energy consumption [kWh/year]	482	1015

The annual energy consumption of the tests with lower cold fan power resulted in a lower annual energy consumption in comparison with the test points F50V125 and F100V175 from the performance tests, as expected. For the F50V125 condition, the annual energy consumption was 510 kWh/year for a fan power of 100% and 482 for a fan power of 25%, a decrease of the order of 5%. For the F100V175 condition, the annual energy consumption was 1045 kWh/year for a fan power of 100% and 1015 for a fan power of 25%, a decrease of the order of 3%.

In terms of performance metrics, both tests with the lower cold fan power provided a slightly lower *COP*. The lower *COP* is a reflection of the lower cooling capacity. As the cooling capacity is calculated as the heat load imposed by the surroundings plus the power of the cold fan, even though the cabinet temperature was lower, so was the cold fan power, which resulted in a lower value of the cooling capacity. The second-law efficiencies, however, were higher for the tests with the lower fan power, as with a higher span between the ambient and cabinet the Carnot *COP* is lower. Table 14 presents a thermodynamic comparison between the F50V125 at 100% fan power and F100V175 at 25% fan power test points.

Table 14 – Thermodynamic comparison between the F50V125 at 100% and F100V175 at 25% test points.

Parameters	**Test**	
	F50V125 @ 100%	F100V125 @ 25%
System temperature span [°C]	11.6	12.4
COP [°C]	0.41	0.40
η_{2nd} [%]	1.7	1.8
Energy consumption [kWh/year]	510	482

4.2.4 Uncertainty Analysis

The expanded uncertainties were calculated for the main variables of the characterization tests of the magnetic wine cooler, for a 98% confidence interval and a combination of type A and B uncertainties. Each data point was acquired over a 2-minute sampling time, with a sampling frequency of 150 Hz for each test condition. Table 15 presents the maximum expanded uncertainties of the main variables. The calculation procedure is presented in Appendix A.

4.2.5 Evaluation of Improvement Points

As means to propose potential improvements to the magnetic wine cooler, this section presents a further analysis on specific aspects of the individual subsystems.

With the low values of internal second-law efficiency in contrast with the high values of internally ideal *COP* (see Figs. 43 and 44), a further analysis based on entropy generation was carried out in this work. As the pump has proven to be the most expressive portion of the total power consumption of the prototype, the entropy generation calculation was focused on the Hydraulic/Control subsystem and its contribution to the total entropy generation of

Table 15 – Maximum expanded uncertainties associated with the experimentally determined variables (98% confidence interval).

Parameter	Uncertainty
Volumetric flow rate [L/h]	13
Temperature [°C]	0.1
Pressure [bar]	0.5
Torque [Nm]	0.2
Pump power [W]	2
Motor Power [W]	2
Fan power [W]	0.3
Valve power [W]	1
Cooling capacity [W]	1.2
Energy consumption [kWh/year]	22
COP [-]	0.04
η_{2nd} [%]	0.2

the system. The entropy generation calculations are described in Appendix B, together with a further analysis on the other subsystems. Figure 49 presents the percentage of entropy generation of the prototype subsystems for the F50V125 test condition, with emphasis on the Hydraulic/Control subsystem. The entropy generation of the Hydraulic/Control subsystem included the generation due to: the pump, the pressure drop of the solenoid valves and some auxiliary components — such as the filters and the flow meter, and the heat losses in connections and tubing. The Hydraulic/Control subsystem contributes to more than two thirds of the total entropy generation, being responsible for the major contribution to the internal inefficiencies of the prototype. The Cabinet/Heat Exchanger and AMR/Magnet contribute together to less than one third of the entropy generation. In a deeper examination, the pump alone contributes with 45% of the total entropy generation of the prototype, representing a very critical point into the system inefficiency, and should be addressed first when considering the improvement of the prototype performance.

Figures 50 (a) and (b) present the power consumption of the pumping system and the heat dissipation of the pump to the working fluid, respectively, as a function of the flow rate and operating frequency. The heat dissipation of the pump was calculated as the product of the temperature difference between the pump ports and the thermal capacity rate of the fluid.

The high values of power consumption and heat dissipation are a consequence of the very low efficiency of the pump, around 20% according to the manufacturer data. With the results of heat dissipation and viscous power losses, an approximated efficiency of the pump was then calculated, as follows in Eq. (4.1), to get a sense of how accurate was the catalogue information.

$$\eta_{\mathrm{p}} = \frac{\dot{W}_{\mathrm{visc}}}{\dot{W}_{\mathrm{visc}} + \dot{Q}_{\mathrm{diss}}} \tag{4.1}$$

where $\dot{W}_{\mathrm{visc}}$ is the viscous power and $\dot{Q}_{\mathrm{diss}}$ is the heat dissipation of the pump to the working fluid. The results pointed to an overall average of pump efficiency around 23%, relatively

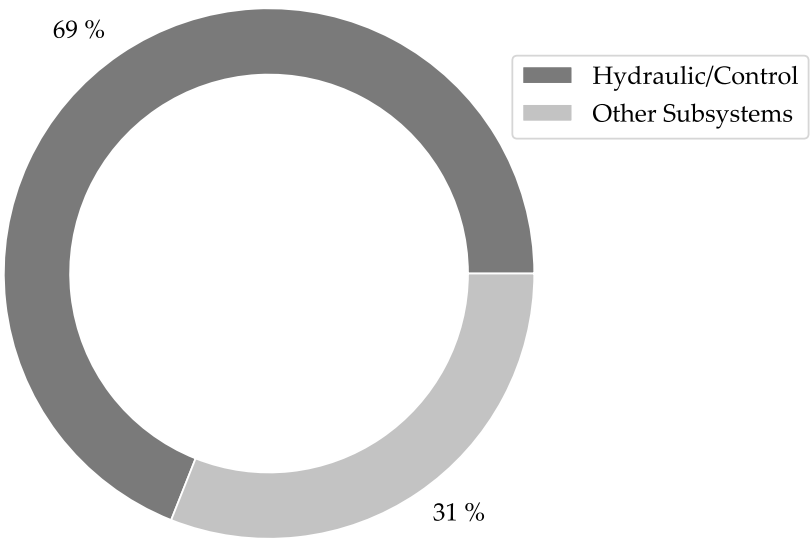

Figure 49 – Percentage of entropy generation of the magnetic prototype subsystems.

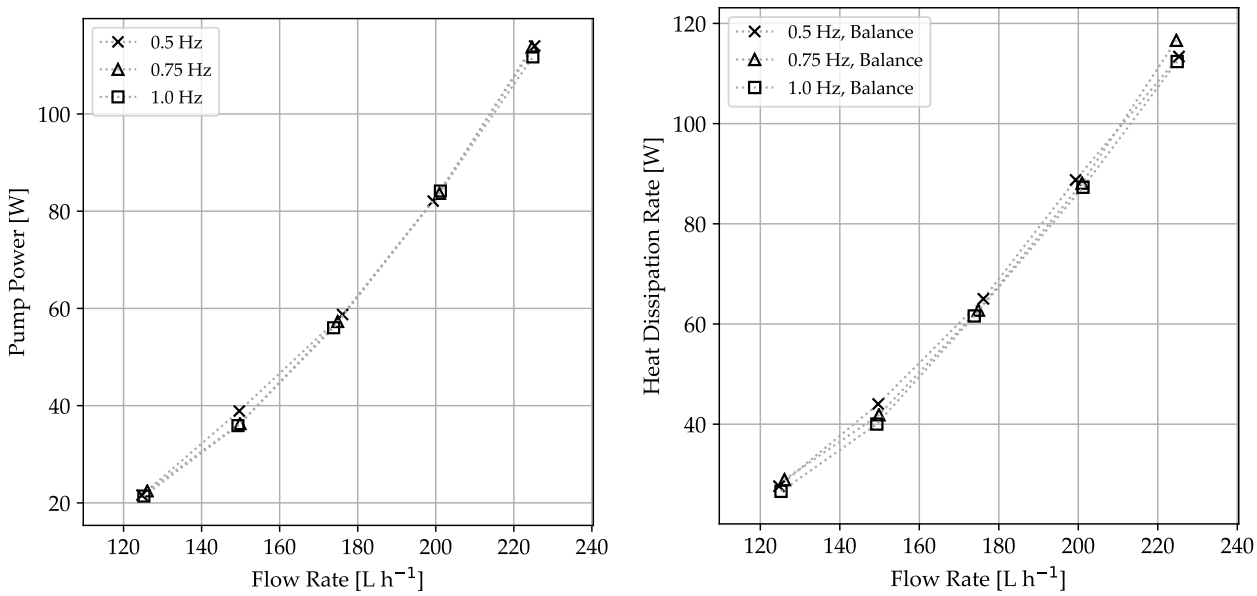

(a) (b)

Figure 50 – Results for the (a) power consumption of the pump and (b) heat dissipation of the pump to the fluid as a function of the volumetric flow rate for the three operating frequencies.

consistent with the catalogue information of an efficiency of 20%, as there is additional losses not considered in Eq. (4.1), confirming a very inefficient pump. Different from other components, the pump was not properly selected for the wine cooler prototype. The pump had been used in previous prototypes developed by the PoloMag team — which were not efficiency-oriented.

With a more efficient pumping system, properly selected for the levels of speed and flow rate applicable in the prototype, improvements in the the overall performance of the

magnetic wine cooler could be achieved. For instance, if the current pump was replaced by a pump with η_P = 40%[3], the *COP* and second-law efficiency at the best operating points would be, respectively, 0.55 and 2.3% for the F50V125 test and 0.33 and 1.6% for the F100V175 test. A more efficient pump would also decrease the need for a large overall thermal conductance heat exchanger on the hot side — currently supplying three fans, as the heat dissipation in the pump would be lower, and the power of the fans could be decreased. Thus, by improving only the pump, the number of fans would naturally be able to be decreased. Nevertheless, a lower heat dissipation by the pump would lead to higher cooling capacities, as the unnecessarily large heat dissipation contributes to the increase of the regenerator inlet temperature in the hot side — which deteriorates the magnetocaloric effect.

Additional improvements in the magnetic wine cooler prototype could also be achieved through the selection of more suitable magnetocaloric materials in the regenerator layers, so as to improve the magnetocaloric effect. Even though the magnetic wine cooler was designed to operate in ambient temperatures around 25ºC, the regenerator layers of Gd and Gd alloys have Curie temperatures of 17ºC, 10ºC and 4ºC (see Sec.3.2.1). With the designed level of ambient temperature, the temperatures in the hot side inlet of the regenerator are therefore higher than 25ºC, and thus the magnetocaloric effect is already poor in the initial stages of the regenerator. The Curie temperature of the layers were a limitation of the first version of the magnetic wine cooler prototype. Although the pure Gd can be alloyed with different elements to obtain positive effects, the alloys can only provide Curie temperatures lower than that of pure Gd, which limited the maximum Gd temperature of the regenerator to 17ºC. In order to assess the loss in the overall performance of the prototype due to the degradation of the MCE, a further test was carried out for the test condition F50V125 — according to the procedure of the performance tests, but for a ambient temperature of 19ºC. This ambient temperature was chosen due to recent studies that showed that higher cooling capacities can be obtained with a hot source temperature 2 K higher than the highest Curie temperature of the regenerator (LEI et al., 2015). Tab. 16 presents the comparison between the results of the F50V125 test with 19 and 25ºC of ambient temperature. With the benefit of being closer to the maximum Curie temperature of the regenerator, the magnetic prototype was able to reach a temperature span between ambient and cabinet almost 3ºC higher than the test for 25ºC, which provided a cooling capacity 5 W higher. Also, the *COP* was increased by 10% and the second-law efficiency by 40%.

Table 16 – Thermodynamic comparison between the F50V125 test for an ambient temperature of 19 and 25ºC.

Parameters	**Ambient temperature**	
	25ºC	19ºC
Temperature span [ºC]	11.7	14.5
Cooling capacity [W]	24.3	29.3
COP [ºC]	0.41	0.45
η_{2nd} [%]	1.7	2.4

[3] This efficiency value was considered for a comparative scenario as it was the double of the current efficiency and also a plausible value according to a research in different pump catalogues.

If the same assumption of a better pump with η_P = 40% was made for the test F50V125 with an enhanced magnetocaloric effect in the regenerators, the *COP* could be increased to 0.62 and the second-law efficiency to 3.3%.

A promising magnetocaloric material for near room temperature applications is the La-Fe-Si alloys (Lanthanum-Iron-Silicon). Figure 51 presents the ΔT_{ad} and Δs_{iso} for the Gd layers that were used in the AMR of the prototype and a simulation of what could be the layers of the AMR if La-Fe-Si alloys were employed instead. The properties of the La-Fe-Si alloys were obtained from Vieira et al. (2020). Although having a similar ΔT_{ad} in average compared to the Gd alloys, the La-Fe-Si alloys have higher Δs_{iso}, which physically is reflected in a higher cooling capacity. Another advantage of the La-Fe-Si alloys is that the Curie temperature can be varied in a temperature range from -73 to 67ºC, with the addition of different alloy materials (SMITH et al., 2012; TREVIZOLI, 2015; LEI et al., 2015; KITANOVSKI et al., 2015), which means that the layers can be adjusted much more than for Gd. With a change of the magnetocaloric material in the current prototype, higher cooling capacities could be achieved, leading to higher system temperature spans, *COP* and second-law efficiencies. Also, a more compact system could be attained, with a lower mass of magnetocaloric material and a smaller magnet, leading to lower power consumption of the pump and the system that drives the magnet — and, hence, to higher *COP* and second-law efficiencies.

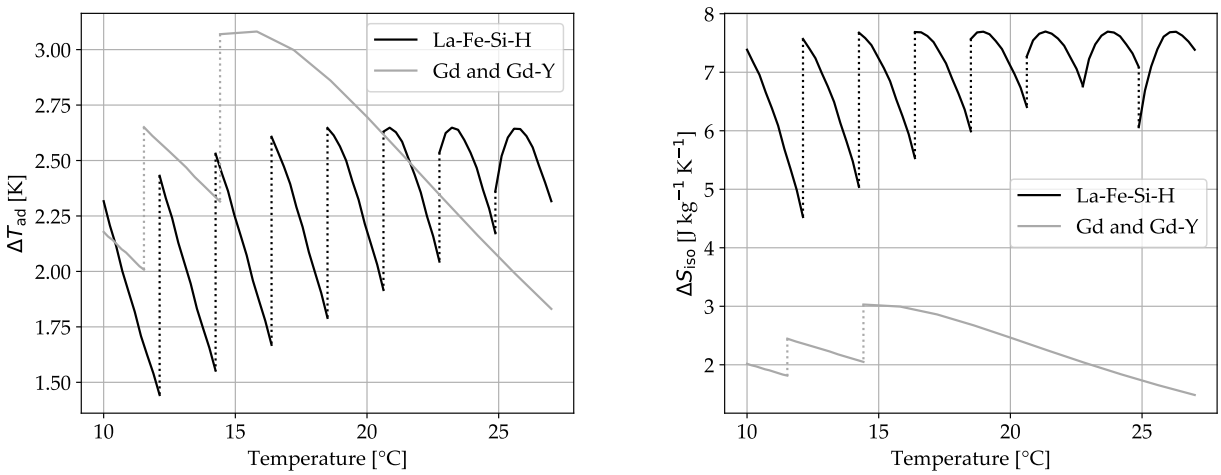

(a) (b)

Figure 51 – Comparison of the ΔT_{ad} and Δs_{iso} parameters of the prototype regenerator and the same regenerator simulated with La-Fe-Si alloys.

4.3 Performance Comparison

With the results of the characterization of the conventional and magnetic wine coolers, both cooling technologies were compared with respect to their performances when operating the same cabinet. In order to establish a reference for the comparison, the performance metrics were evaluated as a function of the steady-state cabinet temperature. The main

results for annual energy consumption, *COP* and second-law efficiency are presented with all test points of the performance tests for the magnetic prototype, together with the tests of the conventional wine cooler characterization. In a further analysis, the most suitable test point from the magnetic wine cooler tests is chosen for a more specific comparison with the conventional technology, considering an analysis of the *COP* — Carnot, internally ideal and actual, and second-law efficiency — external, internal and overall, as well as highlights of cooling capacity and pull down time, so as to define the gap between the two cooling technologies.

Figure 52 presents the annual energy consumption as a function of the cabinet temperature for the magnetic and the conventional wine coolers, with a highlight of the considered best operating points of the magnetic technology. For comparison purposes, the annual energy consumption of the conventional wine cooler was interpolated and extrapolated for the steady-state cabinet temperatures of 10.8 and 12.5ºC, respectively, so as to compare directly with the test points F50V125 and F100V175 of the magnetic prototype. For a cabinet temperature of 12.5ºC, the annual energy consumption of the magnetic wine cooler prototype and the conventional wine cooler were 505 kWh/year and 260 kWh/year, respectively, representing an increase of 94% in the annual energy consumption when operating with the magnetic technology. For a cabinet temperature of 10.8ºC, the increase of annual energy consumption when operating with the magnetic technology was even greater, around 340% higher than an operation with the vapor compression technology, being 1036 kWh/year for the magnetic wine cooler and 303 kWh/year for the conventional wine cooler. In an overall analysis, even the test points of the magnetic wine cooler with lower annual energy consumption are a lot higher than the most consuming operation point of the conventional wine cooler.

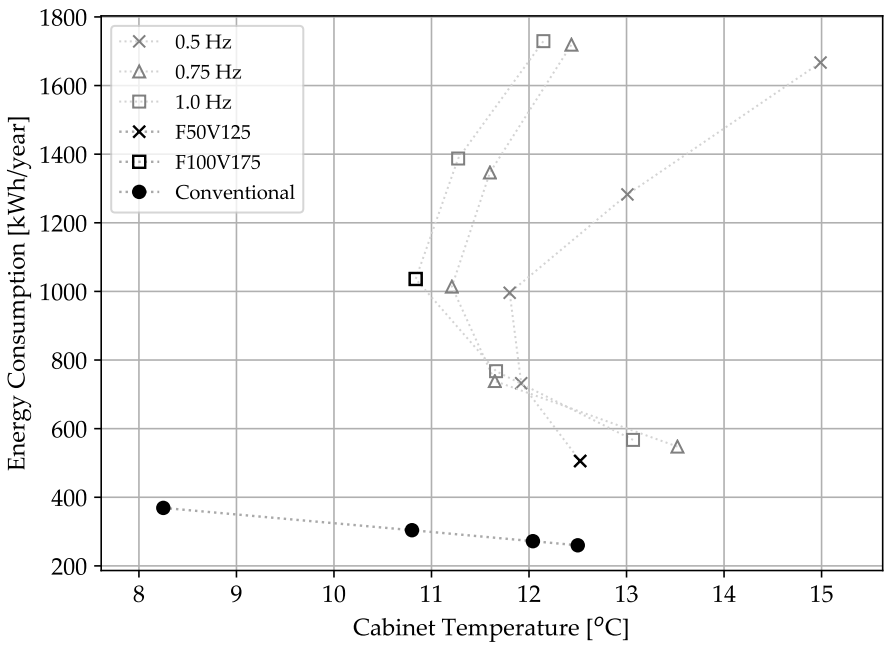

Figure 52 – Results of the annual energy consumption for the magnetic and conventional wine cooler as a function of the steady-state cabinet temperature.

Figure 53 presents the *COP* as a function of the cabinet temperature. The best *COP* of the

prototype was about 40% lower than the *COP* of the conventional wine cooler for a cabinet temperature of 12ºC, and yet provided a steady-state cabinet temperature 0.5ºC higher. Also, the cost of *COP* to lower the cabinet temperature from 12.5 to 10.8ºC in the magnetic prototype was heavily greater than the cost of *COP* to lower the cabinet temperature from 12.0 to 8.2ºC in the vapor compression wine cooler — the *COP* went from 0.41 to 0.23 in the magnetic wine cooler, representing a loss in the order of of 44%, while for the conventional wine cooler the *COP* went from 0.70 to 0.68, representing a loss of 3%. In an overall analysis, the *COP* results for the magnetic wine cooler are all in an inferior level in comparison with the conventional wine cooler.

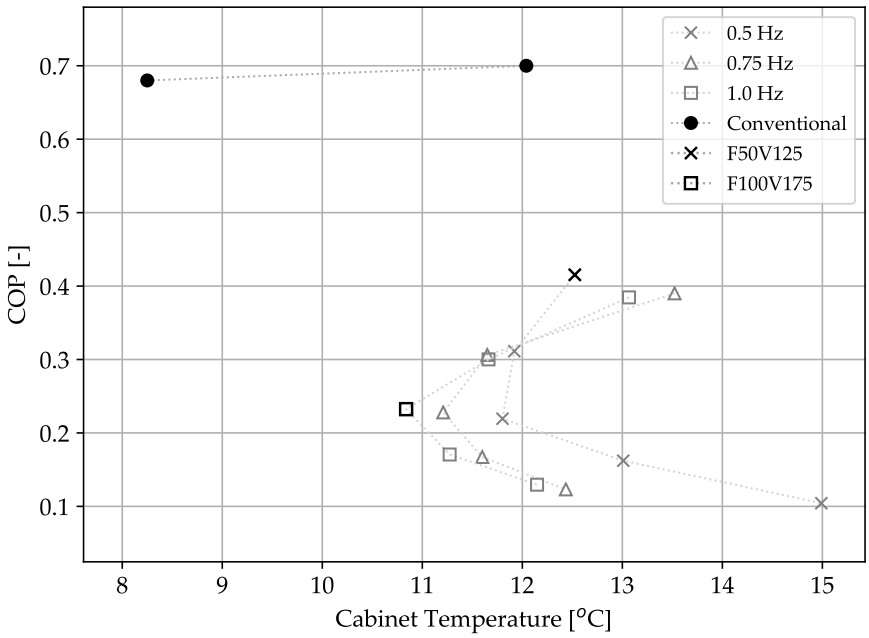

Figure 53 – Results of the coefficient of performance for the magnetic and conventional wine cooler as a function of the steady-state cabinet temperature.

Figure 54 presents the second-law efficiency as a function of the cabinet temperature. In a similar analysis, the second-law efficiency results for the magnetic wine cooler are also all in an inferior level regarding the conventional wine cooler results. The best second-law efficiency of the magnetic wine cooler, 1.7%, was about 46% lower than the second-law efficiency of the conventional wine cooler for a cabinet temperature of 12ºC, 3.1%. Although for lower cabinet temperatures the Carnot *COP* is also smaller, which in principle could lead the points more to the left of the magnetic wine cooler to be more efficient in terms of the second-law, the decrease of *COP* with the flow rate was way higher than the decrease of the Carnot *COP*. Thus, the second-law efficiencies of the prototype tests only experienced a decrease from the points of lowest volumetric flow rate, for the three operating frequencies evaluated.

As means to present a side-by-side comparison of both cooling technologies, the best operating point of the magnetic wine cooler in terms of performance, F50V125, was put to a more detailed comparison with the operating point of 12ºC of the conventional wine cooler.

Figure 55 (a) and (b) present the detailed analysis of *COP* and second-law efficiencies

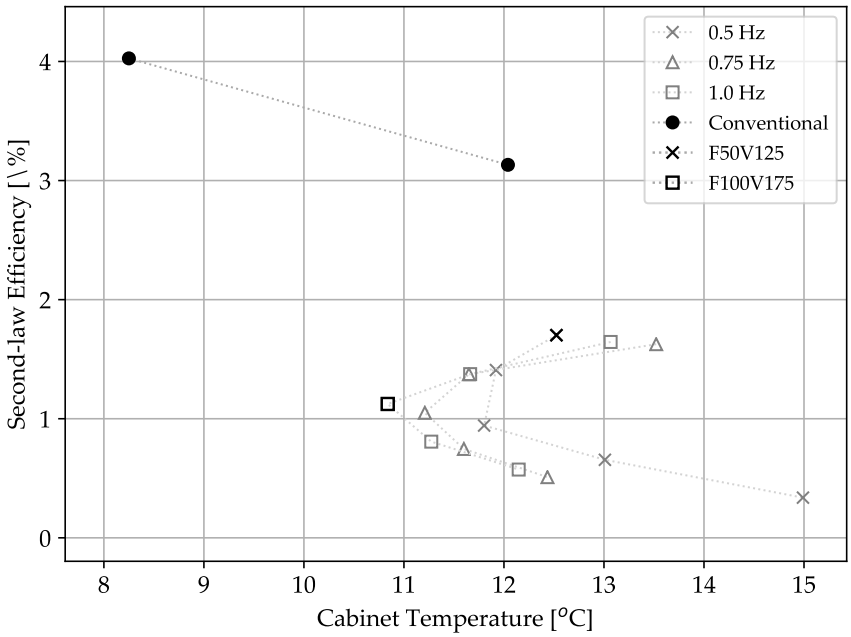

Figure 54 – Results of the second-law efficiency for the magnetic and conventional wine cooler as a function of the steady-state cabinet temperature.

for the magnetic and conventional wine cooler, for the two above mentioned test points. Although the actual *COP* of the magnetic wine cooler was about 40% lower than the actual *COP* of the conventional wine cooler, the internally ideal *COP* was more than 2 times higher than the internally ideal *COP* of the conventional. These results reveal how much greater are the internal irreversibilities and losses of the magnetic wine cooler when compared to the conventional. Indeed, this is confirmed in the results of internal efficiency. The conventional wine cooler was almost 4 times more efficient than the magnetic wine cooler when it comes to internal losses, elucidating that still there is a lot to be improved in magnetic refrigeration and its components. Nevertheless, these results also shows that there is a wider potential to improve the internal efficiency in the magnetic refrigeration than in the vapor compression refrigeration. As regards the external efficiency, the magnetic wine cooler was 2 times more efficient than the conventional wine cooler. This difference is mainly due to the fact that the magnetic wine cooler had heat exchangers with forced convection, while the conventional wine cooler had heat exchangers with natural convection. This result shows that the heat exchangers do not represent a weak point in the improvement of the magnetic technology.

In terms of cooling capacity, the conventional wine cooler provided 22.2 W to reach a steady-state cabinet temperature of 12.0ºC, while the magnetic wine cooler prototype provided 24.3 W to reach a steady-state cabinet temperature of 12.5ºC. That said, the magnetic wine cooler prototype required a higher cooling capacity to reach a cabinet temperature 0.5ºC higher.

The temperature pull down time of the F50V125 test was about 5 hours, almost 5 times higher than the temperature pull down time of the conventional wine cooler for a cabinet temperature of 12ºC, being about 1.1 hours. The pull down time of the magnetic wine cooler could be improved with the implementation of a control based on the speed of the magnet

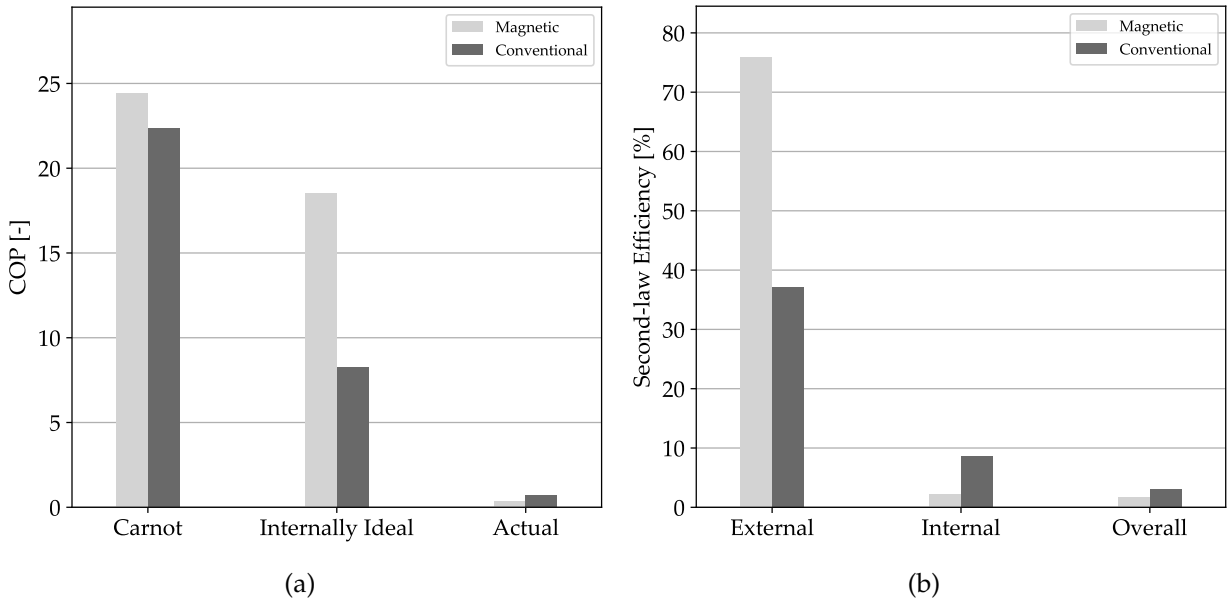

Figure 55 – Detailed results of (a) *COP* and (b) second-law efficiency for the magnetic and conventional wine cooler.

and the pump, by carrying out the pull down at different operation points — such as the F100V175 point or the best combination of flow rate and operating frequency that generates in the prototype the minimum pull down time, and then switching to the operation point F50V125.

Table 17 summarizes the side-by-side comparison of the main efficiency parameters, so as to assess more clearly the gap between magnetic and vapor compression cooling technologies when operating the same cabinet.

Table 17 – Summary of the results for the comparison of the conventional and magnetic wine cooler, for a steady-state cabinet temperature around 12ºC.

Parameters	**Cooling Technology**	
	Conventional	Magnetic
Average cabinet temperature [ºC]	12.0	12.5
Cooling capacity [W]	22.2	24.3
Energy Consumption [kWh/year]	272	505
COP [-]	0.70	0.41
Overall η_{2nd} [%]	3.1	1.7
Pull Down Time [h]	1.1	5.0

5 Conclusions

This work aimed at providing the first-in-literature performance comparison between magnetic and vapor compression cooling technologies, so as to establish the level of maturity of the former in light of the well-developed latter. For this purpose, both technologies were experimentally analyzed while operating over the same wine cooler cabinet. The vapor compression wine cooler was characterized in terms of performance by a selection of tests, based in several works that assessed performance metrics of vapor compression systems for comparison purposes. The magnetic wine cooler, designed by the PoloMag team, was first assembled and then tested so as to characterize the system behavior in range of input variables, as well as select the operating point (or points) to be compared to the vapor compression system system.

The vapor compression system was the Brastemp *Gourmand Dual Zone* BZB31AEBNA, marketed by Whirlpool S.A., which is divided into two internal compartments able to control individually the temperatures in the range of 8 to 18ºC. The wine cooler was instrumented with thermocouples and a wattmeter, to assess all the parameters to calculate the performance variables without altering the original conditions of the product from manufacturer. The product was characterized with temperature pull down, energy consumption and reverse heat leakage tests, for thermostat temperatures of 8 and 12ºC. The *UA* of the cabinet obtained through the RHL test was 1.74 W/K. The test with both the thermostats — from the upper and lower compartments, at 8ºC reached the periodic steady-state after a 1.4 hours of temperature pull down. When in periodic steady-state, the product maintained an average cabinet temperature of 8.2ºC, while providing a cooling capacity of 29.1 W and demanding an energy consumption of 369 kWh/year. The *COP* and second-law efficiency achieved were 0.68 and 4.0%, respectively. The test with both the thermostats at 12ºC reached the periodic steady-state after 1.1 hours of temperature pull down. When in periodic steady-state, the product maintained an average cabinet temperature of 12.0ºC, while providing a cooling capacity of 22.3 W and demanding an energy consumption of 272 kWh/year. The *COP* and second-law efficiency achieved were 0.70 and 3.1%, respectively. Both test conditions demanded an energy consumption higher that that allowed by the IEC 62552 (2015) standard for household appliances — 175 kWh/year, which was attributed to an oversized compressor.

A detailed analysis of the performance parameters was also carried out. The Carnot and internally ideal *COP* were higher for the 12ºC test, while the *COP* barely changed between the two test conditions. As a consequence, the 8ºC test was internally and overall more efficient — in terms of the second law, than the 12ºC test. The two tests presented a very similar external second-law efficiency, around 37.0%, an expected low value as the heat exchangers work by natural convection. The low external efficiencies could be also related to the oversized compressor, which was combined with undersized evaporators in order to compensate the extra capacity and maintain the wine quality.

The magnetic wine cooler prototype was assembled with the same cabinet from the

vapor compression system, coupled with a heat exchanger. The prototype was the one of the first to assemble a magnetic refrigeration system with a cabinet and real heat exchangers in the cold and the hot sides. To facilitate the flow management and control logic, the two compartments were unified into a single cabinet. The magnetic wine cooler was tested for different inputs of volumetric flow rate and operating frequency, which originated a combination of fifteen performance tests. The tests were evaluated first through performance maps.

The cooling capacity exhibited points of maximum for all three operating frequencies, due to a combination of effects such regenerator effectiveness, flow rate and inlet temperature in the regenerator hot side. The maximum cooling capacities were reached for a flow rate of 175 L/h for operating frequencies of 0.75 and 1.0 Hz and for a flow rate of 150 L/h for a frequency of 0.5 Hz. Reflecting the behavior of the cooling capacity, the steady-state cabinet temperature presented points of minimum for a flow rate of 175 L/h for all three operating frequencies. The discrepancy between the minimum steady-state cabinet temperature and maximum cooling capacity in the operating frequency of 0.5 Hz — the first for 175 L/h and the second for 150 L/h, is due to the high influence of the ambient temperature in the cabinet temperature. If the performance tests were carried out at the same exact ambient temperature, the test with flow rate of 150 L/h and operating frequency of 0.5 Hz would have also presented the minimum cabinet temperature. The maximum cooling capacity and minimum steady-state cabinet temperature were 27.3 W and 10.8ºC, respectively, reached in the F100V175 test.

The power consumption was evaluated as a whole and according to share for each component, namely the pump, the fans, the valves and the magnet. The power increased greatly with the flow rate, having tripled from the flow rate of 125 L/h to 225 L/h. As a consequence, the energy consumption was also greatly increased with the flow rate, reaching over 1700 kWh/year. Nevertheless, the minimum energy consumption was of the order of 505 kWh/year, much higher than that allowed by the IEC 62552 (2015) standard for household appliances — 175 kWh/year. In the single components analysis, it became clear that the main share of the power consumption was owed to the pump, contributing to around 50% of the total power for a flow rate of 125 L/h and around 81% for the flow rate of 225 L/h.

In terms of performance, the *COP* presented a continuous decrease behavior with the flow rate, for all three operating frequencies. Although the cooling capacity presented points of maximum, the increase of the power consumption with the flow rate was much more pronounced than the increase of cooling capacity in the first test points of all three operating frequencies. A similar trend was observed for the second-law efficiency, but for an operating frequency of 0.5 Hz the second-law efficiency was somewhat reduced at a higher rate for high flow rates, due to the increase of the ideal Carnot *COP* with the pronounced increase of the steady-state cabinet temperatures. The highest *COP* and second-law efficiency were 0.41 and 1.7%, reached in the F50V125 test. In a more detailed analysis of the performance variables, the internal second law efficiencies were very low and followed the pattern of the overall second-law efficiency, in highly decreasing with the flow rate. In contrast, the internally ideal *COP* were high, suggesting a broad potential for improvement in this regard.

The external second-law efficiencies were very high, on an average at a value around 75.0%, reflecting the use of heat exchangers with forced convection and also a good selection of the heat exchangers in the design phase of the prototype.

In an overall analysis, although the temperature and cooling capacity presented points of optimum, the performance metrics are higher for the lowest values of flow rate. As the point with best *COP* and best second-law efficiency was not the point with highest cooling capacity and lowest cabinet temperature, two tests were considered as best operating points, one in terms of performance and another terms of capacity. The test points were, respectively, the F50V125 and F100V175, and were selected for further analysis of temperature pull down time and influence of the cold fan power consumption. The pull down time was around 5 hours for the F50V125 test and 2.5 hours for the F100V175 test, when tested according to method 1 — with the cold fan being switched on after the temperature of the working fluid starts to stabilize. The F100V175 was then tested according method 2 — with the cold fan being switched on together with the beginning of the AMR/Magnet cycle, which has proven to be faster. The tests of the influence of the cold fan power consumption showed that the temperature of the cabinet tends to decrease with the decrease of the fan power, but with at the expense of increasing the temperature stratification inside the cabinet. Also, although the second-law efficiencies increased with the decrease of the fan power, due to the decrease of the Carnot *COP*, the *COP* barely changed and even decreased, as the cooling capacity is directly proportional to the fan power.

With both cooling technologies fully characterized, the comparison was first carried out for the results of energy consumption, *COP* and second-law efficiency, for all test points of both technologies. To establish the same basis for comparison, the results of the performance metrics were compared as a function of the cabinet temperature. The energy consumption results of the magnetic wine cooler were all higher than that of the conventional wine cooler, and the best case of the magnetic in terms of performance still presented an energy consumption 94% higher than the conventional for a similar cabinet temperature, both around 12ºC. The magnetic wine cooler was not able to reach cabinet temperatures below 10.8ºC, so a direct comparison with the 8ºC test of the conventional wine cooler could not be carried out, but it was clear that the energy cost to lower the cabinet temperature from 12.5ºC to 10.8ºC in the magnetic system was much higher than to lower from 12ºC to 8ºC in the conventional wine cooler.

The *COP* and second-law efficiency results of the magnetic wine cooler were all inferior than those of the conventional wine cooler. The best *COP* of the magnetic wine cooler was about 40% lower than the *COP* of the conventional wine cooler, around a cabinet temperature of 12ºC. The loss in performance to lower the cabinet temperature from 12.5ºC to 10.8ºC in the magnetic technology was of 44%, while to lower the cabinet temperature from 12ºC to 8ºC in the conventional technology the loss was 3%, barely representing a loss at all. The best second-law efficiency of the magnetic wine cooler was about 46% lower than the second-law efficiency of the conventional wine cooler, around a cabinet temperature of 12ºC. In contrast with the conventional wine cooler, which presented an increase of efficiency from the 12ºC to 8ºC tests, the efficiencies of the prototype only experienced a continuous decrease from

the point of smallest flow rate and operating frequency, as the decrease of *COP* was way higher than the decrease of the Carnot *COP*.

For a more detailed comparison, the best operating point in terms of performance of the magnetic wine cooler (F50V125 condition) was analyzed side-by-side with the 12ºC test of the conventional wine cooler. Despite presenting a 40% lower *COP*, the magnetic technology presented an internally ideal *COP* twice as high that of the conventional technology, mainly due to the smallest temperature difference between the working fluid in the heat exchangers with their respective environments compared with the evaporators and condenser in the vapor compression system. Yet, the internal efficiency of the magnetic technology was much lower than that of the conventional technology. That, combined with the higher internally ideal *COP*, indicates that there is room and a need for improvement in the magnetic technology in what regards internal losses. The external efficiency, however, was twice as high for the magnetic technology, again due to forced convection in the heat exchangers, indicating that the heat exchangers do not present as an obstacle for the magnetic technology improvement.

The cooling capacity generated by the magnetic wine cooler was higher, 24.3 W, while the conventional system was 22.2 W. This represents the need of a higher capacity to maintain the same cabinet temperature for the magnetic technology — and in this case 0.5ºC higher, than when operating with the conventional technology. The pull down time of the magnetic wine cooler was five times higher than for the conventional, 5 hours and 1.1 hours, respectively.

With the above results and comparison, a few outcomes can be appointed. The magnetic wine cooler is very sensitive towards changes in the ambient temperature, as the AMR and its layers were designed to work under specific conditions. A slight change in the hot reservoir temperature, either to higher or lower levels, can lead to a sharp decrease in the system performance. The pumping power has presented as an enormous contribution to the internal losses — in the very minimum around 50%, which led not only to very high energy consumption, but also to a very high cost in performance when decreasing the cabinet temperature in few degrees Celsius. Thus, the magnetic wine cooler was not able to reach temperatures below 10.8ºC, and paid a high price to do so. These are very limiting factors when considering the application of the technology at the present stage of the development, as the system needs to be made more robust enough to deal with normal ambient temperature variations.

When considering a cabinet temperature of around 12ºC, the wine cooler operated with a higher *COP* and second-law efficiency and required a lower energy consumption, cooling capacity and time to reach steady-state conditions while driven by the vapor compression system. When driven by the magnetic system, the wine cooler experienced a loss in all the performance variables evaluated. Few improvements in the magnetic wine cooler prototype could lead to similar performance outcomes. The selection of a more efficient pump and better solenoid valves could significantly decrease the power consumption and entropy generation in the system, which itself could improve the *COP* and second-law efficiency as well as decreasing the energy consumption. Also, a change in the magnetocaloric material

from Gd to La-Fe-Si alloys could enhance the cooling capacity and improve even more the *COP* and second-law efficiency, in addition to providing a more flexible selection of the regenerator layers. The pull down time could be improved with an implementation of a control based on the speed of the magnet and the pump, so as to find the best combination that generates the minimum pull down time until reached the temperature condition desired.

In light of those considerations, the magnetic cooling technology is still behind vapor compression in relation to performance metrics and at the present stage of the development, it is not yet sufficiently resilient or competitive to become a commercial product. However, there is a wide potential to reduce the internal irreversibilities, which could lead to similar performances in a side-by-side comparison. In order to advance magnetic refrigeration as a viable alternative to vapor compression, it is mandatory to bring into discussion the development of a more robust system in terms of ambient temperature, that is able to deal with transients during not only a daily weather, but also considering the difference in the temperature amplitude during different seasons and climate regions. Also, however are the current conclusions on the maturity level of magnetic refrigeration, it is worthwhile to periodically review the status of the thermodynamic performance of state-of-the-art prototypes, operating in realistic conditions of application and real cabinets, and compare them to similar vapor compression systems, so as to readdress the efforts to the weaker points that continue to maintain the gap from the magnetic to the vapor compression technology.

5.1 Recommendations for future works

Envisioning the points of improvement provided in this thesis and engaged with an optimization of the current magnetic wine cooler prototype, the following future works are suggested:

- Design new regenerators for the prototype with La-Fe-Si alloys, to select a more suitable set of layers to operate near room temperature, and consider the transient of temperature between winter and summer in a climate class N, to assess the feasibility of a more robust AMR in terms of ambient temperature and to compare the magnetic wine cooler with the conventional in different seasons;

- Select a more efficient pump, sized for the levels of speed and flow rate of the prototype, and more efficient solenoid valves, to assess the improvement on the internal irreversibilities and in the performance variables and readdress new improvement points;

- Carry out a study on the resilience of the magnetic system when submitted to disruptive conditions in equilibrium, such as door openings, wine bottle load and sudden changes in the ambient temperature, and design a PID-driven control for the prototype, so as to optimize the system for time, during conditions of temperature pull down, and for performance, during conditions of steady-state operation;

- Carry out an analysis on the entropy generation of the single components and subsystems of the magnetic wine cooler prototype in a more accurate approach, by characterizing the heat exchangers and the fans in wind tunnels and instrumenting the inlet and outlet of every component — either main or auxiliary, with thermocouples and pressure transducers, in the working fluid flow, air flow or in the magnetocaloric material, when applicable, so as to isolate the components from the tubing and assess the entropy generation of each component and each subsystem, readdressing the knowledge on the most contributive elements to the system inefficiency.

Bibliography

BAHL, C. R. H.; NIELSEN, K. K. The effect of demagnetization on the magnetocaloric properties of gadolinium. *Journal of Applied Physics*, v. 105, 2009.

BARCLAY, J.; STEYERT, W. Active Magnetic Regenerator. *US-Patent 4332135*, 1982.

BEZ, H.; NAKASHIMA, A. T.; LANG, G.; LOZANO, J. A.; BARBOSA, J. R. Numerical simulations and experimental tests of Gd-Y multi-layered active magnetic regenerators. In: *Proceedings in Eighth IIR International Conference on Caloric Cooling, Thermag VIII*. Darmstadt, Germany: [s.n.], 2018.

BEZ, H. N.; NAKASHIMA, A. T.; LANG, G. B.; LIMA, B. S. de; MACHADO, A. J.; LOZANO, J. A.; BARBOSA, J. R. Performance assessment and layer fraction optimization of Gd-Y multilayer regenerators for near room-temperature magnetic cooling. *International Journal of Air-Conditioning and Refrigeration*, World Scientific, v. 28, n. 3, 9 2020. ISSN 20101333.

BOENG, J. *Uma Metodologia para a seleção do par tubo capilar/carga de refrigerante que maximiza o desempenho de refrigeradores domésticos*. Master Thesis — Universidade Federal de Santa Catarina, 2012.

BROWN, G. V. Magnetic heat pumping near room temperature. *Journal of Applied Physics*, v. 47, 1976.

BROWN, J. S.; DOMANSKI, P. A. Review of Alternative Cooling Technologies. *Applied Thermal Engineering*, v. 64, p. 252–262, 2014.

CALOMENO, R. Modelagem Matemática do Gabinete e Trocadores de Calor de uma Adega Doméstica Visando à Operação por um Refrigerador Magnético. Master Thesis - Universidade Federal de Santa Catarina, 2018.

CALOMENO, R.; LOZANO, J. A.; TREVIZOLI, P. V.; BARBOSA, J. R. Influence of heat exchangers thermal conductance on the thermodynamic performance of a magnetic refrigerator. In: *Proceedings in Seventh IIF-IIR International Conference on Magnetic Refrigeration at Room Temperature*. Turin, Italy: [s.n.], 2016.

CAPOVILLA, M. S.; LOZANO, J. A.; TREVIZOLI, P. V.; BARBOSA, J. R. Performance Evaluation of a Magnetic Refrigeration System. *Science and Technology for the Built Environment*, v. 22, p. 534–543, 2016.

CARARO, J. Análise de Regeneradores Magnético-Ativos do Tipo Multicamadas. Master Thesis - Universidade Federal de Santa Catarina, 2016.

CARDOSO, P. O. Um Sistema à Base de Eletroválvulas para o Gerenciamento Hidráulico de Regeneradores Magnético-Ativos. Master Thesis - Universidade Federal de Santa Catarina, 2018.

CHURCHILL, S.; CHU, H. Correlating equations for laminar and turbulent free convection from a horizontal cylinder. *International Journal of Heat and Mass Transfer*, v. 18, p. 1049, 1975.

DUTRA, S. Avaliação de uma adega doméstica sob a perspectiva de duas tecnologias de refrigeração: compressão mecânica de vapores e refrigeração magnética. Undergraduate Thesis - Universidade Federal de Santa Catarina, 2018.

DUTRA, S.; NAKASHIMA, A. T.; HOFFMANN, G.; LOZANO, J. A.; BARBOSA, J. R. Using electrovalves as a flow distribution system for an active magnetic regenerator. In: *Proceedings in the 24th ABCM International Congress of Mechanical Engineering*. [S.l.: s.n.], 2017.

ENGELBRECHT, K.; BAHL, C. R. Evaluating the effect of magnetocaloric properties on magnetic refrigeration performance. *Journal of Applied Physics*, American Institute of Physics Inc., v. 108, n. 12, 12 2010. ISSN 00218979.

ENGELBRECHT, K.; ERIKSEN, D.; BAHL, C. R. H.; BJØRK, R.; GEYTI, J.; LOZANO, J. A.; NIELSEN, K. K.; SAXILD, F.; SMITH, A.; PRYDS, N. Experimental results for a novel rotary active magnetic regenerator. *International Journal of Refrigeration*, v. 35, p. 1498–1505, 2012.

ERIKSEN, D.; ENGELBRECHT, K.; BAHL, C. R. H.; BJØRK, R.; NIELSEN, K. K.; INSINGA, A. R.; PRYDS, N. Design and experimental tests of a rotary active magnetic regenerator prototype. *International Journal of Refrigeration*, v. 58, p. 14–21, 2015.

ESPÍNDOLA, R. da S. *Análise teórico-experimental do desempenho de refrigeradores domésticos com condensadores do tipo Hot-Wall*. Master Thesis — Universidade Federal de Santa Catarina, 2017.

FORTKAMP, F. P. Integrated Design of theMagnet-Regenerator Assembly for aMagnetic Refrigerator. In: . PhD Thesis - Universidade Federal de Santa Catarina: [s.n.], 2019.

FORTKAMP, F. P.; LANG, G.; PEIXER, G.; LOZANO, J. A.; BARBOSA, J. R. Integrated design of a magnetic circuit and an active magnetic regenerator for a 100-W compact device. In: *Proceedings in Eighth IIR International Conference on Caloric Cooling, Thermag VIII*. Darmstadt, Germany: [s.n.], 2018.

FORTKAMP, F. P.; LANG, G. B.; LOZANO, J. A.; BARBOSA, J. Design trade-offs for an active magnetic regenerator device. *Applied Thermal Engineering*, Elsevier Ltd, v. 165, 1 2020. ISSN 13594311.

FORTKAMP, F. P.; LOZANO, J. A.; BARBOSA, J. R. Analytical solution of concentric two-pole Halbach cylinders as a preliminary design tool for magnetic refrigeration systems. *Journal of Magnetism and Magnetic Materials*, Elsevier B.V., v. 444, p. 87–97, 12 2017. ISSN 03048853.

GONÇALVES, J. M. et al. Estudo experimental de um refrigerador *No-Frost*. parte i: Transferência de calor através das paredes. In: *Primeiro Congresso Nacional de Engenharia Mecânica*. Natal-RN, Brasil: [s.n.], 2000.

GOSNEY, W. B. *Principles of Refrigeration*. [S.l.]: Cambridge University Press, 1982.

HERMES, C. J.; BARBOSA, J. R. Thermodynamic comparison of Peltier, Stirling, and vapor compression portable coolers. *Applied Energy*, v. 91, n. 1, p. 51–58, 2012.

HERMES, C. J.; MELO, C.; KNABBEN, F. T. Alternative test method to assess the energy performance of frost-free refrigerating appliances. *Applied Thermal Engineering*, Elsevier, v. 50, n. 1, p. 1029–1034, 2013.

HERMES, C. J.; MELO, C.; KNABBEN, F. T.; GONÇALVES, J. M. Prediction of the energy consumption of household refrigerators and freezers via steady-state simulation. *Applied Energy*, v. 86, n. 7-8, p. 1311–1319, 2009.

HERMES, C. J. L. *Desenvolvimento de modelos matemáticos para simulação numérica de refrigeradores domésticos em regime transiente*. Master Thesis — Universidade Federal de Santa Catarina, 2000.

HERMES, C. J. L. *Uma metodologia para a simulação transiente de refrigeradores domésticos*. PhD Thesis — Universidade Federal de Santa Catarina, 2006.

HINKEL, L. Desenvolvimento do projeto mecânico conceitual e dimensionamento de elementos estruturais de um refrigerador magnético compacto. In: . Trabalho de Conclusão de Curso - Instituto Federal de Educação, Ciência e Tecnologia de Santa Catarina: [s.n.], 2018.

HOFFMANN, G. *Desenvolvimento e avaliação experimental de estratégias de controle para sistemas de refrigeração magnética*. Master Thesis *(Ongoing)* — Universidade Federal de Santa Catarina, 2020.

HOFFMANN, G.; DUTRA, S.; CARDOSO, P. O.; NAKASHIMA, A. T.; LOZANO, J. A.; BARBOSA, J. R. Actuation and Control of Electric Valves for a Magnetic Refrigerator. In: *Proceedings in the 24th ABCM International Congress of Mechanical Engineering*. [S.l.: s.n.], 2017.

IEC 62552. Household refrigerating appliances - characteristics and test methods - part 1: General requirements. In: *International Electrotechnical Commission*. Geneva: [s.n.], 2015.

IIR. *The impact of the refrigeration sector on climate change.* 35th Informatory Note on Refrigeration Technologies. International Institute of Refrigeration. Technical Report. Paris, France, 2019.

INCROPERA, F. P.; DEWITT, D. P.; BERGMAN, T. L.; LAVINE, A. S. *Fundamentals of heat and mass transfer*. 6. ed. [S.l.]: LTC, 2008.

ISO 15502. Household refrigerating appliances - characteristics and test methods. In: *International Organization for Standardization*. Geneva: [s.n.], 2005.

ISO 8561. Household frost-free refrigerating appliances - refrigerators, refrigerators-freezers, frozen food storage cabinets and food freezers cooled by internal forced air circulation - characteristics and test methods. In: *International Organization for Standardization*. Geneva, Switzerland: [s.n.], 1995.

JACOBS, S.; AURINGER, J.; BOEDER, A.; CHELL, J.; KOMOROWSKI, L.; LEONARD, J.; RUSSEK, S.; ZIMM, C. The performance of a large-scale rotary magnetic refrigerator. *International Journal of Refrigeration*, v. 37, p. 84–91, 2014.

KITANOVSKI, A. *Energy Applications of Magnetocaloric Materials*. [S.l.]: Wiley-VCH Verlag, 2020.

KITANOVSKI, A.; PLAZNIK, U.; TUŠEK, J.; POREDOŠ, A. New thermodynamic cycles for magnetic refrigeration. *International Journal of Refrigeration*, v. 37, p. 28–35, 2014.

KITANOVSKI, A.; TUSEK, J.; TOMC, U.; PLAZNIK, U.; OZBOLT, M.; POREDOS, A. *Magnetocaloric Energy Conversion: From Theory to Applications*. [S.l.]: Springer International Publishing, 2015.

LANG, G. *Development of an Active Magnetic Regenerator Model in Python using the Finite Volume Method*. Undergraduate Thesis (Mechanical Engineering Department) — Universidade Federal de Santa Catarina, 2018.

LEI, T. *Modeling of active magnetic regenerators and experimental investigation of passive regenerators with oscillating flow*. Tese (Doutorado) — Technical University of Denmark, 2016.

LEI, T.; NIELSEN, K. K.; ENGELBRECHT, K.; BAHL, C. R.; BEZ, H. N.; VEJE, C. T. Sensitivity study of multi-layer active magnetic regenerators using first order magnetocaloric material La(Fe,Mn,Si)13Hy. *Journal of Applied Physics*, American Institute of Physics Inc., v. 118, n. 1, 7 2015. ISSN 10897550.

LOZANO, J. *Design of a rotary magnetic refrigerator*. Tese (Doutorado) — Universidade Federal de Santa Catarina, 2015.

LOZANO, J. A.; CAPOVILLA, M. S.; TREVIZOLI, P. V.; ENGELBRECHT, K.; BAHL, C. R. H.; JR., J. R. B. Development of a novel rotary magnetic refrigerator. *International Journal of Refrigeration*, v. 68, p. 187–197, 2016. ISSN 0140-7007.

LYUBINA, J. *Magnetocaloric materials for energy efficient cooling*. [S.l.]: Institute of Physics Publishing, 2017.

MARCON, A. S. A. *Otimização do desempenho de um refrigerador doméstico do tipo built-in de acordo com a norma global de consumo de energia*. Trabalho de Curso (Graduação em Engenharia Mecânica) — Universidade Federal de Santa Catarina, 2017.

NAKASHIMA, A. T.; DUTRA, S.; HOFFMANN, G.; LOZANO, J. A.; BARBOSA, J. R. Performance Assessment of Solenoid Valves as Flow Distributors for an Active Magnetic Regenerator. In: *Proceedings in Eighth IIR International Conference on Caloric Cooling, Thermag VIII*. Darmstadt, Germany: [s.n.], 2018.

NAKASHIMA, A. T.; DUTRA, S. L.; TREVIZOLI, P. V.; BARBOSA, J. R. Influence of the flow rate waveform and mass imbalance on the performance of active magnetic regenerators. Part II: Numerical simulation. *International Journal of Refrigeration*, v. 93, p. 159–168, 2018.

NAKASHIMA, A. T. D.; FORTKAMP, F. P.; SÁ, N. M. D.; SANTOS, V. M. A. D.; HOFFMANN, G.; PEIXER, G. F.; DUTRA, S. L.; RIBEIRO, M. C.; LOZANO, J. A.; BARBOSA, J. R. A Magnetic Wine Cooler Prototype. *International Journal of Refrigeration*, 2020. In press.

NELLIS, G.; KLEIN, S. *Heat transfer*. [S.l.]: Cambridge University Press, 2009. 1107 p.

NIELSEN, K. K.; BAHL, C. .; SMITH, A. .; ENGELBRECHT, K. .; OLSEN, U. L.; PRYDS, N. The influence of non-magnetocaloric properties on the AMR performance. In: *Proceedings of the fifth IIF-IIR International Conference on Magnetic Refrigeration at Room Temperature*. [S.l.: s.n.], 2012.

OLIVEIRA, M. S. Modelo para o Lean Product Development com o uso da Abordagem Toyota Kata Aplicado no Desenvolvimento De Produto Inovador. Master Thesis - Universidade Federal de Santa Catarina, 2017.

PEIXER, G.; CALOMENO, R.; LANG, G.; LOZANO, J. A.; JR., J. R. B. Integrated design of active magnetic regenerators and heat exchangers for magnetic refrigerators. In: *Proceedings in Eighth IIR International Conference on Caloric Cooling, Thermag VIII*. Darmstadt, Germany: [s.n.], 2018.

PEIXER, G. F. *Thermodynamic design of a magnetic cooling system for air-conditioning applications*. Master Thesis — Universidade Federal de Santa Catarina, 2020.

PEIXER, G. F.; DUTRA, S. L.; Sá, R. S. C. Natália M. de; LANG, G. B.; LOZANO, J. A.; BARBOSA JR., J. R. Influence of heat exchanger design on the thermal performance of a domestic wine cooler driven by a magnetic refrigeration system. *Annals of the Brazilian Academy of Sciences*, 2020. Manuscript accepted for publication.

QIAN, S.; NASUTA, D.; RHOADS, A.; WANG, Y. Not-in-kind cooling technologies : A quantitative comparison of refrigerants and system performance Technologies de refroidissement alternatives : une comparaison quantitative des frigorigènes et de la performance du système. *International Journal of Refrigeration*, v. 62, p. 177–192, 2016.

ROWE, A.; TURA, A.; DIKEOS, J.; CHAHINE, R. Experimental studies of near room temperature magnetic refrigeration. In: *Proceedings in 1st International Conference on Magnetic Refrigeration at Room Temperature*. Montreux, SWI: [s.n.], 2005.

SANTOS, V. Adaptação dos Sistemas Hidráulico e de Acionamento de um Protótipo de Refrigeração Magnética. Undergraduate Thesis - Instituto Federal de Educação, Ciência e Tecnologia de Santa Catarina, 2018.

SHAH, R. K.; SEKULIĆ, D. P. *Fundamental of Heat Exchanger Design*. Hoboken, New Jersey: John Willey & Sons, Inc, 2003. 941 p.

SMITH, A. Who discovered the magnetocaloric effect? Warburg, Weiss, and the connection between magnetism and heat. *European Physical Journal H*, v. 38, n. 4, p. 507–517, 9 2013. ISSN 21026459.

SMITH, A.; BAHL, C. R. H.; BJØRK, R.; ENGELBRECHT, K.; NIELSEN, K. K.; PRYDS, N. Materials challenges for high performance magnetocaloric refrigeration devices. *Advanced Energy Materials*, v. 2, p. 1288–1318, 2012.

TEYBER, R.; TREVIZOLI, P. V.; CHRISTIAANSE, T. V.; GOVINDAPPA, P.; NIKNIA, I.; ROWE, A. Experimental Evaluation of Two-material Active Magnetic Regenerators. In: *Proceedings in Seventh IIF-IIR International Conference on Magnetic Refrigeration at Room Temperature*. Turin, Italy: [s.n.], 2016.

THIESSEN, S. Caracterização experimental de gabinetes refrigerados isolados com painéis de vácuo. Master thesis - Universidade Federal de Santa Catarina, 2015.

TISHIN, A. M.; SPICHKIN, Y. I. The magnetocaloric effect and its applications. *IoP Institute of Physics Puclishing*, 2003.

TREVIZOLI, P.; BARBOSA, J. Overview on magnetic refrigeration. In: *Reference Module in Materials Science and Materials Engineering*. [S.l.]: Elsevier, 2020.

TREVIZOLI, P. V. *Development of thermal regenerators for magnetic cooling applications*. PhD Thesis — Universidade Federal de Santa Catarina, 2015.

TREVIZOLI, P. V.; BARBOSA, J. R.; TURA, A.; ARNOLD, D.; ROWE, A. Modeling of thermomagnetic phenomena in active magnetocaloric regenerators. *Journal of Thermal Science and Engineering Applications*, American Society of Mechanical Engineers (ASME), v. 6, n. 3, 9 2014. ISSN 19485093.

TREVIZOLI, P. V.; NAKASHIMA, A. T.; PEIXER, G. F.; BARBOSA, J. R. Performance evaluation of an active magnetic regenerator for cooling applications part I: Experimental analysis and thermodynamic performance. *International Journal of Refrigeration*, v. 72, p. 192–205, 2016.

TREVIZOLI, P. V.; OLIVEIRA, P. A.; CANESIN, F. C.; JR., J. R. B.; FERREIRA, R. T. S. Assessment of demagnetization phenomena in the performance of an active magnetic regenerator. *Internacional Journal of Refrigeration*, v. 35, p. 1043–1054, 2012.

TURA, A.; ROWE, A. Permanent magnet magnetic refrigerator design and experimental characterization. *International Journal of Refrigeration*, v. 34, n. 3, p. 628–639, 5 2011. ISSN 01407007.

URBAIN, G.; WEISS, P.; TROMBE, F. Un nouveau métal ferromagnétique, le gadolinium. *Comptes Rendus*, v. 200, p. 2132–2134, 1935.

VIEIRA, B. P.; BEZ, H. N.; KUEPFERLING, M.; ROSA, M. A.; SCHAFER, D.; CID, C. C. P.; VIEYRA, H. A.; BASSO, V.; LOZANO, J. A.; BARBOSA, J. R. Magnetocaloric properties of spheroidal La(Fe,Mn,Si)13Hy granules and their performance in epoxy-bonded active magnetic regenerators. *Applied Thermal Engineering*, Elsevier Ltd, v. 183, 1 2020. ISSN 13594311.

APPENDIX A – Uncertainty Analysis

This appendix presents the uncertainty analysis of the characterization tests for both the conventional and the magnetic wine cooler, based on the works of Boeng (2012) and Thiessen (2015).

A.1 Theoretical Definitions

A parameter x can be defined as the mean of the experimental values of its sampling, $\overline{x}$, and is calculated for n measurements as:

$$\overline{x} = \frac{1}{n}\sum_{\mathrm{i}=1}^{\mathrm{n}} x_{\mathrm{i}} \tag{A.1}$$

The estimate of the standard deviation of the parent population for the measurements of x, SD_{x}, is calculated as:

$$SD_{\mathrm{x}} = \sqrt{\frac{1}{n-1}\sum_{\mathrm{i}=1}^{\mathrm{n}}(x_{\mathrm{i}} - \overline{x})^2} \tag{A.2}$$

The parameter x is influenced by two error sources: random and systematic. The systematic random uncertainty (u_0), or type A, is owed to the scatter of the measurement values during the measurement period, while the systematic standard uncertainty, or type B (u_{s}), is owed to the errors inherent to the measuring system. The combined standard uncertainty for a parameter x is obtained as the combination of the elemental standard uncertainties, as:

$$u_{\mathrm{x}}^2 = u_0^2 + u_{\mathrm{s}}^2 \tag{A.3}$$

Since the parameters are affected by two (or more) independent error sources and considering a normal distribution of the error, the expanded uncertainties are calculated as:

$$U = k_{\mathrm{st}}\, u_{\mathrm{x}}^2 \rightarrow U_{98\%} = 2.32\, u_{\mathrm{x}}^2 \tag{A.4}$$

where k_{st} is the coefficient of Student for a 98% confidence interval. The type A uncertainty was divided into two categories, for the direct measured variables and for the the indirect measured variables. When a variable is direct measured, the random uncertainty is calculated by two forms, one for parameters with fixed values in time and other considering parameters that vary on time due to physical phenomena. If the parameter vary along the sampling time, the random uncertainty is simply equal to SD. If the parameter is fixed in time, the random uncertainty is calculated as:

$$u_0 = \frac{SD_{\mathrm{x}}}{\sqrt{n}} \tag{A.5}$$

When a variable indirect measured — obtained by a combination of direct variables, the random uncertainty can be derived from the general expression of the uncertainty propagation, as:

$$y = f(x_1, x_2, ..., x_n) \rightarrow u_0(y) = \sqrt{\frac{1}{n-1}\sum_{i=1}^{n}\left(\frac{\partial y}{\partial x_i}u(x_i)\right)^2} \tag{A.6}$$

A.2 Uncertainties of the Conventional Wine Cooler Tests

The direct measured parameters of the conventional characterization tests are presented in Tab. 18.

Table 18 – Direct measured parameters of the conventional characterization tests.

Parameter	Unit System
Product power	[W]
Upper compartment temperatures *(superior and bottom)*	[°C]
Lower compartment temperatures *(superior, middle and bottom)*	[°C]
Evaporator inlet temperatures *(upper and lower compartments)*	[°C]
Evaporator outlet temperatures *(upper and lower compartments)*	[°C]
Condenser inlet temperature	[°C]
Condenser outlet temperature	[°C]

As during the energy consumption tests the wine cooler operates in periodic steady-state, the direct measured parameters are not fixed in time, varying due to the on-off regime of the compressor. Thus, the type A uncertainties of these parameters should be calculated considering only the SD. However, as the interest is this parameters are as effective values — an analogue to the effective voltage in an AC electric circuit, the type A uncertainties were calculated in a different approach. The energy consumption tests were carried out in an 5 hour interval, for the two test points of the conventional wine cooler. This interval was divided into 5 intervals of 1 hour, for the evaluation of the average parameters in each interval. Taking the power consumption of the compressor as an example, the average value was calculated for each hour of an energy consumption test, totalling 5 average values for the entire test period (or $n = 5$). Then, the type A uncertainty was calculated considering the power consumption as a fixed parameter in time — in 1 hour of test, and considering Eq. A.5. Thus, the uncertainty can be interpreted as the variation that can be expected when evaluating the average power consumption of the compressor in an 1 hour interval of a periodic steady-state test. This approach was extended to all parameters measured during the energy consumption tests. For the RHL tests, the direct measured parameters were all in steady-state condition during sampling time, and therefore the type A uncertainties were calculated simply by Eq. A.5.

The indirect measured parameters of the conventional characterization tests are presented in Tab. 19.

Table 19 – Indirect measured parameters of the conventional characterization tests.

Parameter	Unit System
UA	[W/K]
Energy consumption	[kWh/year]
Average cabinet temperature	[ºC]
Average ambient temperature	[ºC]
Cooling capacity	[W]
COP	[-]
Second-law efficiency	[%]

The type B uncertainties of the conventional characterization tests were only due to the thermocouples and the wattmeter, and are presented in Tab. 20.

Table 20 – Type B uncertainties of the conventional wine cooler tests.

Parameter	**Uncertainty**
Thermocouples	0.2 ºC
Wattmeter	0.5 W

The expanded uncertainties were calculated as described in the previous section, as a combination of type A and B uncertainties, for the two test points of 8 and 12ºC. The energy consumption tests were acquired over a 5-hour sampling time and the RHL tests over a 5-minute sampling time, both with a sampling frequency of 0.1 Hz. The maximum expanded uncertainties of the two tests are presented in Tab. 21.

Table 21 – Maximum expanded uncertainties associated with the experimentally determined variables (98% confidence interval).

Parameters	**Uncertainty**
UA [W/ºC]	0.08
Energy consumption [kWh/year]	46
Average cabinet temperature [ºC]	0.1
Average ambient temperature [ºC]	0.1
Average evaporator temperature [ºC]	0.8
Average condenser temperature [ºC]	1.0
Cooling capacity [W]	1.2
Coefficient of performance [-]	0.1
Second-law efficiency [%]	0.9

A.3 Uncertainties of the Magnetic Wine Cooler Tests

The direct measured parameters of the magnetic characterization tests are presented in Tab. 22. All parameters were in steady-state condition during the sampling time, and therefore the type A uncertainties were calculated by Eq. A.5.

Table 22 – Direct measured parameters of the magnetic characterization tests.

Parameter	Unit System
Volumetric flow rate	[L/h]
Pressure	[bar]
Torque	[Nm]
Power of the fans	[W]
Power of the valves	[W]
Pump inlet temperature	[ºC]
Pump outlet temperature	[ºC]
HHEX inlet temperature	[ºC]
HHEX outlet temperature	[ºC]
CHEX intlet temperature	[ºC]
CHEX outlet temperature	[ºC]
Cabinet temperatures *(superior, middle and bottom)*	[ºC]
Ambient temperatures *(left, front and right)*	[ºC]

The indirect measured parameters of the magnetic characterization tests are presented in Tab. 23.

Table 23 – Indirect measured parameters of the magnetic characterization tests.

Parameter	Unit System
Power of the pump	[W]
Power of the magnet motor	[W]
Total power	[W]
Energy consumption	[kWh/year]
Average cabinet temperature	[ºC]
Average ambient temperature	[ºC]
Cooling capacity	[W]
COP	[-]
Second-law efficiency	[%]

The type B uncertainties of the magnetic characterization are presented in Tab. 24. The thermocouples and the pressure transducers uncertainties are the maximum uncertainties obtained during the calibration of those sensors, carried out internally in the Polo laboratory. The flow meter uncertainty was also obtained with calibration, with a Coriolis flow meter as reference (U = 10%).

Table 24 – Type B uncertainties of the magnetic wine cooler tests.

Parameter	**Uncertainty**
Flow meter	11 L/h
Thermocouples	0.1 ºC
Pressure transducers	0.5 bar
Torquimeter	0.5%
Wattmeter	0.3 W

The expanded uncertainties were calculated as described in the previous section, as a combination of type A and B uncertainties, for all the performance tests of the magnetic

wine cooler. Each data point was acquired over a 2-minute sampling time, with a sampling frequency of 150 Hz for each test condition. The maximum expanded uncertainties of the two tests are presented in Tab. 24.

Table 25 – Maximum expanded uncertainties associated with the experimentally determined variables (98% confidence interval).

Parameter	Uncertainty
Volumetric flow rate [L/h]	12
Temperature [°C]	0.1
Pressure [bar]	0.5
Torque [Nm]	0.2
Pump power [W]	2
Motor Power [W]	1
Fan power [W]	0.3
Valve power [W]	1
Cooling capacity [W]	1
Energy consumption [kWh/year]	22
COP [-]	0.04
η_{2nd} [%]	0.2

APPENDIX B – Entropy Generation of the Magnetic Wine Cooler Components

This appendix presents the analysis of the entropy generation of the prototype and the components of the Hydraulic/Control subsystem. A further estimated analysis on the entropy generation of the remaining subsystems and its components is suggested and evaluated, to get a sense of possible additional critical points in the contribution of the system inefficiencies.

B.1 Evaluation of the Hydraulic/Control Subsystem

The total entropy generation of the magnetic wine cooler prototype was obtained through Eq. B.1, from Hermes & Barbosa (2012), considering the temperatures of the hot and cold ends.

$$\dot{S}_{\mathrm{ger,sys}} = \frac{\dot{W}_{\mathrm{Tot}}}{T_{\mathrm{HE}}} + \dot{Q}_{\mathrm{C}}\left(\frac{1}{T_{\mathrm{HE}}} - \frac{1}{T_{\mathrm{CE}}}\right) \tag{B.1}$$

When evaluating the single components of the prototype, the entropy generation is calculated considering each component as a control volume. The entropy generation in a control volume is described by:

$$\dot{S}_{\mathrm{gen}} = \Delta\dot{S} - \sum \frac{\dot{Q}}{T} \tag{B.2}$$

The entropy variation can usefully be evaluated through the Gibbs equation, as follows:

$$ds = \frac{dh}{T} - \frac{vdP}{T} \tag{B.3}$$

The Hydraulic/Control system included the pump, the solenoid valves, the filter and the flow meter. The entropy generation of the pump was obtained by Eq. B.4, where $\overline{T}_{\mathrm{P}}$ is the average between the temperatures of the working fluid on the inlet and outlet of the pump. The heat dissipation of the pump was considered to be fully absorbed by the working fluid.

$$\dot{S}_{\mathrm{gen,P}} = \dot{m}_{\mathrm{f}}\left(\frac{\Delta h_{\mathrm{P}}}{\overline{T}_{\mathrm{P}}} - \frac{\Delta p_{\mathrm{P}}}{\rho\overline{T}_{\mathrm{P}}}\right) \tag{B.4}$$

The solenoid valves, on the other hand, were considered to dissipate all of the heat to the external ambient. Due to limitations on the instrumentation of the prototype, it was not feasible to evaluate the entropy generation of the valves as isolated components, and therefore the entropy generation was a combination of the solenoid valves and the filter installed at the hot side. The entropy generation of the valves and the filter were obtained

through Eq. B.5. The term $\Delta h/\overline{T}_{\mathrm{HS}}$ was omitted from Eq. B.5 as there was no temperature measurements among the components, limiting the assessment of the working fluid enthalpy.

$$\dot{S}_{\mathrm{gen,(V+Fil)}} = \left(\frac{\dot{W}_{\mathrm{V}}}{\overline{T}_{\mathrm{amb}}}\right)_{\mathrm{V}} + \left(\frac{\dot{V}\Delta p}{\overline{T}_{\mathrm{HS}}}\right)_{\mathrm{V+Fil}} \tag{B.5}$$

Lastly, the entropy generation of the flow meter was calculated as in Eq. B.6. The flow meter was installed between the pump outlet and the HHEx inlet, and as the pressure and temperature measurements were not at the exact inlet and outlet of the flow meter, the entropy generation due to heat losses ($\dot{Q}_{\mathrm{loss,FM}}$) of the tubing was also considered.

$$\dot{S}_{\mathrm{gen,FM}} = \dot{m}_{\mathrm{f}}\left(\frac{\Delta h_{\mathrm{FM}}}{\overline{T}_{\mathrm{FM}}} - \frac{\Delta p_{\mathrm{FM}}}{\rho\overline{T}_{\mathrm{FM}}}\right) + \frac{\dot{Q}_{\mathrm{loss,FM}}}{\overline{T}_{\mathrm{FM}}} \tag{B.6}$$

The heat losses of the tubing to the external environment were calculated as presented in Eq. B.7.

$$\dot{Q}_{\mathrm{loss,FM}} = \mathrm{UA}_{\mathrm{loss,FM}}(\overline{T}_{\mathrm{P,out}} - T_{\mathrm{HHEx,in}}) \tag{B.7}$$

The overall heat transfer coefficient was calculated by Eq. B.8, in terms of the internal surface area of the tube (INCROPERA et al., 2008).

$$\frac{1}{\mathrm{U}} = \frac{1}{h_{\mathrm{int}}} + \left(\frac{D_{\mathrm{t,in}}/2}{k_{\mathrm{t}}}\right)\ln\frac{D_{\mathrm{t,ex}}}{D_{\mathrm{t,in}}} + \frac{D_{\mathrm{t,in}}}{D_{\mathrm{t,ex}}}\frac{1}{h_{\mathrm{ex}}} \tag{B.8}$$

The internal heat transfer coefficient (h_{int}) was calculated through the equations below (INCROPERA et al., 2008).

$$Re_{\mathrm{D}} = \frac{\rho_{\mathrm{f}} u_{\mathrm{f}} D_{\mathrm{t,in}}}{\mu_{\mathrm{f}}} \tag{B.9}$$

$$Nu_{\mathrm{D}} = 3.66 \tag{B.10}$$

$$h_{\mathrm{int}} = \frac{Nu_{\mathrm{D}}\, k_{\mathrm{f}}}{D_{\mathrm{t,in}}} \tag{B.11}$$

The external heat transfer coefficient (h_{ext}) was calculated through the equations below (NELLIS; KLEIN, 2009; CHURCHILL; CHU, 1975).

$$Ra_{\mathrm{D}} = \frac{g\beta D_{\mathrm{t,ex}}(\overline{T}_{\mathrm{res}} - T_{\mathrm{amb}})}{\nu\,\alpha} \tag{B.12}$$

$$\overline{Nu}_{\mathrm{ext}} = \left[0.6 + \frac{0.387 Ra_{\mathrm{D}}^{1/6}}{(1 + (0.559/Pr)^{9/16})^{8/27}}\right]^2 \tag{B.13}$$

$$h_{\mathrm{ext}} = \frac{Nu_{\mathrm{ext}}\, k_{\mathrm{amb}}}{D_{\mathrm{t,ex}}} \tag{B.14}$$

Applying the experimental data of the F50V125 test condition into the equations described above, the result of the entropy generation of the Hydraulic/Control subsystem

is presented in Fig. 56, in reference to the total entropy generation of the system. The Hydraulic/Control subsystem contributes to 69% of the total entropy generation of the magnetic wine cooler, where 45% is due to the pump, 16% is due to the valves and the filter and 8% is due to the flow meter. The remaining portion was attributed to the sum of the contributions of the AMR/Magnet and Cabinet/HEx subsystems.

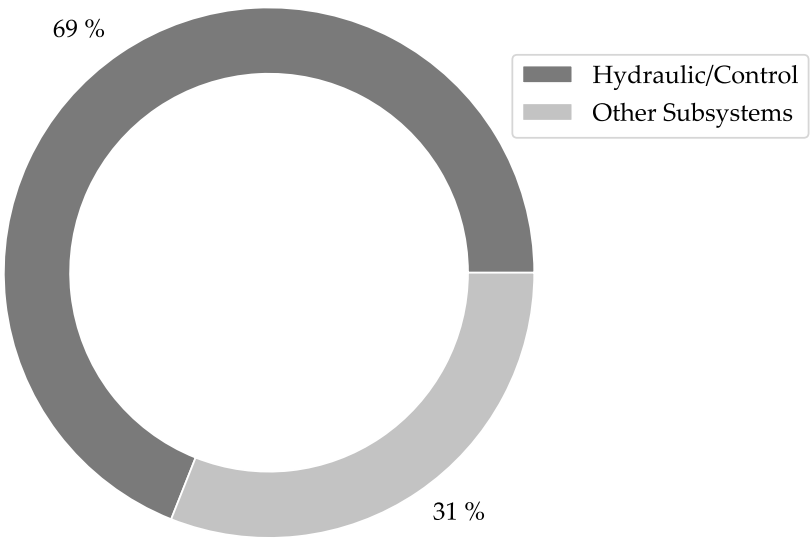

Figure 56 – Percentage of entropy generation of the magnetic prototype subsystems.

B.2 Estimation of the Entropy Generation of other Subsystems

The entropy generation of other components of the prototype was also estimated, with several approximations, so as to get a sense of possible additional critical points in the contribution of the system inefficiencies. The estimation of each component of the remaining subsystems, AMR/Magnet and Cabinet/HEx, is presented below.

B.2.1 AMR/Magnet

The AMR/Magnet subsystem included the AMR and the system to drive the rotation of the magnet. The entropy generation of the AMR was calculated as the sum of the entropy generations in the cold and hot blows, presented in the Eqs B.15, B.16 and B.17. As the pressure and temperature measurements were not at the exact inlet and outlets of the cold and hot blows, the entropy generation due to heat losses ($\dot{Q}_{\text{loss}}$) in the tubing, either by absorption or release, was also considered. The $\dot{Q}_{\text{loss,CB}}$ and $\dot{Q}_{\text{loss,HB}}$ were calculated following the same procedure used to calculate the $\dot{Q}_{\text{loss,FM}}$, from Eq. B.7 to B.14.

$$\dot{S}_{\text{gen,AMR}} = \dot{S}_{\text{gen,AMR,CB}} + \dot{S}_{\text{gen,AMR,HB}} \tag{B.15}$$

$$\dot{S}_{\text{gen,AMR,CB}} = \dot{m}_{\text{f}} \left(\frac{\Delta h_{\text{CB}}}{\overline{T}_{\text{CB}}} - \frac{\Delta p_{\text{CB}}}{\rho \overline{T}_{\text{CB}}} \right) - \frac{\dot{Q}_{\text{loss,CB}}}{\overline{T}_{\text{CB}}} \tag{B.16}$$

$$\dot{S}_{\text{gen,AMR,HB}} = \dot{m}_{\text{f}} \left(\frac{\Delta h_{\text{HB}}}{\overline{T}_{\text{HB}}} - \frac{\Delta p_{\text{HB}}}{\rho \overline{T}_{\text{HB}}} \right) + \frac{\dot{Q}_{\text{loss,HB}}}{\overline{T}_{\text{HB}}} \tag{B.17}$$

The entropy generation of the magnet is due to the mechanical losses of its drive system to the external ambient. The power consumption of the drive system is due to the magnetic interaction and transmission losses. To characterize the entropy generation of the drive system, the transmission losses power ($\dot{W}_{\text{Tr}}$) must be separated from the magnetic interaction power ($\dot{W}_{\text{Mag}}$), by Eq. B.18. The magnetic interaction power consumption is calculated as in Eq. B.19, and is dependent on the mass of magnetocaloric material (MCM), its temperature and entropy variation and the magnet frequency. Due to limitations in the instrumentation of the prototype, the temperature and entropy variation of the magnetocaloric material could not be assessed. The magnetic interaction power consumption was approximated based on results of Capovilla et al. (2016), that presented the variation of the power losses as a function of the magnet frequency, in a transmission system very similar to that of the magnetic wine cooler prototype. The losses vary linearly with the magnet frequency, being around 5 W for a magnet frequency of 0.5 Hz and 10 W for a magnet frequency of 1.0 Hz. Considering all the transmission losses as a heat rejection to the external ambient, the entropy generation of the magnet was calculated by Eq. B.20.

$$\dot{W}_{\text{Tr}} = \dot{W}_{\text{Mo}} - \dot{W}_{\text{Mag}} \tag{B.18}$$

$$\dot{W}_{\text{Mag}} = f \left(m \oint T \, ds \right)_{\text{MCM}} \tag{B.19}$$

$$\dot{S}_{\text{gen,Mag}} = \frac{\dot{W}_{\text{Tr}}}{\overline{T}_{\text{amb}}} \tag{B.20}$$

B.2.2 Cabinet/HEx

The Cabinet/HEx subsystem included the CHEx, the HHEx and the cold and hot fans. As there were no measurements on the air velocities, air pressure drop and air temperatures in the fans and heat exchangers, the portions of entropy variation of the air currents were not considered in the equations, and the entropy generation of this subsystem was calculated as an underestimated approximation.

The entropy generation of the CHEx was calculated considering a control volume around the boundaries of the CHEx itself, separated from the cold fan, and immersed into the cabinet air as exchanging environment. The entropy variation of the air current could not be assessed and was disregarded. Thus, only the entropy variation of the working

fluid current and the heat absorbed from the environment was considered, and the entropy generation in the CHEx was obtained by Eq. B.21.

$$\dot{S}_{\text{gen,CHEx}} = \dot{m}_{\text{f}} \left(\frac{\Delta h_{\text{CHEx}}}{\overline{T}_{\text{CHEx}}} - \frac{\Delta p_{\text{CHEx}}}{\rho \overline{T}_{\text{CHEx}}} \right)_{\text{f}} - \frac{\dot{Q}_{\text{C}}}{\overline{T}_{\text{cab}}} \tag{B.21}$$

Similarly, the entropy generation in the HHEx was calculated by Eq. B.22.

$$\dot{S}_{\text{gen,HHEx}} = \dot{m}_{\text{f}} \left(\frac{\Delta h_{\text{HHEx}}}{\overline{T}_{\text{HHEx}}} - \frac{\Delta p_{\text{HHEx}}}{\rho \overline{T}_{\text{HHEx}}} \right)_{\text{f}} + \frac{\dot{Q}_{\text{H}}}{\overline{T}_{\text{amb}}} \tag{B.22}$$

The entropy generation of the fans was calculated considering only the heat exchange with their respective environments, disregarding the entropy variation of the air currents. As there were no characterization of the fans, the efficiencies could not be assessed, and were both considered to be 20%. The entropy generation of the cold and hot fans were obtained by Eq. B.23 and Eq. B.24, respectively.

$$\dot{S}_{\text{gen,CF}} = \frac{\dot{W}_{\text{CF}} \left(1 - \eta_{\text{CF}}\right)}{\overline{T}_{\text{cab}}} \tag{B.23}$$

$$\dot{S}_{\text{gen,HF}} = \frac{\dot{W}_{\text{HF}} \left(1 - \eta_{\text{HF}}\right)}{\overline{T}_{\text{amb}}} \tag{B.24}$$

B.3 Overall Evaluation of the Entropy Generation

With the approximations of the entropy generation of single components from the AMR/Magnet and Cabinet/HEx subsystems, all the subsystems and its components of the prototype were evaluated individually. Fig. 57 presents the evaluation of the contribution of each subsystem to the total entropy generation of the prototype. The Cabinet/HEx subsystem contributes with 20% of the total entropy generation of the magnetic wine cooler, being the second highest contribution. The AMR/Magnet subsystem contributes with 11% of the total entropy generation, representing the subsystem with the least contribution.

In a deeper examination of the entropy generation, Fig. 58 presents the contributions of each component. As it can be seen, the pump contributes with around 45% of the total entropy generation of the prototype, representing a very critical point into the system inefficiency. The fans, although positively contributing to the external second-law efficiency – as they increase the UA of the HEx, represent the second highest contribution, totalling around 17%. The valves contribute almost as much as the fans, but as it also carry the entropy generation due to the filter, it cannot be confirmed that the valves represent a third critical contribution to the system inefficiencies, as the filter could represent a high restriction to the fluid flow and therefore a high pressure drop. The driving system of the magnet and the AMR, intrinsically the core of magnetic refrigeration, contribute together in around 12%. The contribution of the auxiliary flow meter is around 8.5%, a high contribution for an auxiliary component but a loss that could be avoided in a final product version of the magnetic wine cooler. Lastly,

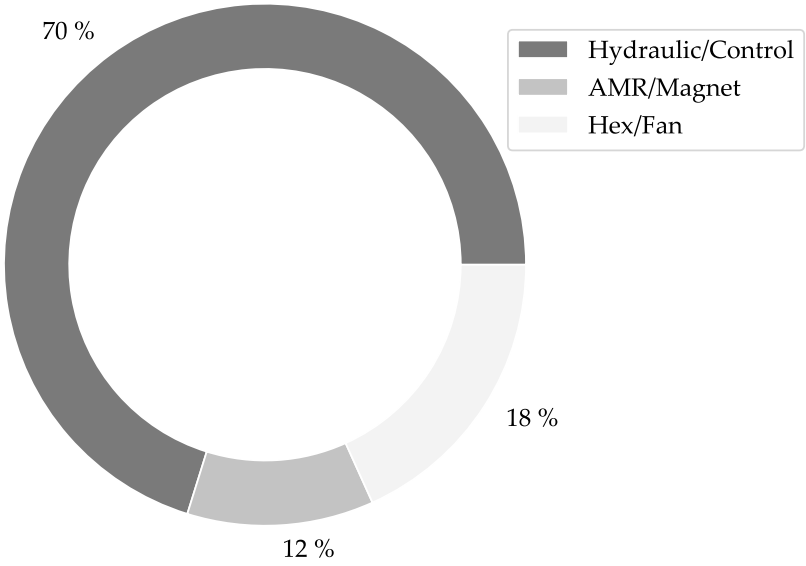

Figure 57 – Percentage of entropy generation of the magnetic prototype subsystems.

the cold and hot HExs contribute very little to the total entropy generation, setting both as optimized points in the prototype in terms of inefficiencies.

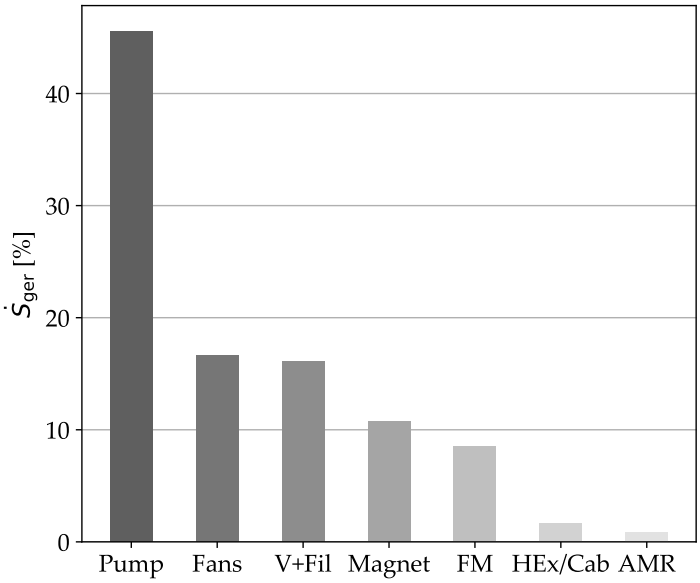

Figure 58 – Percentage of entropy generation of each component of the magnetic prototype.

The pump, the fans and the valves should be addressed first when considering the improvement of the inefficiencies of the magnetic wine cooler, as together they represent 78% of the total entropy generation of the prototype. However, with a sized and more efficient pump, the need of a high heat transfer coefficient in the hot side – currently supplying three fans, would naturally decrease, as the heat dissipation in the pump would be lower and the power of the fans could be decreased. Also, the entropy generation of the valves should be evaluated without the influence of the filter, to identify if the valves are indeed one of the

critical points in terms of inefficiencies.

The total entropy generation of the system was then calculated by the sum of the entropy generation of each component and further compared to the entropy generation of the system obtained by Eq. B.1. The result calculated by the sum of the single components underestimated the total entropy generation in around 2.5%, representing a good error given the approximations made. However, the shares of entropy generation of the components and the subsystems could change if the entropy generation evaluation were more accurate. So as to improve the entropy generation calculations, some modifications could be made in the current prototype.

The entropy generation of the magnet could be improved by a better approximation of the magnetic interaction power consumption, with measurements of temperature inside the layers of magnetocaloric material, so as to assess the average temperature of the regenerative matrix in each blow and the respective entropy variation. The entropy generation of the CHEx, HHEx and the fans could be improved with a characterization in a wind tunnel, to assess the air flow rates of the fans and the pressure drops in the fans and the HExs. With the pressure drop and air flow rates, the efficiencies of the fans could also be calculated. Nevertheless, it is necessary to measure the temperatures in the inlet and outlet of the fans and in the inlet and outlets of the HEx in the air currents, so as to assess the enthalpy and entropy variation.

Besides the changes proposed above, the prototype could be instrumented with thermocouples and pressure transducers in the inlet and outlet of each component, so as to separate the entropy generation of the main components from the auxiliary components and from the heat losses due to the tubing.

APPENDIX C – Experimental Results of the Conventional Characterization Tests

Table 26 – Experimental results of the characterization tests of the conventional wine cooler.

$\overline{T}_{set}$ [ºC]	$\overline{T}_{up}$ [ºC]	$\overline{T}_{low}$ [ºC]	$\overline{T}_{avg}$ [ºC]	$\overline{T}_{amb}$ [ºC]	$\overline{T}_{evap,in}$ [ºC]	$\overline{T}_{evap,out}$ [ºC]	$\overline{T}_{cond,in}$ [ºC]	$\dot{W}$ [W]	$\dot{Q}_C$ [W]	COP [-]	η_{2nd} [%]
8	7.7	8.5	8.2	24.9	-4.3	-1.1	38.6	42.8	29.1	0.68	4.0
12	11.7	12.2	12.0	24.8	1.0	3.9	34.0	31.8	22.3	0.70	3.1

APPENDIX D – Experimental Results of the Magnetic Wine Cooler Characterization Tests

Table 27 – Experimental results of the performance tests of the magnetic wine cooler prototype.

Test point	$\dot{V}_f$ [l/h]	$\overline{T}_{cab}$ [°C]	$\overline{T}_{amb}$ [°C]	$\overline{T}_{CHEx,in}$ [°C]	$\overline{T}_{HHEx,in}$ [°C]	$\dot{W}$ [W]	$\dot{Q}_C$ [W]	COP [-]	η_{2nd} [%]
F50V125	124.7	12.5	24.2	11.5	26.9	58.5	24.3	0.41	1.7
F50V150	149.6	11.9	24.8	11.0	27.3	84.8	26.4	0.31	1.4
F50V175	176.1	11.8	24.0	10.7	27.4	115.3	25.3	0.22	0.9
F50V200	199.3	13.0	24.6	12.1	28.0	148.4	24.0	0.16	0.6
F50V225	225.3	15.0	24.3	14.4	29.0	192.9	20.1	0.10	0.3
F75V125	126.0	13.5	25.4	12.7	27.6	63.4	24.7	0.39	1.6
F75V150	149.8	11.6	24.4	10.7	27.2	85.5	26.2	0.31	1.4
F75V175	174.9	11.2	24.3	10.3	27.5	117.3	26.7	0.23	1.0
F75V200	200.9	11.6	24.3	10.7	28.0	155.9	26.1	0.17	0.7
F75V225	224.7	12.4	24.2	11.7	28.6	199.0	24.5	0.12	0.5
F100V125	125.2	13.0	25.3	12.1	27.5	65.6	24.2	0.38	1.6
F100V150	149.3	11.6	24.7	10.7	27.1	88.8	26.7	0.30	1.4
F100V175	174.0	10.8	24.6	9.8	27.7	119.9	27.9	0.23	1.1
F100V200	201.0	11.3	24.7	10.3	28.1	160.6	27.4	0.17	0.8
F100V225	224.8	12.1	24.8	11.3	28.7	200.2	25.9	0.13	0.6

ANNEX A – Heat Exchanger Technical Drawing

The CHEx and HHEx are identical to the model of heat exchanger presented in Fig. 59, in terms of external dimensions and pipe diameter. They differ only in the number of fin density, the CHEx having 10 fins/pol and the HHEx having 12 fins/pol.

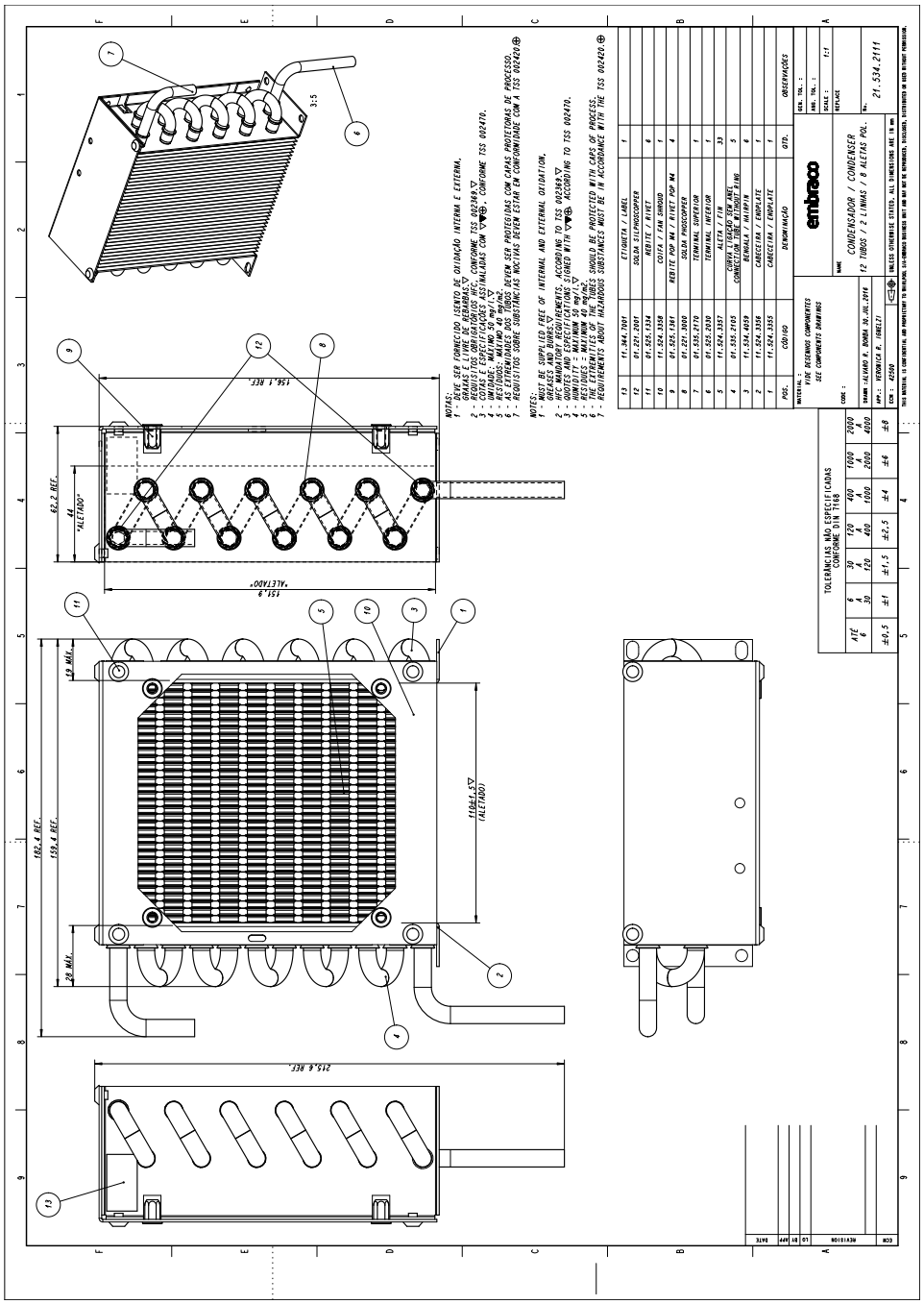

Figure 59 – Technical drawing of the heat exchangers assembled in the magnetic wine cooler prototype.